Mitochondrial nucleoid distribution and its relation to presynaptic activity investigated by correlative light microscopy

Dissertation
for the award of the degree

"*Doctor rerum naturalium*"

Division of Mathematics and Natural Sciences
of the Georg August University Göttingen

within the doctoral program *Molecular Medicine*
of Göttingen Graduate School for Neurosciences, Biophysics and Molecular Biosciences (GGNB)

submitted by

Axel Rösch

from Karlsruhe
Göttingen, 2022

Thesis Committee:

Prof. Dr. Stefan Jakobs

Clinic for Neurology
High Resolution Microscopy of the Cell
University Medical Center Göttingen (UMG)

Prof. Dr. Michael Müller

Dept. Neurophysiology and Sensory Physiology
Physiology and Pathophysiology
University Medical Center Göttingen (UMG)

Prof. Dr. Michael Meinecke

Biochemistry Center Heidelberg(BZH)
Molecular Membrane Biology
Heidelberg University

Members of the Examination Board

Prof. Dr. Stefan Jakobs	(Reviewer)
Prof. Dr. Michael Müller	(2nd Reviewer)
Prof. Dr. Michael Meinecke	(Biochemistry Center, Heidelberg University)
Prof. Dr. Peter Rehling	(Department of Cellular Biochemistry, UMG, Göttingen)
Prof. Dr. Caroline Wichmann	(Institute for Auditory Neuroscience & InnerEarLab, UMG Göttingen)
Dr. Wiebke Möbius	(Department of Neurogenetics, Max Planck Institute for Multidisciplinary Sciences, Göttingen)

Date of the oral examination:

04th of November, 2022

Affidavit

I hereby declare, that I prepared the PhD thesis entitled:

"Mitochondrial nucleoid distribution and its relation to presynaptic activity investigated by correlative light microscopy"

that was submitted on the 09th of September, 2022 is the result of my own work and was prepared with no other sources than quoted.

Göttingen, 09th of September, 2022

Axel Rösch

Summary

Mitochondria are essential for eukaryotic life, because they provide most of the energy for a variety of cellular processes. Especially high energy demanding cells and tissues like the muscles and the neuronal cells of the brain depend on a reliable supply of energy. It is of no surprise that impairments of this organelle manifest in pathophysiological effects. To perform their task as the "power plant of the cell", mitochondria rely on the import of proteins encoded in the nucleus. Together with thirteen proteins encoded in their own genome (mitochondrial DNA, mtDNA), they assemble the oxidative phosphorylation system for energy production. Although many studies investigated neuronal mtDNA, little is known about the relationship between the presence of mtDNA in axonal mitochondria, mitochondrial function and presynaptic activity. The aim of this work was to investigate the nucleoid (Protein-mtDNA complex) distribution in neurons and to study the interplay between neuronal activity and the mtDNA content of neuronal mitochondria.

This work shows that the nucleoid distribution is not homogeneous across the neuronal cell. Rather, the majority of mitochondria in the axon do not harbor a nucleoid, whereas 90 % of dendritic mitochondria do. Additionally, it was found that the mitochondria carrying mtDNA in the axon are mainly accumulated in the presynapse. This raised the question if there is a relationship between synaptic activity and the presence of mitochondria with nucleoids. . A single microscopy method such as immunofluorescence microscopy or live cell imaging alone would not be sufficient to answer this question, but a combination of both imaging modalities would is required to gain new insights into the relationship between neuronal activity and mitochondrial dynamics.

This is why a new correlative light microscopy workflow was developed that allows functional live cell microscopy to be combined with subsequent immunofluorescence imaging on other microscopes. For this, three major obstacles had to be addressed: the technical requirements of stable on-stage fixation, the adaptation of fixation conditions and the relocation of a predefined region of interest when the sample is moved from one microscope to another. The main obstacle of stable on-stage fixation was overcome by designing a novel live cell imaging chamber. Together with an optimized fixation protocol, this set-up allows for a rapid and homogenous fixation of the cells during live cell image acquisition. Subsequent immunofluorescence staining and transfer of the sample to another microscope presented the challenge of locating the same cells and regions of interest identified during live cell imaging. To address this problem, a combination of a unique label on the coverslip and an image registration script was developed to store regions of interest and relocate them relative to the label.

The correlative live cell imaging system was used to study the relationship between presynaptic activity and the presence of mitochondrial DNA in neuronal mitochondria. The results revealed that about 70 % of the mitochondria located in active presynapses harbor nucleoids, whereas 36 % of non-synaptic axonal mitochondria carry nucleoids. This finding led to the question if there is an active selection of mtDNA-loaded mitochondria driven by the

specific demand at their cellular location. The idea of an active selection was supported by silencing neuronal activity with the reversible neurotoxin Tetrodotoxin (TTX), which resulted in a significant reduction to ~44 % mitochondria with mtDNA in presynapses compared to the untreated presynapses (~59 %). Furthermore, after a period of 24 h of toxin washout, the level of nucleoid positive mitochondria recovered fully. Taken together, these results suggest a selective accumulation of mtDNA-positive mitochondria driven by the activity of the presynapse and the associated increased demands on the mitochondria.

Table of figures

Contents

1 Introduction

1.1 Neurons

All human cognitive functions, such as memories, emotions and conscious movements, are formed and processed in the brain, a complex structure consisting of billions of specialized cells, which are organized into several subareas with distinct functions and responsibilities. The hippocampus, for example, is the central hub for processing sensory information to form long-term memory (Eichenbaum et al., 1992). To accomplish this task, a certain flexibility is required to form new neuronal connections, maintain existing ones, and break down synapses that are no longer needed. This process is called synaptic plasticity (Citri & Malenka, 2008).

The smooth functioning of the brain requires the interaction of different cell types. The cells that enable the transmission of information are called neurons (Figure 1). The transmission signal itself is conducted through the cell in the form of electrical impulses, so called action potentials (Hodgkin & Huxley, 1952). Input of information is received over multiple cell extensions called dendrites or directly in the main cell body, the soma, and transmitted via a long segment, the axon. In humans, axons can span a distance of a few centimeters in the brain up to about one meter along the spine (Muzio & Cascella, 2020).
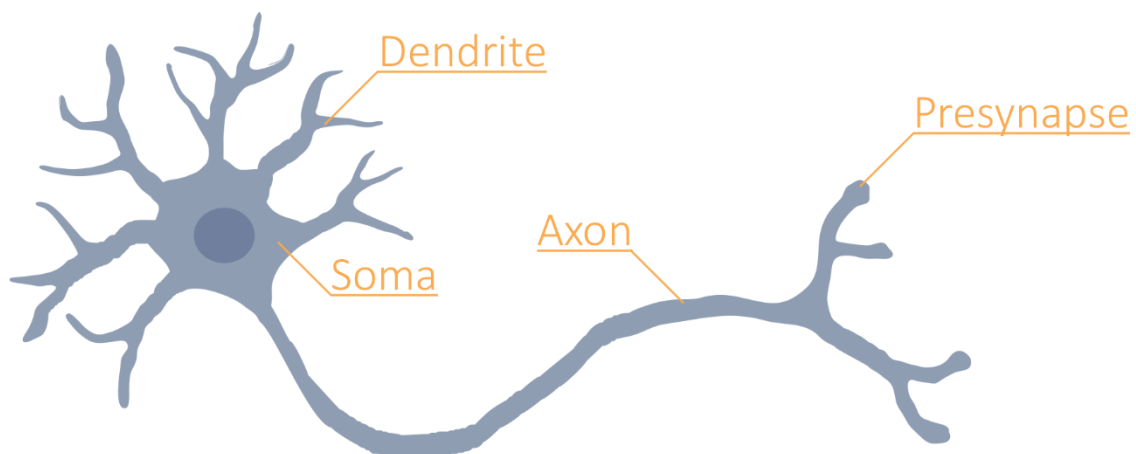
Figure 1: Components of a neuron. *From the cell body, called soma, emanate several small cell extensions called dendrites where the postsynapses are located. The axon is a long cell segment that protrudes from the soma and has presynapses on its surface and at its end.*

For signal transmission between cells, neurons form highly specialized connections with neighboring neurons called synapses (Schikorski & Stevens, 1997). These consist of a presynapse located at the axon and a postsynapse, which can be located at the main cell body (soma) or at the dendrites. Signal transmission between two neurons occurs mainly chemically via signaling molecules such as epinephrine, norepinephrine, acetylcholine and glutamate, which are called neurotransmitters (Goldstein, 2010; Zhou & Danbolt, 2014). These neurotransmitters are stored in synaptic vesicles (SV) in the presynapse as illustrated in Figure 2. Upon the arrival of an action potential, a short local inversion of the membrane potential of the neuronal plasma membrane which is propagating along the cell through voltage gated opening of ion channels, the presynapse releases the neurotransmitters into the synaptic cleft

(Bean, 2007). The SVs fuse with the plasma membrane in the so-called active zone and release their load by exocytosis into the space between the presynapse and postsynapse (Rizzoli, 2014). After the neurotransmitter docks with receptors at the postsynapse, the chemical signal is converted back into an electrical signal. SVs are then recycled and acidified via an ATPase (Moriyama et al., 1992). The resulting pH gradient is required to reload the SVs with fresh neurotransmitter via an antiporter. The loaded SVs are then stored in a vesicle pool until the next action potential arrives.
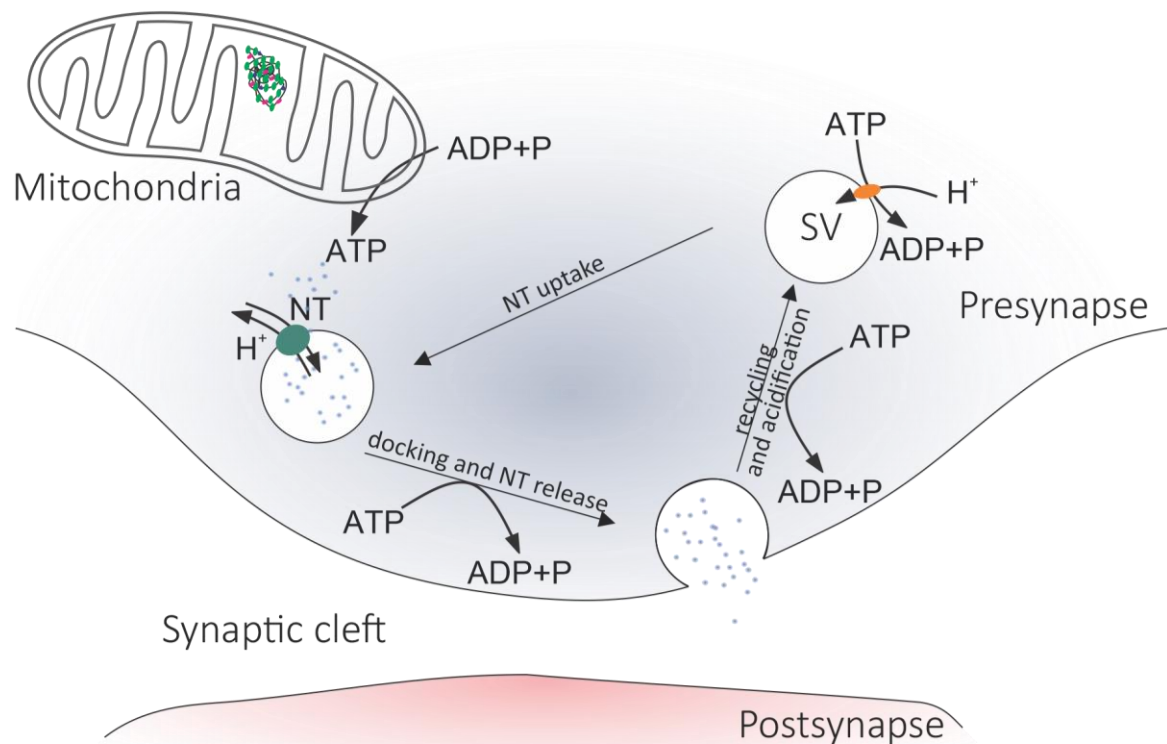
Figure 2: The energy demanding synaptic vesicle cycle in the presynapse. *For signal transduction between cells, synaptic vesicles (SV) are exocytosed upon Ca^{2+} uptake in the presynapse. This releases neurotransmitters (NT) into the synaptic cleft that typically induce an action potential in the postsynapse. To replenish the cellular SV pool, parts of the plasma membrane are endocytosed. These empty vesicles are acidified by an active proton-pumping ATPase using ATP. The resulting ion gradient between the vesicle lumen and the cytosol drives the uptake of NTs into the SV via an antiporter. In addition to acidification, energy consuming processes like vesicle docking and endocytosis, as well as ion transport at the plasma membrane to restore membrane potential, depend on the availability of ATP. In addition to the glycolysis, the mitochondria present at the presynaptic site constantly replenish the local ATP stores via and oxidative phosphorylation.*

Several studies have shown that synaptic transmission places a large energy burden on neuronal cells (Harris et al., 2012; Pathak et al., 2015; Rangaraju et al., 2014). It is estimated that the energy demand of the brain, normalized to weight, is approximately 8 to 10 times greater than that of other tissues (Mink et al., 1981; Pulido & Ryan, 2021). As shown in Figure 2 there are many processes consuming ATP such as the acidification of the SVs, the docking and recycling of the SVs and the restoring of the plasma membrane potential. A recent study by Pulido et al. showed that 44 % of the presynaptic ATP content alone is used for constant

re-acidification of the SV within the reserve pool (Pulido & Ryan, 2021). This is because SVs are constantly leaking protons (Pulido & Ryan, 2021). However, how the high and rapidly changing energy demand is met, is still controversial. The most obvious answer to this question is the mitochondrion, but the actual interplay between mitochondria and synaptic activity is still unclear.

1.2   Mitochondria in neurons

Mitochondria are often referred to as the "powerhouse of the cell", but in addition to ATP production, mitochondria are also involved in the production of lipids, ion buffering, and Ca^{2+} signaling. With such a wide variety of tasks, mitochondria are much more than just the "powerhouse of the cell" (Figure 3). In the compartmentalized structure of neurons (Figure 1), mitochondria show strong heterogeneity in their morphology (Figure 4) (Jakobs et al., 2011; Pekkurnaz & Wang, 2022; Popov et al., 2005). Somatic mitochondria form a complex dynamic network of various sizes (Figure 4 B), whereas dendritic mitochondria are elongated (Figure 4 A). With a length of about 1 µm, axonal mitochondria are comparatively small (Figure 4 C) (Lewis et al., 2018). In addition to their different appearance, neuronal mitochondria also show high variation in protein distribution between organelles. Furthermore, other studies show significant differences between the protein levels in synaptic vs non-synaptic mitochondria (Völgyi et al., 2015).

Large cells such as neurons rely on efficient energy transport from the soma to their axon terminals, which can be several centimeters away from the main cell body. However, recent results show that mitochondria may not be required for this as rapid changes in ATP levels are likely regulated by glycolysis (Ashrafi & Ryan, 2017). Moreover, only a fraction of presynapses are occupied by mitochondria (Shepherd & Harris, 1998). Nevertheless, the presence of mitochondria in presynapses seems to influence the synaptic plasticity and contribute to a higher stability of this compartment (Lees et al., 2019).
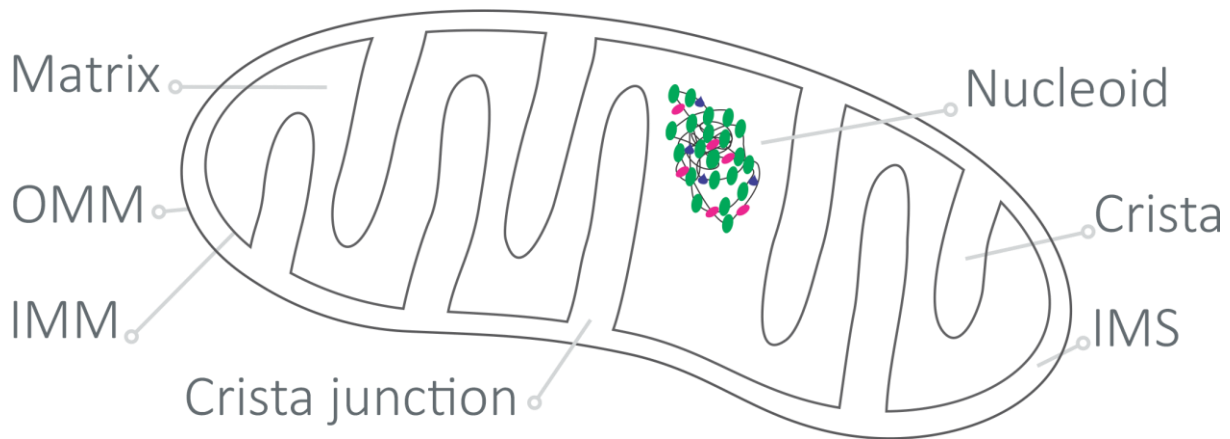
Figure 3: Schematic of a Mitochondrion. *The organelle has two membranes, the outer mitochondrial membrane (OMM) and the inner mitochondrial membrane (IMM) are separated by the intermembrane space (IMS). The invaginations of the IMM are called cristae membranes that are connected to the IMM by crista junctions. The space enclosed by the IMM and crista membranes is called the matrix. The nucleoid a complex of different proteins and the mitochondrial DNA (mtDNA) is located in the matrix.*

The presynaptic mitochondria are modulating synaptic strength through Ca^{2+} buffering. Ca^{2+} influx into the presynapse is used as a trigger for neurotransmitter release. Thus decreasing the effective Ca^{2+} concentration in the presynapse, by taking the ions up into the mitochondrial matrix, leads to a decreased release of neurotransmitter (Lewis et al., 2018). To enable this, axonal mitochondria are more sensitive to cytosolic Ca^{2+} concentrations than mitochondria in other tissues (Fieni et al., 2012; Patron et al., 2019). Ca^{2+} influx into the mitochondrial matrix is regulated by the mitochondrial calcium uniporter (MCU) complex, whose protein composition varies between tissues. In neurons, MCU3 has been found to upregulate Ca^{2+} influx (Patron et al., 2019). The force for ion transport through the IMM is provided by the pH gradient rather than the electrical gradient (Poburko et al., 2011). Nevertheless, both gradients are interdependent, and both are generated by oxidative phosphorylation (OXPHOS), which is a central part of the energy metabolism (Santo-Domingo & Demaurex, 2012).

The mitochondrial uptake of Ca^{2+} ions has been shown to transiently upregulate mitochondrial respiration. This suggests a flexible mechanism of the organelle to meet changes in the local energy demand (Ashrafi et al., 2020; Hajnoczky et al., 1995). Moreover, a sudden local rise of Ca^{2+} levels can lead to the arrest of mobile axonal mitochondria; this is an alternative support mechanism to cover the synaptic energy demand (Li et al., 2009; Mironov, 2006; Vaccaro et al., 2017). This also means that the higher the activity of a synapse marked by local Ca^{2+} influx, the higher is the likelihood that passing mitochondria will stop and stay.
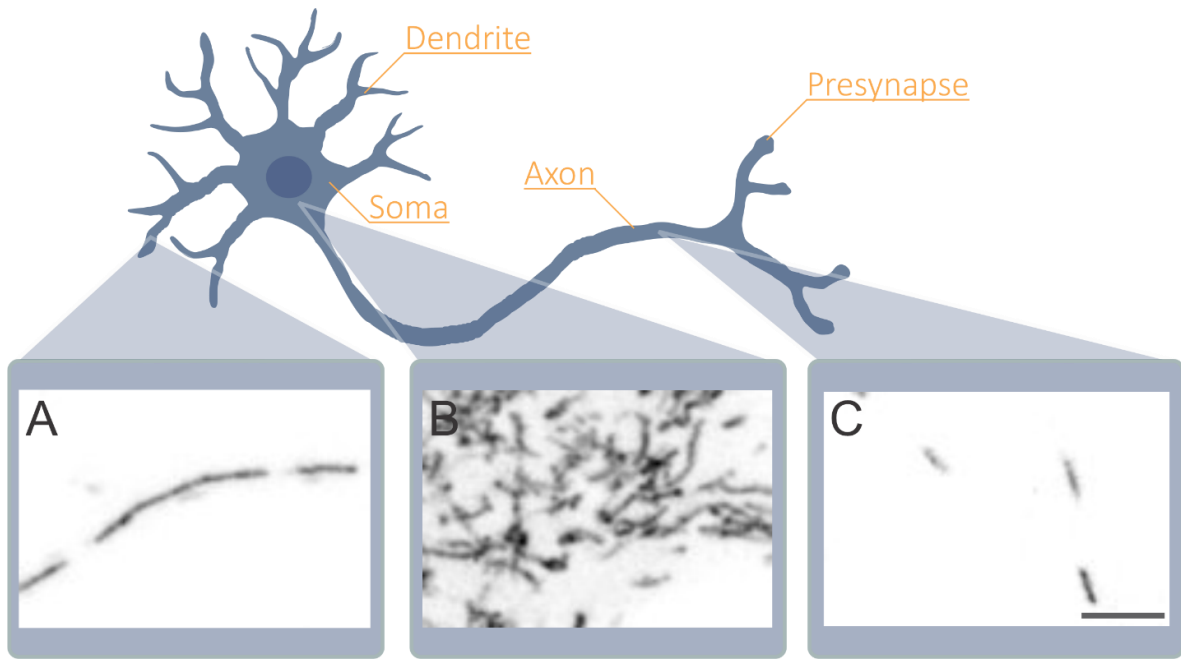
Figure 4: Diversity of mitochondrial morphology in different neuronal compartments. *The mitochondria in the different compartments have different morphologies as shown in the fluorescence images. Mitochondria are labeled with an anti- Cytochrome C antibody. A) Mitochondria in the dendrites are large organelles up to several micrometers long. B) Mitochondria in the soma form an interconnected network of tubes. C) Presynaptic mitochondria are small and often isolated from each other. (Unpublished data, scale bar: 5 µm).*

Moreover, local stable mitochondria contribute to a high plasticity by forming local nodes to promote local protein translation and establish axonal branches and new synapses (Rangaraju et al., 2019; Spillane et al., 2013). Therefore, it is essential that not only mitochondria but also the necessary nuclear encoded mRNAs are transported into the axon. RNA sequencing of isolated axons found abundant mRNAs in this compartment. These experiments revealed a large amount of mRNA from nuclear-encoded mitochondrial genes, including mRNA encoding the mitochondrial transcription and translation machinery (Costa & Willis, 2018). This is particularly important because the lifespan of some proteins is estimated to be shorter than the time required for their transport along the axon (Miller & Samuels, 1997).

1.3   Mitochondrial DNA (mtDNA)

Mitochondria harbor their own genome, mitochondrial DNA (mtDNA), which is a remnant of their endosymbiotic origin. The endosymbiotic origin theory states that mitochondria evolved from alphaproteobacteria that invaded early eukaryotic and anaerobic cells. This theory is strongly supported by the prokaryotic features of the mitochondrial genome (Gray et al., 1999). During the evolution, mitochondrial genes were continuously transferred to the eukaryotic genome (Adams & Palmer, 2003).

Although most mitochondrial proteins are now encoded in the nucleus, the mtDNA of eukaryotes still contains 13 essential genes encoding proteins of the OXPHOS complexes, as well as 22 tRNAs and 2 rRNAs (Wallace, 1994). The mtDNA is gene dense and exists as a 16.6 kb circular double-stranded DNA, as shown in Figure 5 (Nass, 1966; Van Bruggen et al., 1966). The genes are distributed on both strands of the mtDNA, called the heavy strand and the light strand according to their behavior during density centrifugation. Both strands harbor a single promoter, referred to as the heavy strand promoter (HSP) or light strand promoter (LSP), respectively (Chang & Clayton, 1984). This means that all genes of one strand are transcribed on one polycistronic RNA strand. Thus, the processing of RNA to the individual mRNA, tRNA, or rRNA is regulated at the posttranscriptional level. The 13 genes are transcribed into 11 mRNAs, and some of the genes overlap in their sequences. Therefore, *ND4L/ND4* and *ATP8/ATP6* are located on the same bicystronic mRNA (Rak et al., 2016; Van Haute et al., 2015). Each of the bicystronic mRNAs contains two open reading frames, one for each gene. The mtDNA also encodes the small peptide humanin, which was discovered in 2001 (Hashimoto et al., 2001). This peptide is thought to have a neuroprotective function in Alzheimer's disease via its activity in the regulatory chain of apoptosis (Guo et al., 2003; Ikonen et al., 2003; Lee et al., 2013).

The mtDNA molecule is tightly decorated with different proteins for packaging, transcription, and replication that together form a Protein-DNA-complex that is called a nucleoid (Bogenhagen, 2012). Each cell has multiple copies and the nucleoids are polymorphic. The number of mtDNA copies varies around 500-6000 depending on the cell type and their specific energy requirements (D'Erchia et al., 2015; Reznik et al., 2016). Although, light microscopy provides better local information, studies analyzing nucleoid quantities are mainly performed using quantitative PCR or sequencing data. The main reason for this is the tendency of nucleoids to appear clustered at a distance smaller than the diffraction limit (Kukat et al., 2011). Therefore, conventional microscopy underestimated the number of nucleoids. Super-resolution microscopy can resolve individual nucleoids and depending on the cell type, it is possible to detect 60% more individual nucleoids than conventional confocal microscopy (Kukat et al., 2011).

An abundant protein on nucleoids is the mitochondrial transcription factor A (TFAM) (Kang et al., 2007). In the steady state, TFAM acts as a histone-like packaging molecule and initiates transcription by unwinding mtDNA upstream of promoters (Fisher et al., 1992). This enables the mitochondrial RNA polymerase (POLRMT) to bind to the now accessible DNA, which initiates the transcription process. Recently, Brüser et al. showed that the transcription and replication of mitochondrial DNA are regulated by the degree of TFAM packaging. By using multicolor STED microscopy, they demonstrated that TFAM levels on nucleoids vary depending on how active the nucleoid is (Brüser et al., 2021). Low TFAM levels on mtDNA corresponded with a high activity of the nucleoids: They were either involved in transcription or replication or both at the same time. This can be explained by the DNA-shaping properties of TFAM, with lower TFAM levels corresponding to lower compactness of DNA, resulting in more space for the transcription or replication machinery (Brüser et al., 2021; Farge et al.,

2014). On the other hand, a higher TFAM level leads to a decrease in binding site accessibility. In fact, the great majority of all nucleoids in a cell are tightly decorated with TFAM and are considered inactive (Brüser et al., 2021). This large pool of dormant mtDNA is believed to compensate for possible mutations in a single mtDNA molecule (Filograna et al., 2019; Stewart & Chinnery, 2015).

The simultaneous presence of unmodified and mutant mtDNA sequences in a cell is called heteroplasmy (Parakatselaki & Ladoukakis, 2021). Before a mutation causes a physiological effect, its occurrence must be above a certain threshold that depends on the type of mutation. Single large-scale deletions reach this threshold at about 60 %. For other mtDNA mutations, a prevalence of approximately 80-90 % is required to have an impact on mitochondrial health (Rossignol et al., 2003; Russell & Turnbull, 2014). One cause of mtDNA mutations is generally seen in the presence of reactive oxygen species (ROS) (Harman, 1981). In the ROS vicious circle theory, the caused mutations may lead to impaired OXPHOS, which would result in a further increased ROS production as well as a further increased mutation rate (Balaban et al., 2005; Harman, 2002). This positive feedback loop would lead to an exponentially growing mutation rate. However, Trifunovic et al. found that the accumulation of abberant mtDNA in mitochondria of a mouse line susceptible to mtDNA mutations was linear over time. In addition, ROS levels as well as antioxidant defense protein expression levels indicated normal levels of oxidative stress in these cells. These results are in contrast to the ROS vicious circle theory (Trifunovic et al., 2005).

Another reason for mutations to accumulate in mtDNA is that mtDNA replication is error-prone due to the lack of DNA repair mechanisms (Fontana & Gahlon, 2020). Interestingly, some mutations may lead to an increased replication rate, resulting in a higher accumulation over time. The reason for this is not yet entirely clear. In the case of single point mutations, one explanation could be that reduced energy production due to impaired OXPHOS proteins leads to an increase in mtDNA replication to compensate for the impairment (Yoneda et al., 1992). However, computer modeling has shown that this could also occur due to a statistical probability known as genetic drift (Chinnery et al., 2002; Elson JL et al., 2001).

The pathological accumulation of mtDNA alterations does not occur to the same extent in every cell. Therefore, cells with a reduced metabolic function can be controlled by programmed cell death, known as apoptosis. While this is part of the normal housekeeping in most regenerative tissues, the brain is particularly prone to accumulate mtDNA mutations because neurons do not undergo cell division and the cells last a lifetime of the organism.

Figure 5: Gene map of the Rattus norvegicus mtDNA. *A 16,315 base pairs (bp) circular DNA harboring the regulatory sequence D-loop, the genes for 13 mRNAs and 2 rRNAs. The genes are distributed on both strands (heavy and light) with 12 mRNAs encoding genes on the heavy strand and only one, ND6, on the light strand.*

1.4 mtDNA in neurodegeneration

Mitochondrial dysfunction is one of the most common causes of metabolic diseases and occurs mainly in tissues with high energy demands, such as the heart or the brain. Therefore, it is not surprising that mitochondria play a central role in many neurological diseases such as Alzheimer's disease (AD) or Parkinson's disease (PD) (Monzio Compagnoni et al., 2020; Pyle et al., 2016). The causes of mitochondrial dysfunction are diverse and range from mutations in mitochondrial or nuclear DNA, to variations in nucleoid copy number to impaired mitophagy.

The accumulation of mtDNA mutations appears to play an important role in aging and neurological diseases (Dolle et al., 2016). The importance of mtDNA sequence integrity is supported by the predisposition of mitochondrial haplotypes to certain neurological diseases such as Leber's hereditary optic neuropathy (Torroni et al., 1997). There is also evidence of inherited risk due to mtDNA polymorphisms for other diseases such as Alzheimer's disease and Parkinson's disease. For example, AD patients show a more frequent occurrence of some haplotypes such as mutations in the mtDNA at positions 5633, 7476, and 15812 (Chagnon et al., 1999). This is also supported by a dominant female inheritance (Edland et al., 1996), but it is still unclear whether mitochondria play a primary or secondary role in the development of AD, and the role of haplotypes in AD is still controversial. However, mitochondrial polymorphisms do not only show negative effects. In Parkinson's disease, some haplogroups have been suggested to be risk factors, while others have the opposite effect and are thought to be protective against PD (Chinnery & Gomez-Duran, 2018; Khusnutdinova et al., 2008).

The integrity of mtDNA is affected not only by deletions or point mutations in the mtDNA itself, but also by mutations in nuclear DNA. For example, alterations in axonal mRNA transport mechanisms can lead to impaired mitochondrial function and impaired mtDNA maintenance (Aschrafi et al., 2010). In addition, mutations in the genes encoding the mitochondrial DNA polymerase gamma PLOG and the DNA helicase Twinkle, both of which are involved in mtDNA replication, can result in an increase in mtDNA point mutations and deletions or altered copy numbers (Pinto & Moraes, 2014).

Alterations in the mtDNA copy number can lead to pathological effects, as seen for example in the mtDNA depletion syndrome caused by impaired mtDNA maintenance (Pinto & Moraes, 2014). Age-related changes in the mtDNA copy number have also been reported (Clay Montier et al., 2009). However, there are large differences between tissues and/or brain areas. While mtDNA copy numbers in tissues such as muscles decreases with age, the mtDNA copy numbers in the heart are stable (Barazzoni et al., 2000; Wachsmuth et al., 2016). In Alzheimer's and Parkinson's disease patients mtDNA depletion is observed as a phenotype. But here, too, the phenotype only shows up in certain tissues (Dolle et al., 2016; Pyle et al., 2016).

Another cause of changes in mtDNA integrity may be an impaired mitochondrial recycling process (Hara et al., 2006). Defect mitochondria, potentially harbouring altered mtDNA, are suspected to be labelled for degradation by the ubiquitin-protein ligase Parkin in a process called mitophagy. Impairment of this process can lead to a decreased degradation of altered proteins and mitochondria, which results in an accumulation of mtDNA mutations as commonly seen in Parkinson's disease patients (Kitada et al., 1998; Monzio Compagnoni et al., 2020).

In summary, mitochondria play a central role in maintaining a healthy brain. The integrity of mtDNA is influenced by several factors such as the mutation rate, replication and transcription mediated by nuclear DNA-derived proteins and mitochondrial recycling through mitophagy. Most studies addressing mtDNA functionality in neurodegenerative diseases are based on biochemical studies of pooled mitochondria and neglect local information on subcellular and sub-organelle distribution (Morten et al., 2007; Pyle et al., 2016). Especially in highly polarized neuronal cells with different conditions and requirements in each compartment, additional local information may contribute to the understanding of mitochondrial heterogeneity and its functional implications.

To gain insight into the cellular and intracellular variability of mitochondria in neurons, noninvasive analytical methods with high spatial and temporal resolution are needed. Light microscopy is a promising way to follow dynamic processes under natural conditions (Jakobs et al., 2020).

1.5   Microscopy

1.6   Microscopy, a key tool for the life sciences

The first version of a microscope was a brightfield microscope, where the sample is illuminated transmissively by light and the contrast between different structures relies on their attenuation of the transmitted light (Henry, 1740; Wollman et al., 2015). This type of microscopy allowed the first structural observations of cells and their substructures such as mitochondria (Altmann, 1894). It is the easiest microscopy method to implement but the contrast is very low in weakly absorbing samples like mammalian cells (Korzynska et al., 2007). High contrast is an important factor in microscopy to differentiate between features and background.

This limitation in light microscopy was eventually overcome by the development of fluorescence microscopy (Masters, 2010). This method is based on the specific labeling of structures with a fluorophore. A fluorophore can be a chemical compound or a protein that can be excited with light of a specific wavelength and emits fluorescence light with a longer wavelength (Lichtman & Conchello, 2005). Using dichroic mirrors and spectral filters, the excitation and emission light can be separated (Figure 7). This separation of excitation light and emitted light facilitates a high contrast. Fluorescence microscopy is one of the most important techniques for life sciences and has revolutionized our understanding of (dynamic) cellular processes as it can be used to study the spatial distribution of specific proteins or structure in living and fixed cells. In order to visualize a cellular structure by fluorescence microscopy, the choice of the appropriate microscope as well as the appropriate labeling strategy is crucial (Achimovich et al., 2019; Dean & Palmer, 2014). In the following, first a brief overview of the different fluorescence microscopy and nanoscopy techniques as well as the different labelling strategies is given, subsequently the potential of a correlative approach of combining live cell with fixed cell microscopy for the analysis of dynamic cellular events is highlighted.

1.6.1   Microscopy and nanoscopy techniques

The most basic technique is a widefield microscope. Here, the sample is exposed to light in its entirety and the resulting image is directly viewed by the researcher or a camera (Figure 6) (Sanderson et al., 2014). On the other hand, a confocal microscope uses point illumination and a pinhole in front of the detector helps to eliminate out-of-focus signals (Minsky, 1988). The confocal image is built up from the sequentially acquired individual pixels as the illumination is scanned across the sample. By blocking out the off focus light in the back focal plane with the pinhole, the confocal approach reaches a better resolution due to a decreased background (Conchello & Lichtman, 2005). However, the scanning approach is generally slower than the widefield approach. The acquisition speed is important for imaging of live and moving samples to reduce motion artifacts and in high-throughput applications to reduce experiment time.
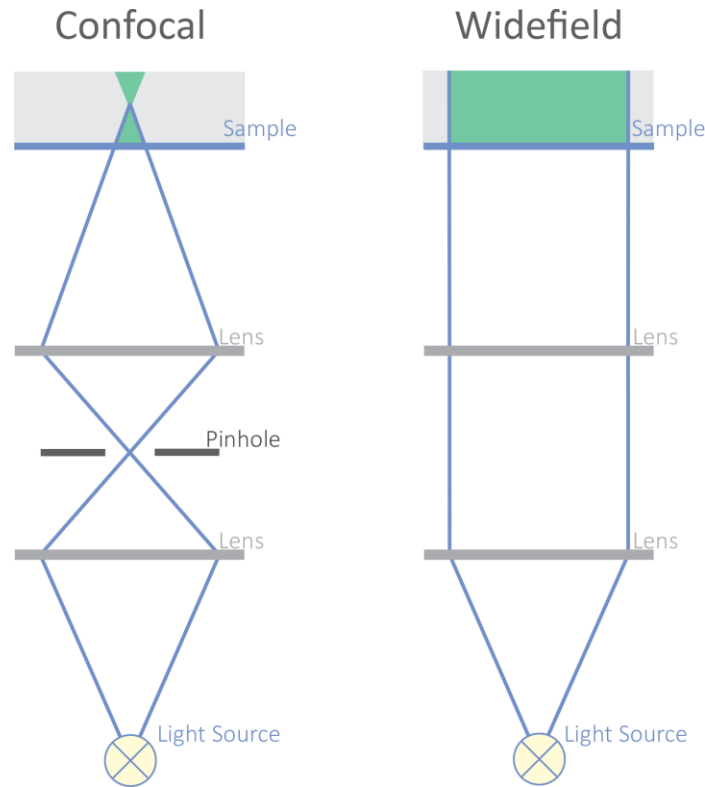
Figure 6: Simplified illustration of a confocal microscope and a widefield microscope. *The left side shows the principle of a confocal microscope. The light is focused on the sample via two lenses in a focal point. A pinhole between the lenses blocks out any off focus light. A widefield microscope is shown on the right. In contrast to the confocal microscope, the entire sample is illuminated here, which is represented by the green area.*

The resolution of conventional light microscopy is fundamentally limited by the diffraction of light (Cremer, 2011). This limit or diffraction barrier was defined by Abbe as follows (Equation 1):

Equation 1

$$d \approx \frac{\lambda}{2n \, \sin \alpha} = \frac{\lambda}{2NA}$$

The distance d is defined by the wavelength λ, the refractive index n and the half angle α of the collected light. The refractive index and the half angle can be combined to give the numerical aperture of the objective, which can reach up to about 1.5 for modern oil objectives. Thereby, the resolution of conventional light microscopy is limited to about 200 nm (Abbe, 1873; Cremer, 2011). Light microscopy uses visible light, but since resolution is highly dependent on wavelength, resolution can be increased using smaller wavelengths. Electron microscopy (EM) takes advantage of this but requires extensive sample preparation not compatible with living cells due to its technical properties such as high vacuum during acquisition.

However, in recent years, the diffraction limit has been overcome by various diffraction-unlimited super-resolution microscopy techniques such as Photoactivated Localization Microscopy (PALM), Stochastic Optical Reconstruction Microscopy (STORM) and Stimulated Emission Depletion (STED) (Betzig et al., 2006; Hell & Wichmann, 1994; Rust et al., 2006). To reach a diffraction-unlimited resolution all methods rely on the separation of neighboring fluorophores. Therefore, fluorophores are used, that are able to alternate between an emitting (on state) and an not emitting state (off state). A distinction can be made between a coordinate stochastic and targeted readout approaches. In stochastic approaches as PALM and STORM (Bates et al., 2013; Betzig et al., 2006) which are based on the widefield approach, the fluorophores randomly change between on and off states (blinking). In the targeted approaches as STED and RESOLFT which are commonly based on a confocal microscope the off state is forced at specific coordinates using a donut shaped laser (Hofmann et al., 2005). The highest resolution to date is reached by recently developed methods combining the approaches such as MINimal photon FLUXes (MINFLUX) and MINSTED (Balzarotti et al., 2017; Weber et al., 2021). Furthermore, several other methods reach an increased resolution but are not diffraction-unlimited such as Structured Illumination Microscopy (SIM), Airy Scan, Rescanning or Image Scanning Microscopy.

All these microscopic methods differ in terms of temporal and spatial resolution as well as in the requirements for optics, fluorophores and preparation. This makes them more or less suitable for each specific research question. Furthermore, the scope of the experiment and the expected results are often limited by these limitations of the microscopes. In recent years, there have been more and more approaches to combine different microscopy methods to compensate for their individual weaknesses. One of these approaches is called correlative microscopy (More in 1.6.4).
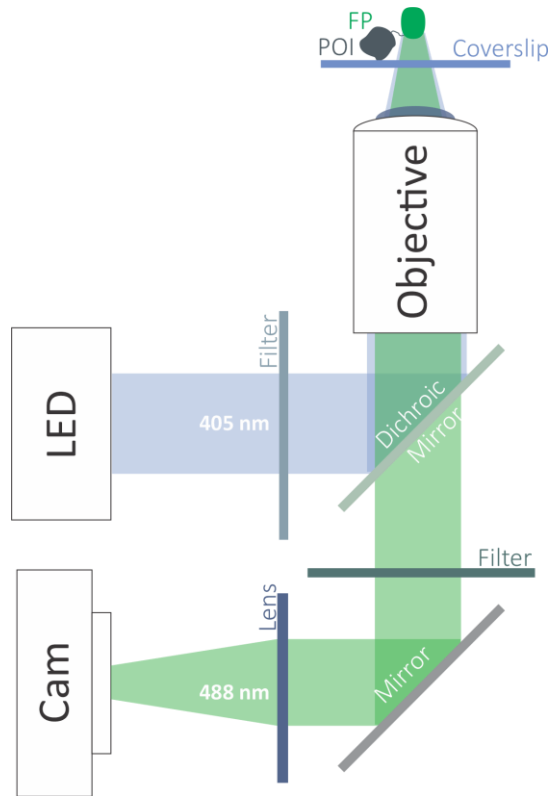
Figure 7: Schematic design of a fluorescence microscope. *Simplified illustration of the basic function of fluorescence microscopy. A fluorescent dye, or here a fluorescent protein (FP) coupled to a protein of interest (POI), is excited with light of a wavelength corresponding to its specific excitation spectrum of the fluorophore (here 405 nm). The emitted fluorescence light is shifted towards a longer wavelength (here 488 nm) and is separated from the excitation light using a dichroic mirror and spectral filter and finally detected by a camera.*

1.6.2 Different labelling strategies for specific use cases

In addition to the technical requirements of the microscope, the labeling of the desired structure or protein with an adequate fluorophore is crucial and equally determines the potential for visualization and subsequent analysis. The challenge here is to label the structure or protein specifically without interfering with its natural localization and function, thereby avoiding the creation of artifacts.

Each fluorophore has characteristic properties such as specific excitation and emission spectra, brightness, fluorescence lifetime, cell permeability, phototoxicity or photostability that determine the imaging parameters and applicable microscope techniques (Shaner et al., 2005). The high-resolution microscopy techniques in particular often have special requirements for suitable fluorophores such as blinking behavior, photostability and brightness (Bottanelli et al., 2016). In general, fluorescent proteins (FPs) are often more compatible with living cells, while synthetic dyes tend to be brighter and more photostable (Dean & Palmer, 2014).

The strategy of labeling the target protein or structure with a fluorophore also has specific requirements and implications on the resolution, contrast and sample health. Parameters to be considered include achievable contrast, specificity, labeling efficiency, and production of artifacts. The strategies employed in this thesis can be grouped into three categories: genetically encoded markers, small molecule dyes, and antibodies (Dean & Palmer, 2014; Han et al., 2021; Li et al., 2017).

The first category, genetically encoded markers are fusion proteins of the protein of interest with an FP or a self-labeling tag. In most cases, these fusion proteins are then overexpressed in the model organism, but modern gene editing methods like CRISPR/Cas9 also allow endogenous tagging of specific proteins (Cong et al., 2013; Mali et al., 2013; Ratz et al., 2015). A wide color range of fluorescent proteins such as GFP, mScarlet, rsEGFP2 optimized for various applications and microscopy techniques is now available (Bindels et al., 2017; Dunsing et al., 2018; Grotjohann et al., 2012; Pédelacq et al., 2006). The range of applications for FPs is becoming even broader thanks to FP-based sensors. They can be used to investigate changes in the intracellular levels of ions, small molecules or pH. Therefore, FP enable a temporally and spatially resolved functional readout. When choosing an FP, the FP's tendency to form dimers and maturation times must be considered additionally to those parameters mentioned for fluorophores (Shaner et al., 2005). The self-labeling tags such as SNAP-tag or HALO-tag are proteins that can react with and covalently bind to chemical dyes (Keppler et al., 2003; Prasher et al., 1992). This technology makes the advantages of synthetic dyes compatible with living cells. However, the dye used for self-labeling must be cell-permeable, which severely limits the amount of dyes that can be used (Wang et al., 2020).

Small molecule dyes are dyes coupled to drugs that bind specifically to certain structures such as DNA, microtubules or actin filaments (Lukinavičius et al., 2014). These dyes are easy to use and do not require prior modification of the organism or cell. To do this in living cells, these dyes have to be cell-permeable and non-cytotoxic. However, to date, the number of structures that can be directly labeled with these small molecules is limited (Terai & Nagano, 2013).

The third strategy, antibody labeling also called immunofluorescence, is a method mostly limited to fixed and permeabilized samples. Here, antibodies with specificity for the protein of interest are covalently labeled with a dye. This is a simple method for labeling endogenous protein amounts and at the same time very versatile, since antibodies can theoretically be produced for a high variety of proteins. Often antibody labeling is performed with a primary antibody specific against the protein of interest and a secondary antibody specific against the primary antibody. In this case, the secondary antibody is labelled with a dye and allows for an indirect detection of the protein of interest. This has the advantage of a greater flexibility and a signal amplifying effect since many secondary antibodies can bind to a single primary antibody. Antibodies are about 15 to 20 nm in size, so staining with a primary and secondary antibody results in an increase of the target structure of at least 30–40 nm (Harris et al., 1998). In nanoscopy, however, the size of the label becomes a problem since the resolution may be smaller than the distance of the dye from the target structure (Pleiner et al., 2015).

1.6.3 Specific techniques for specific question

The tasks for microscopy are constantly extending, but unfortunately there is no microscope that fits all research endeavors. Rather, certain parameters are in conflict with each other, e.g., an increase in spatial resolution is usually accompanied by a decrease in temporal resolution and increasing stress on sample health (Laissue et al., 2017). One of the images used to illustrate this is the "frustration pyramid" as shown in Figure 8. None of these attributes can be changed without simultaneously affecting the others.
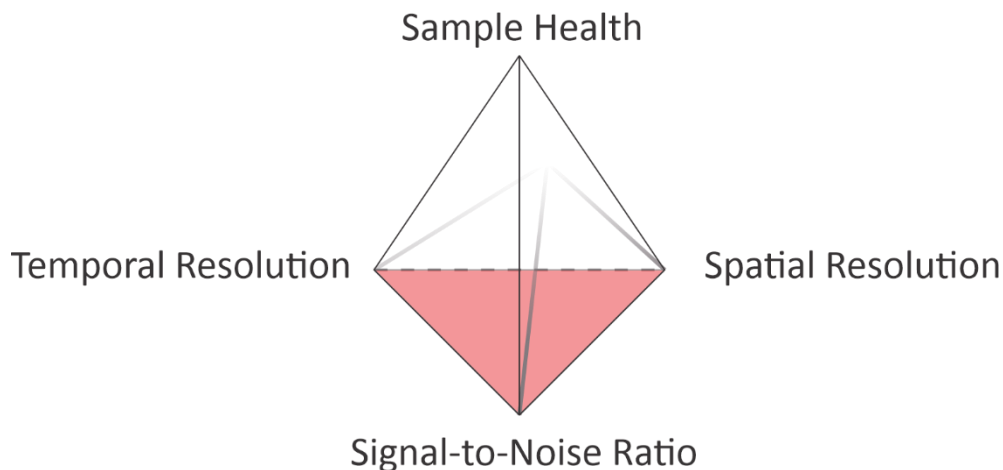
Figure 8: The "Pyramid of frustration" of (live cell) fluorescence microscopy. *This pyramid illustrates the parameters that must be balanced in fluorescence microscopy: The temporal and spatial resolution, the signal-to-noise ratio and the sample health, which is especially important for imaging living cells. No parameter can be improved without affecting another, for instance improving the spatial resolution often results in long imaging times and therefore reduced temporal resolution. For this reason, most microscopy techniques sacrifice one or more parameters to perform exceptionally well in another. One way of compensation for the drawbacks of the specific techniques is to combine microscopy methods to achieve a high temporal and high local resolution in a sequential approach. First, cellular dynamics are imaged with low spatial resolution live cell time-lapse imaging, followed by fixation at a time point of interest and subsequent super-resolution microscopy to analyze the structure with higher precision.*

Therefore, a variety of different microscopy techniques has been developed to address specific research objectives. For example, in live cell microscopy spatial resolution is often balanced against the speed of data acquisition and sample health. The observation of fast dynamic processes in living cells is easily compromised by high light doses, because increasing the load of light potentially damages the sample over time (Laissue et al., 2017). Therefore, wide field microscopy, which has the advantage of high imaging speed and low phototoxicity is often used. It allows imaging of fast processes such as Ca^{2+} fluxes, which can be visualized with special FPs (Chen et al., 2013).

Imaging speed and moreover signal-to-noise ratio are paramount in the observation of protein dynamics for instance using single-molecule FRET (Fluorescence Resonance Energy Transfer) (Hellenkamp et al., 2018). Here, scientists use Förster resonance, in which a fluorescence free energy transfer occurs between two fluorophores of different excitation wavelengths

(Förster, 1948). Since this transfer is dependent on the distance of the two fluorophores this method can be used as a fluorescence ruler in the nm range. In practice, this means that if one fluorophore is excited, it transfers its energy when it is close enough to the other and the second fluorophore emits light/energy. Due to the different wavelengths, both fluorophores can be spectrally distinguished from each other. This allows to observe conformational changes of individual proteins or the binding dynamics of different molecules. These dynamics can take place in the millisecond range, so imaging speed is an important factor. Hence, camera-based systems are often preferred for these types of tasks (Wolf et al., 2021).

Increasing spatial resolution, e.g., through high-resolution microscopy, is often at the expense of longer imaging times and harsh illumination conditions .. For this reason, most super-resolution imaging is done with fixed cells. However, STED microscopy also offers the possibility to observe living cells (Stephan et al., 2019). In this scanning approach, the lower speed can be compensated by using a smaller field of view to reduce motion artifacts, but the necessary higher laser powers limits imaging in terms of sample health.

No microscopy methods is optimal for all possible biological applications, but all have their advantages and disadvantages for specific tasks. One way to compensate for this is correlative microscopy.

1.6.4   Correlative microscopy

In dynamic objects such as living cells, it is rarely possible to capture all facets of a process with a single microscopy technique. Dynamic processes, especially at the subcellular level, are too fast and complex. Hence, to obtain more information from a single sample, the combination of several microscopy methods is required. In neurons, the combination of live and fixed cell microscopy can be used to establish a link between the time-resolved activity of individual synapses and endogenous protein distribution. This would be an important extension of the static biochemical findings.

Common fluorescence correlative microscopy approaches combine conventional fluorescence microscopy with atomic force or electron microscopy. In those applications, fluorescence microscopy is mainly used to detect the location of specific marker proteins or to identify cells with a specific phenotype, these protein locations and cells are then subsequently examined by electron or atomic force microscopy (de Boer et al., 2015; Zhou et al., 2017). Thereby, combining the functional information of a cell with the cellular nanostructure with the highest resolution possible.

But also the correlation of live cell microscopy with fixed cell nanoscopy has been demonstrated (Balint et al., 2013; Tam et al., 2014). Most correlative light microscopy methods use one microscope to perform both widefield live cell microscopy and STORM nanoscopy. However, the experiment often requires a change in the instrumental setup or additional sample preparation steps such as immunostaining between image acquisitions. The main challenge then is to retrieve the previously identified regions of interest (ROI). A common method for this is to use commercially available gridded coverslips, such as those used in the work of Consentio et al. to show mtDNA dynamics in apoptosis (Cosentino et al., 2022). However, these coverslips have their drawbacks in terms of price, altered image quality at the grids, or landmark visibility. Furthermore, fast dynamic processes require a fixation process while imaging to avoid gaps in the temporal history between the last image and the time point of fixation. This was done for example by using a microfluidic platform to fix mitochondria live on-stage (Tam et al., 2014).

This work describes a low-cost cross-platform correlative approach using a newly developed live cell imaging and fixation chamber and computer-assisted retrieval of previously determined ROIs. This approach allowed to investigate the interplay between neuronal and mitochondrial function in relation to mtDNA localization. By using functional imaging of live cells and combining this with antibody labeling of endogenous proteins, it is possible to obtain a large amount of information about a single subject without drastically affecting sensitive cellular processes.

2 Aim of the thesis

Mitochondria carry their own genetic information in the form of multi-protein DNA complexes called nucleoids. Mitochondrial DNA encodes several proteins and subunits of the oxidative phosphorylation system, which is responsible for synthesizing most of the ATP in a cell. Impairments of this system have a direct impact on energy production and thus on the overall activity of the cell. The nervous system in particular, with its energy-intensive neuronal cells, is susceptible to changes in the functional status of the mitochondria.

The highly specialized neuronal cells with their distinct morphology need to maintain their cellular functions even in the most distant parts of their cell body. So far, not much is known about the functional relationship between local neuronal activity and mitochondrial heterogeneity in respect of their nucleoid content.

The aim of this work is to analyse the distribution of mitochondrial nucleoids in neuronal cells and to determine whether there is a functional relationship between local neuronal activity and the presence of mitochondrial DNA.

Initially, nucleoid distribution in neurons will be characterized by immunofluorescence microscopy to gain information on mitochondrial heterogeneity in the different neuronal compartments. To investigate whether there is a relationship between mtDNA distribution and neuronal activity, a new workflow for correlating live cell fluorescence microscopy with immunofluorescence microscopy needs to be established. Finally, this workflow will be used to investigate whether differences in neuronal activity are reflected in altered mtDNA distribution.

3 Material and Methods

3.1 Molecular biology

3.1.1 Cloning

The cloning of the viral plasmids listed below was planned and documented using SnapGen® 6.0.2 (GSL Biotech, Chicago, IL, USA).

3.1.1.1 pAAV-hSyn-4xmts-mScarlet-I

For Gibson Assembly® the following primers were used to amplify the 4xmts-mScarlet-I sequence:

    GCGCAGTCGAGAAGGTACCGATGTCCGTCCTGACGCCG

    ATCGATAAGCTTGATATCGCTTGTACAGCTCGTCCATGC

The AAV Vector featuring a neuron specific promotor hSyn was linearized using BamHI and EcoRI in NEBuffer™ 2.

3.1.1.2 pAAV-hSyn-mNeonGreen-OMP25

OMP25 was amplified using the following primer:

    TGTACAAGTCCGGACTCAGATCT

    AAGCTTTTATCTAGATCCGGTGGATCCCG

The PCR product and the AAV Vector featuring a neuron specific promotor hSyn and mNeonGreen was digested using BsrGI and HindIII in NEBuffer™ 2.

3.1.1.3 pAAV-hSyn-4xmts-SypHer3s

For Gibson Assembly® the following primers were used to amplify the SypHer3s sequence:

    TCCACCGGTCGCCACCATGGATCCATCCGGACCGCTGCACA

    GTTGATTATCGATAAGCTTGATATCTTAAACCGCCTGTTTTAAAACTTTATCGAAATGG

The pAAV-hSyn-4xmts-mScarlet-I plasmid was linearized using NcoI and EcoRV in NEBuffer™ 3.

3.1.1.4 pAAV-hSyn-TFEM-HA

TFEM-HA was amplified using the following primer:

    GGTACCATGAGCGGGTCTGTCCTCT

    TGTACATAGGCGTAGTCGGGCAC

The PCR product and the AAV Vector featuring a neuron specific promotor hSyn were cleaved using BsrGI and KpnI in NEBuffer™ 2.

3.1.2   Plasmid isolation

E. coli DH5α bacteria containing the plasmids were grown over night in LB medium containing 50 µg/µl Ampicillin for at least 12 h at 37 °C with constant shaking. The Quiagen® Plasmid Mini Kit (Hilden, Germany) was used for isolation according to the manufacturer's protocol and the plasmids were eluted in 50 µl H_2O. The DNA concentration was measured using NanoDrop® 1000 spectrophotometer (ThermoFisher Scientific, Waltham, MA, USA).

3.1.3   PCR

DNA fragments were amplified using Q5® DNA polymerase (1 µl) (New England Biolabs® Ipswich, MA, USA), 1 µl of dNTPs (10 mM) (Thermo Fisher Scientific, Waltham, MA, USA), 2.5 µl of each primer (10 µM stock), 5 µl of 5x Q5® Reaction buffer (New England Biolabs® Ipswich, MA, USA), 50 ng of template DNA and filled up to 25 µl with ddH$_2$O. PCR was performed using a Biometra TOne thermal cycler (Analytik Jena, Jena, Thüringen, Germany). The PCR thermocycle protocol was performed as shown in Table 1.

Table 1: PCR thermocycle protocol

98 °C	120 sec	
98 °C	20 sec	
60 °C	30 sec	20 cycles
72 °C	30 sec	
72 °C	120 sec	
4 °C	∞ sec	

3.1.4   Agarose gel electrophoresis

For size-selective purification of DNA fragments, a 1 % agarose gel (Bio-Budget Technologies, Krefeld, North Rhine-Westphalia, Germany) was prepared by mixing the agarose in TAE buffer and boiling the solution. The warm gel was cooled in a mold. The finished gel was immersed in TAE and the pockets were loaded with DNA mixed with loading buffer (Invitrogen™, Carlsbad, CA, USA). The gel was run at 75 V for 45 min. The bands were excised from the gel under UV irradiation after ethidium bromide treatment. DNA was extracted from the gel piece

using the QIAquick® gel extraction kit (Qiagen®, Hilden, Germany) according to the manufacturer's protocol and eluted in 30 µl of H_2O.

3.1.5   Restriction digestion

Restriction sites were selected using SnapGen® and DNA was digested at 37 °C for 1 h. The optimal NEBuffer™ was selected for each restriction enzyme combination based on the manufacturer's efficiency data. The reaction was assembled as described in Table 2.

Table 2: Restriction digestion

DNA	1 µg
10x Buffer	5 µl
Enzyme 1	1 µl
Enzyme 2	1 µl
H_2O	to 50 µl
Sum	**50 µl**

3.1.6   Ligation

For ligation of sticky-end DNA fragments, T4 ligase (Invitrogen™, Carlsbad, CA, USA) was used for 10 min at RT or overnight at 16 °C. After incubation, enzymes were heat inactivated at 65 °C for 10 min. The reaction was assembled as described in Table 3.

Table 3: DNA Ligation

T4 Buffer	2 µl
DNA Vector	50 ng
DNA Insert	37.5 ng
H_2O	to 20 µl
Sum	**20 µl**

3.1.7   Gibson Assembly®

Gibson Assembly® requires overlapping sequences of DNA fragments. Therefore, primers were designed to give an overlap of at least 20 base pairs between the insert and the vector. In this work, the inserts were amplified using the extension primers and the vectors were linearized using a restriction digest. A vector to insert ratio of 1:2 was used for the reaction with approximately 0.03-0.2 pmol insert. DNA was mixed with 10 µl of Gibson Assembly®

Master Mix (New England Biolabs® Ipswich, MA, USA) and filled up to 20 µl with ddH2O. The mixture was incubated at 50 °C for 15 min and then stored on ice.

3.1.8   Sequencing

For sequencing, 1 µg of purified plasmid was mixed with 3 µl of a 10 µM primer and filled up to 15 µl with ddH$_2$0. The DNAs were sent to Microsynth Seqlab (Göttingen, Lower Saxony, Germany).

3.2   Cell biology

3.2.1   Culture of *E. coli*

E. coli Max Efficiency™ Dh5alpha cells were used for plasmid production and cloning. The *E. coli* were grown in LB medium supplemented with 50 µg/ml Ampicillin or on LB agar plates supplemented with 50 µg/ml Ampicillin.

3.2.2   Transformation of *E. coli*

50 µl of aliquoted DH5α cells were thawed on ice and diluted with 70 µl autoclaved and distilled water. 50 µl of the diluted cells were pipetted into an electroporation cuvette (Cell Projects, Harrietsham, Maidstone, UK) along with 1 µl Plasmid (100-300 ng DNA). Transformation was performed at 200 ohms using a BioRad gene pulser. After electroporation, 950 µl of LB medium was added to the cells and incubated for 1 h at 37 °C. Subsequently, 100 µl of the cells were plated on an antibiotic treated agar plate and incubated overnight at 37 °C.

3.2.3   Mammalian cell culture

Hela cells stably expressing Cox8A-SNAP were used for the optimization of the fixation protocol for preserving the mitochondrial structure. This cell line was previously designed and published in this group (Stephan et al., 2019). Cells were grown in high glucose Dulbecco's Modified Eagle Medium (DMEM) mixed with 1 mM Gibco™ GlutaMax™, 1 mM sodium pyruvate and 10 % FBS. Incubation was performed at 37 °C and 5 % CO_2.

3.2.4   SNAP-Staining and cristae fixation of mammalian cells

Cox8a SNAP-stable-expressing HeLa cells were seeded at low density 2 days before imaging. 1 nM SNAP-cell SiR (New England Biolabs® Ipswich, MA, USA) was added to the medium for 30 min, followed by a brief fixation of 15 min with 1 ml of 4 % formaldehyde (FA) and 0.2 % glutaraldehyde (GA) in PHEM buffer added to the medium without washing the living samples

before. Samples were then washed twice in PHEM buffer and blocked in saponin solution for 30 min. Samples were then either mounted for direct STED imaging of the cristae or subsequently immunofluorescently stained as described in the following part.

3.2.5   Immunofluorescence of mammalian cells

The primary antibody diluted in saponin solution was added to the coverslip and incubated overnight at 4 °C. Samples were then washed 3x 60 min in saponin solution at 4 °C. Labeled Fab fragments were used to detect the primary antibody and treated in the same manner as the primary antibody.

3.2.6   Coverglass preparation

The 18 mm 1.5H coverslips (CS) were cleaned by sonication in pure ethanol for 20 min and then dried on a clean work surface. The CS were then placed in 12-well plates and covered with 1 ml of 200 µg/ml poly-L-ornithine (Sigma Aldrich, St. Louis, Missouri, USA) in borate buffer. For same-day plating, CS were incubated for at least 1 h at RT. For use at a later time point, plates could be stored at 4 °C until use. On the day of plating, the CS were washed 3x with H_2O, incubated in H_2O for 1 h, and washed 3x with H_2O again. To ensure sterility, plates were placed under UV light for 1 hr.

3.2.7   Isolation of neuronal cells

The pups of Wistar rats were decapitated with scissors on the day of their birth. First, the skin and then the skull were opened along the sagittal axis of the head to the level of the eyes. The brain was removed with a spatula and placed in a 30-mm dish of ice-cold HBSS for washing and then in a new dish of ice-cold HBSS. Using a stereomicroscope Leica S6 D (Wetzlar, Hessen, Germany), the brain halves were separated with a spatula. Before excising the hippocampus, the meninges were removed with two forceps. The isolated hippocampi were removed with a disposable pipette, washed once in fresh HBSS, and placed on ice in a 15-ml falcon tube soaked in HBSS. Both hippocampi of a brain were collected together. After dissection, the falcon tubes were filled up to 4.5 ml with prewarmed HBSS and 0.5 ml of 2.5 % trypsin (Thermo Fisher Scientific, Waltham, MA, USA) was added. After 18 min of incubation at 37 °C, trypsin was blocked with 10 ml of DMEM and the falcon tubes were centrifuged at 300 rpm for 5 min. The supernatant was discarded, and the hippocampi were washed 3x with warm HBSS. The hippocampi were then homogenized in 6 ml of warm spreading medium by pipetting up and down with a 10 ml pipette. The cell suspension was strained with a 50-µm cell strainer (Corning Life Science, NY, USA) and made up to a total volume of 12 ml with 6 ml of fresh plating medium. For each well, 1 ml of the cell suspension was added to the CS coated with poly-L-ornithine. After 1 hour in the 37 °C, 5 % CO_2, 5 % O_2 incubator Binder CB060 (Tuttlingen, BW, Germany), the medium was replaced with 37° C warm culture medium.

3.2.8 Culture of neurons

Primary rat hippocampal neurons were kept at 37 °C, 5 % CO_2, 5 % O_2 in the incubator (Binder CB060, Tuttlingen, BW, Germany) for 7-15 days in vitro (DIV). The interspace between the wells was filled with ddH$_2$O to reduce evaporation of medium. For standard culture up to DIV15, medium was not changed.

3.2.9 Transduction of neurons

Adeno-associated viruses (AAV1/2) were used for neuronal expression of fusion proteins and fluorescent reporters. AVVs were applied to DIV7 neurons by diluting 1 µl of the AAV solution with 3 ml of fresh medium. 250 µl of the dilution was then added per well of a 12-well plate. Cells were used after at least 7 days depending on the brightness of the structure.

3.2.10 Fixation and permeabilization of neurons

Primary neuronal cells were fixed by adding 4 % FA to PHEM buffer at a 1:1 fixation solution to medium ratio. After 15 min, the mixture was replaced with pure fixation solution for an additional 5 min. Neurons were then permeabilized with 0.2 % Triton in PHEM buffer for 4 min and washed three times in PHEM.

3.2.11 Immunofluorescence of neurons

The fixed, permeabilized neurons were incubated with a primary antibody diluted in PHEM buffer for 1 h at RT or 24 h at 4 °C. After a 20 min wash step with PHEM buffer, the secondary antibody was applied for 1 h and washed again for 1 h.

3.2.12 Antibodies

Table 4: primary and secondary antibodies used in this thesis.

Antigen	Host species	Clone/Cat. no	Vendor	Fluorophore	Dilution
dsDNA	Mouse	HYB331-01	SantaCruz	__	1:200
TFAM	Rabbit	ab131607	Abcam	__	1:400
Bassoon	Chicken	141016	SySy	__	1:400
Shank2	Guinea Pig	162 204	SySy	__	1:500
Neurofilament H	Guinea Pig	171 104	SySy	__	1:500
Cyt-C	Rabbit	6H2.B4	BD Bioscience	StarRed	1:200
Mouse IgG	Goat	515-005-062	Dianova	StarRed	1:200
Mouse IgG	donkey	715-475-150	Jackson/Dianova	DyLight405	1:200
Rabbit IgG	Goat	A11037	Thermo Fisher Scientific	AF594	1:200
Chicken IgG	Goat	ab150169	Abcam	AF488	1:200
Chicken IgG	Goat	703-005-155	Dianova	StarRed	1:200
Guinea Pig IgG	Goat	ab175678	Abcam	AF405	1:200

3.2.13 Mounting of neurons

To remove excess salt, the samples were briefly rinsed with ddH$_2$O. Excess water was absorbed with a paper towel. A drop of Moviol was placed on a coverslip and the sample was placed cell side down. Moviol was allowed to cure overnight prior to imaging.

3.2.14 Virus preparation

AAV1+2 virus particles were produced in a 50-70 % confluent 10-cm dish containing HEK-T cells. For this purpose, HEK cells were transfected with TransIT® (Mirus Bio®, Madison, Wisconsin, USA) according to the manufacturer's protocol and a 1:1:1:1 mixture of helper plasmid, AAV1 plasmid, AAV2 plasmid and a plasmid containing the protein sequence of

interest with a marker. After two days of expression, HEK cells were detached and lysed. For this, the medium was removed and 5 ml of AAV lysis buffer was added. Cells were resuspended by pipetting up and down. The cell solution was transferred to a 15-ml falcon and placed in the -80 °C freezer for 20 min 3 times, followed by 37 °C for 30 min. The cell lysate was centrifuged at 3000 rpm for 10 min and then at 5000 rpm for 3 min. The supernatant was transferred to a sterile centrifuge tube and spun at 20000 rpm at 4 °C for 2 h. The supernatant was then discarded, and the virus pellet resuspended in 150 µl PBS and stored at -80 °C until use.

3.2.15 Plasmids

To assess neuronal activity Ca^{2+} imaging is used. The axonal targeted Ca^{2+} sensor GCaMP6s was purchased from addgene (Plasmid #111262) as plasmid and virus. The AAV were used 1:6000 and kept on the cells for 8 days.
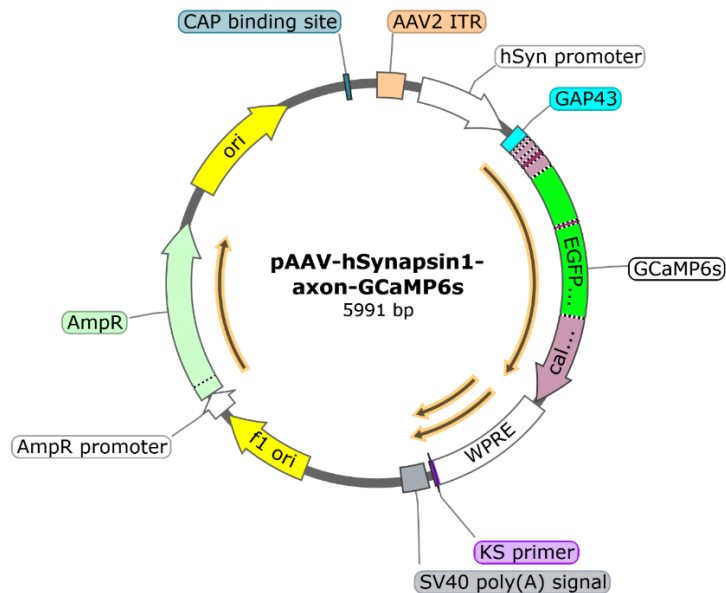
Figure 9: pAAV-hSynapsin1-axon-GCaMP6s. *AAV vector with the neuron specific promotor human Synapsin (hSyn) that drives the expression of the Ca^{2+}-sensor GCaMp6s. The Ca^{2+}-sensor is targeted to the axon by GAP43.* Neuron-specific labeling of mitochondria for use in live and fixed cells was performed with a mitochondrial matrix-targeted mScarlet-I or a mitochondrial OMM-targeted mNeonGreen regulated by a hSyn promoter. This plasmid for the mitochondrial matrix-targeted mScarlet-I was purchased from Addgene (plasmid #98818) and cloned into an AAV vector.
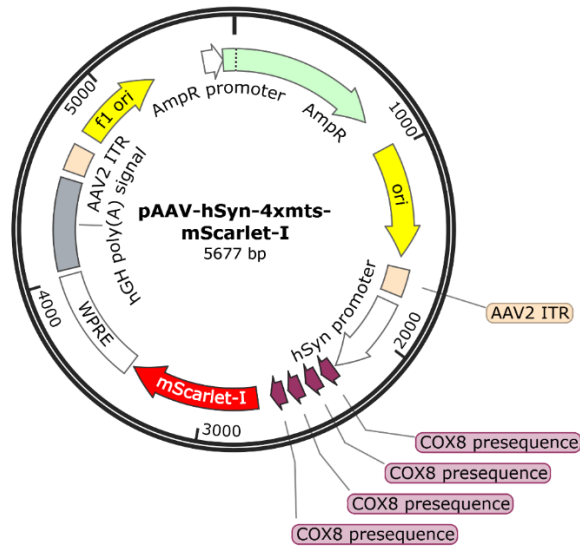
Figure 10: pAAV-hSyn-4xmts-mScarlet-I. AAV vector with the neuron specific promotor human Synapsin (hSyn). The red fluorescent FP mScarlet-I is targeted to the mitochondrial matrix using four repetitions of the Cox8a presequence.

Plasmid harboring the OM25 sequence was a gift from the Bewersdorf Lab and cloned into the vector as described before.
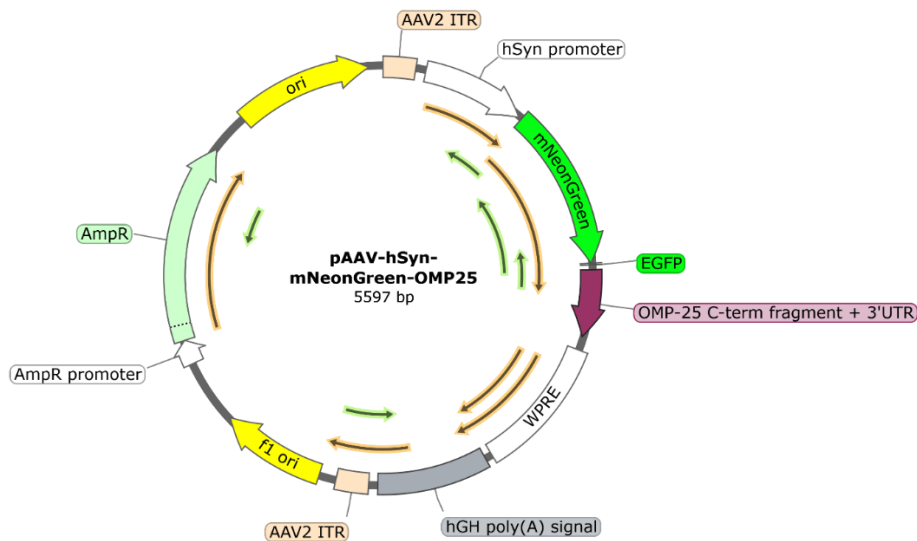
Figure 11: pAAV-hSyn-mNeonGreen-OMP25. AAV vector with the neuron specific promotor human Synapsin (hSyn). The green fluorescent FP mNeonGreen is targeted to the mitochondrial outer membrane using the C-terminal fragment of the OMP25 sequence.

A pH sensor targeting the mitochondrial matrix was used to assess mitochondrial function as a function of nucleoid content. For this purpose, the pH sensor SypHer3s, purchased from Addgene (plasmid #108119), was cloned into an AVV vector containing a neuron-specific promoter hSyn.
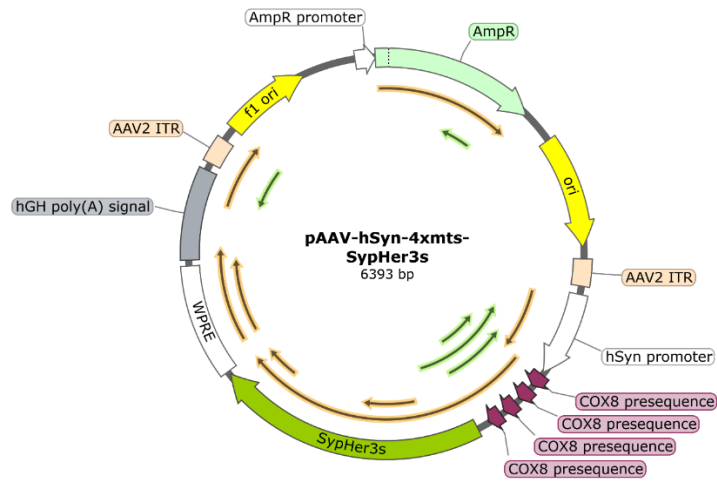
Figure 12: pAAV-hSyn-4xmts-SypHer3s. *AAV vector with the neuron specific promotor human Synapsin (hSyn). The pH sensitive ratiometric, green fluorescent FP SypHer3s is targeted to the mitochondrial matrix using four repetitions of the Cox8a presequence.*

3.3 Microscopy

3.3.1 Widefield imaging

Live cell imaging was performed on an Olympus IX73 (Shinjuku, Tokio, Japan) with an Olympus 64x 1.4 NA oil objective and captured with an sCMOS camera (Hamamatsu Orca Flash4.0 V3). Illumination was provided by a CoolLED pE-4000 and filtered through a Chroma 59908 filter set. To provide optimal conditions for living cells, imaging was performed at 37 °C and 5 % CO_2 using PeCon's cellVivo system (Erbach an der Donau, Baden-Württemberg, Germany). A Märzhäuser Scan IM (Wetzlar, Hessen, Germany) was used as a stage to store the sample positions. A custom-made device was used for electrical stimulation of the neurons, as shown in supplemental Figure 21. The trigger was given by either a pulse generator or an NI card. The settings were fixed at 10 Hz pulses with a signal width of 1 ms, alternating polarizations and 10 V per centimeter between the two parallel platinum electrodes on the sample.

3.3.2 Confocal imaging

Confocal images were acquired with a commercially available Leica SP8 (Wetzlar, Hessen, Germany) equipped with excitation laser lines 405, 488, 458, 476, 496, 514, 561, 633 nm, 3 hybrid and 2 PMT detectors. The objective used was a Leica 64x oil objective 1.4 NA. The 2048x2048 pixel images were acquired at 4 x line average and 200 Hz.

3.3.3 STED imaging

STED images were acquired on an Abberior expertline (Göttingen, Lower Saxony, Germany) using an Olympus 100x oil objective with an NA of 1.4. Fluorophores were excited with a 640 nm and 561 nm LASER and depleted with a 775 nm STED laser. Image settings were set to 15 nm pixel size and a dwell time of 10 µs with 4 line accumulations.

3.3.4 Image analysis

3.3.5 Detection of nucleoids

Confocal images of TFAM or dsDNA were analyzed to detect nucleoid spots. Spots were detected based on the local center of mass (CoM). To avoid detection of pixel fluctuations in a spot, a Gaussian filter with sigma=1 was applied. Then, the background was subtracted using a simple intensity threshold. A scipy algorithm was used to detect the CoM. The resulting coordinates were stored in a Numpy array for further analysis.

3.3.6 Quantification of TFAM levels

To determine the average TFAM signal per nucleoid, TFAM spots were segmented by applying a Gaussian filter with sigma=1, followed by an intensity threshold to subtract background.

Segmentation was then calculated using the Scipy label function. For verification, the CoMs coordinated as described above were checked for overlap with the TFAM signal. The average TFAM signal was calculated in the RAW image at the positions of the verified segments.

3.3.7 Detection of mitochondria

A Gaussian filter with sigma=0.7 was used to detect the mitochondrial signal. An intensity threshold was applied to subtract the background. Then, the Scipy label function was used to isolate individual mitochondria and assign unique numbers to them. In this way, each individual mitochondrion detected could be called separately and analyzed for TFAM content and Bassoon overlap.

3.3.8 Separation of neuronal cells using spectral unmixing

For the spectral separation a Gaussian filter with sigma=1 was applied to reduce pixel variation. Afterwards, the percentage of the FPs detected in every pixel was calculated. Plotting a histogram of the percentages resulting in different peaks representing different cells with different FP ratios. Local maxima of the peaks were calculated. The threshold to isolate the cells was automatically set to the midpoint between the maxima. All pixels belonging to one peak were saved into one channel.

Two different fluorescent proteins targeting the mitochondrial matrix were used to separate the different neuronal cells. Both were transduced with AAVs. The results are neurons expressing only one of both FP and some expressing a mixture of both. The ratio between the two imaged FPs was used to separate different cells. By ensuring that the labeled cells are far enough apart so that the dendrites do not overlap, any mitochondrion with a different FP ratio in an ROI that has a soma as its center can be assumed to be an axonal mitochondrion. Using a custom Python code, the percentage between the two FP was calculated. The different ratios of the cells were then detected by finding the local maxima of the 1D histogram of the ratio. The threshold to isolate the cells was automatically set to the midpoint between the maxima. In this work, it was not of interest to separate all individual cells, but rather to separate the cell located in the center of the ROI from the incoming axons. Therefore, the channel showing soma and dendrites was selected manually, and the other channels were merged for further analysis.

3.3.9 Image registration

The two transmitted light images taken by two different microscopes were analyzed using a Python code (8.2). In the script, unique features of the two images were detected using the SIFT algorithm (Burger & Burge, 2016). The features of the two images were then compared to find similarities between them. This was done using the FLANN algorithm (Suju & Jose, 2017). The brute force algorithm showed a higher number of matches but was much slower, while the FLANN algorithm provided enough matches to proceed. The affine matrix was estimated from the two matched coordinate sets using the estimateAffinePartial2D algorithm from the OpenCV (CV2) package. The resulting affine matrix can be decomposed to obtain the rotation angle x and y translation, as well as the scaling between the images. These metrics were used to calculate the new position of the region of interest of a correlative experiment, as described in the results.

3.3.10 Software

Image analysis was performed either with imageJ or with custom made Python scripts. Used packages were:

Numpy	(Harris et al., 2020)
Scipy	(Virtanen et al., 2020)
Matplotlib	(Hunter, 2007)
Panda	(McKinney, 2010)
Seaborn	(Waskom, 2021)
Statmodels	(Skipper & Perktold, 2010)
CV2	(Bradski, 2000)
Scikit-Image	(Walt. et al., 2014)

3.4   Buffers, media and solutions

Table 5: Collection of buffers used in this thesis

HBSS			(Thermo Fisher Scientific)
Cellculture Medium		**50 ml**	
	DMEM	43 ml	(Thermo Fisher Scientific)
	FBS	5 ml	(Merck Millipore)
	Penicillin Streptavidin 100 U/ml	0.5 ml	(Merck Millipore)
	Sodium Pyruvate	1 mM	(Sigma Aldrich)
Plating Medium		**50 ml**	
	Neurobasal A	48.5 ml	(Gibco)
	B27 Plus	1 ml	(Gibco)
	GlutarMax	0.5 ml	(Thermo Fisher Scientific)
Culture Medium		**50 ml**	
	Neurobasal A	48 ml	(Gibco)
	B27 Plus	1 ml	(Gibco)
	GlutarMax	0.5 ml	(Thermo Fisher Scientific)
	Penicillin Streptavidin 100 U/ml	0.5 ml	(Merck Millipore)
PHEM Buffer			
	Pipes	60 mM	(AppliChem)
	Hepes	25 mM	(AppliChem)
	EGTA	10 mM	(Sigma Aldrich)
	MgCl	2 mM	(Sigma Aldrich)
2x FA			
	Paraformaldehyde	8 g	(Merck)
	H_2O	100 ml	

Saponin solution		**100 ml**	
	Saponin	2 g	(Sigma Aldrich)
	BSA	2 g	(Serva)
	PHEM buffer	100 ml	

0.2 % Triton		**100 ml**	
	Triton X100	0.2 ml	(Merck)
	ddH$_2$O	99.8 ml	

AAV-Lysis buffer		**100 ml**	
	5M NaCl	3 ml	(Sigma Aldrich)
	1M Tris-HCl	5 ml	(Sigma Aldrich)
	ddH$_2$O	92 ml	

4 Results

This work investigates the distribution of nucleoids in neurons and the relationship between neuronal function and the distribution of mtDNA. In addition to more classical experimental approaches, a new correlative microscopy workflow and analysis strategy is introduced to explore the relationship between presynaptic activity and the local presence of nucleoids.

4.1 mtDNA distribution in neuronal mitochondria

In the first part of the thesis, the nucleoid distribution in primary rat hippocampal neurons was studied, to gain deeper understanding if and how it is influenced by the location of the mitochondria in the different neuronal subcompartments. To do so, a suitable and reliable marker for nucleoids had to be found as well as a way to efficiently analyze the intracellular localization of the mitochondria.

4.1.1 Nucleoid visualization

A specific and efficient staining was needed for the visualization of the nucleoids in neuronal cells. These labelling methods needed to be compatible with additional stainings for multicolor imaging and adaptable to different microcopy and nanoscopy techniques.

First, an antibody for double-stranded DNA was used to detect the mitochondrial DNA in the nucleoids. However, this direct antibody-based detection of DNA proofed to be unsuitable as the antibodies showed a strong unspecific binding to the background. This is most probably due to a strong cross reactivity with the poly-L-Lysine coating which is necessary to ensure the attachment of the neuronal cells to the glass coverslip (Supplementary Figure 1). In order to reduce the cross reactivity with the coverslip coating, a short washing step with a high pH buffer (Tris Buffer pH 8.0) after immunofluorescence staining was introduced to neutralize the charge of the coating. However, this harsh treatment was not compatible with all antibodies initially used for co-staining. Furthermore, the background signal was reduced using this procedure but was not completely eliminated. The staining of nucleoids with DNA specific dyes was not feasible, as these dyes can exhibit high background and cannot be fixed easily.

Next, an antibody against TFAM was used for nucleoid detection. TFAM is a mitochondrial transcription factor, which was initially expected to be found at all nucleoids. The antibody shows a specific staining of the nucleoids with low background and excellent contrast (Figure 13 A). The nucleoids are stained throughout the cell in the axon and dendrites (Figure 14). However, during the experimental phase of this work, a publication showed that the TFAM concentration coating the mtDNA is highly variable to enable nucleoid activity (Brüser et al., 2021). The activity is defined as transcription or replication and the study reported that both processes are strongly dependent on the transcription factor TFAM.

To evaluate the robustness of TFAM as a sufficient marker for nucleoids, the number of nucleoids containing detectable levels of TFAM was quantified by immunofluorescence co-staining against DNA as well as markers for transcription (TEFM) and replication (BrdU). Neurons after 14 days in vitro (DIV14) were imaged using a confocal microscope. The images were analyzed using a Python code to calculate the percentage of overlapping signals. To efficiently detect the DNA in the nucleoids, in the dsDNA channel, (Figure 13 A) a background subtraction was applied. Furthermore, an extra channel was recorded for detection of mitochondria using an antibody against Cytochrome C (Cyt-C). From this channel, a binary mask was created and used to subtract the background from the mitochondrial signal.

The analysis showed that 90 % of detected dsDNA also showed a TFAM signal (Figure 13 A). This means that 10 % of the DNA antibody positive nucleoids showed no TFAM signal. When the analysis was performed in the reverse direction, it was found that 99.91% of TFAM spots also have a DNA signal.

Following the findings from Brüser et al. (2021) that the absence of TFAM is inducing nucleoid activity, the colocalization of TFAM with a transcription or a replication marker was tested. This was done to verify that the nucleoids showing no TFAM signal were indeed the active ones. First, actively transcribing nucleoids were analyzed for the presence of TFAM (Figure 13 B). To test this, the Mitochondrial Transcription Elongation Factor TEFM fused to an HA-tag was expressed in neuronal cells as a marker for transcription and visualized using an anti-HA antibody (Figure 13 B). Co-staining with TFAM revealed that only 11% of TEFM-positive sites had TFAM signals. This indicates that the majority of actively transcribing nucleoids have no detectable TFAM signal.

Next, the mtDNA replication was analyzed using BrdU labeling. BrdU is a synthetic nucleoside, which is integrated in the DNA instead of thymidine during replication and can be visualized using an antibody. For this purpose, BrdU was added to the neurons for two hours before fixation and staining. The analysis showed that less than 2.8 % of BrdU signals colocalized with the TFAM staining. This is in line with the finding that active nucleoids are less decorated by TFAM molecules as shown by Brüser et al., 2021 (Figure 13 C).

In conclusion, the finding that TFAM plays a regulatory role for mitochondrial transcription and mtDNA replication by Brüser et al. (2021) is also true for neuronal cells. Most of the transcription or replication active nucleoids in these cells are not represented by a TFAM staining. Direct labeling of the mtDNA would have been the preferred method, but due to the rigorous treatment protocol required, this staining remains problematic. It prevents costaining with other antibodies and requires digital background subtraction due to the remaining unspecificity. For this reason, TFAM staining, although slightly underrepresenting the total number of nucleoids, is the best available compromise for detecting mtDNA in neurons.
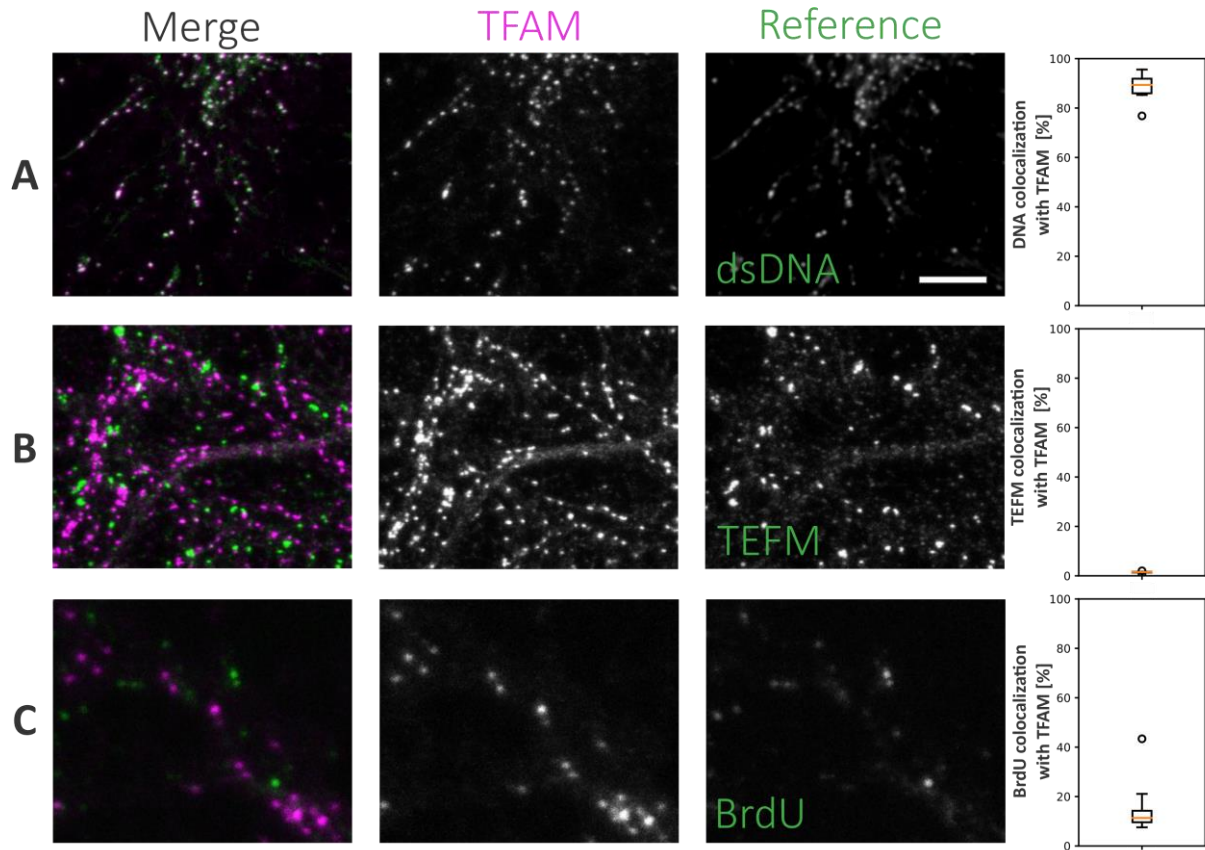
Figure 13: Evaluation of TFAM as a marker for mitochondrial DNA in neurons. *The first column shows the individual overlays of the two rows of fluorescence images on the right. The middle column shows the fluorescence signals of the mitochondrial protein TFAM that was detected via immunofluorescence. The last column shows the fluorescence signals of DNA or nucleoid activity markers. A) TFAM and double-stranded DNA were co-stained with specific antibodies. Due to a high background of the DNA-staining the mtDNA signals were isolated from the background by using a mitochondrial mask. With nearly 90 % colocalization the signals of TFAM and dsDNA (mtDNA) show the highest overlap. B) The TEFM-HA fusion protein was overexpressed in neuronal cells and the HA-tag was detected with primary and secondary antibodies along with TFAM. The calculated average percentage of TEFM spots overlapping with TFAM was about 11 %. C) The synthetic nucleoside BrdU was added to the neuronal cell culture for 2 hours. TFAM as well as BrdU were subsequently detected with antibodies in a co-staining. The overlap of fluorescent BrdU spots with the TFAM signal was calculated and is shown in the graph on the right. It shows that only 2.8 % of TFAM and BrdU signals colocalize. Scale bar: 5 µm.*

4.1.2   Small mitochondria often miss mtDNA

To analyze the distribution of mitochondria and nucleoids in neuronal cells, nucleoids were stained using the TFAM antibody in combination with a Cytochrome C (Cyt-C) antibody to visualize mitochondria. Rat hippocampal neurons 11 days in vitro (DIV 11) were fixed, stained for Cyt-C and TFAM, and imaged with a confocal microscope.

The Cytochrome C signal showed mitochondria varying in length and shape depending on their location in the neuron (Figure 4): mitochondria located in the axon are generally smaller and lack branching compared to those found in the dendrites. Strikingly, TFAM staining showed that not all mitochondria exhibited a TFAM signal and that the mitochondria that did not were comparatively small. (Figure 14). This led to the hypothesis that the majority of mitochondria seen without nucleoids might be located in the axon. However, because dendrites and axons of neighbouring cells are so intertwined, it is difficult to assign mitochondria without nucleoids to individual cells. For this reason, a new method that enables this distinction was developed and is described below.
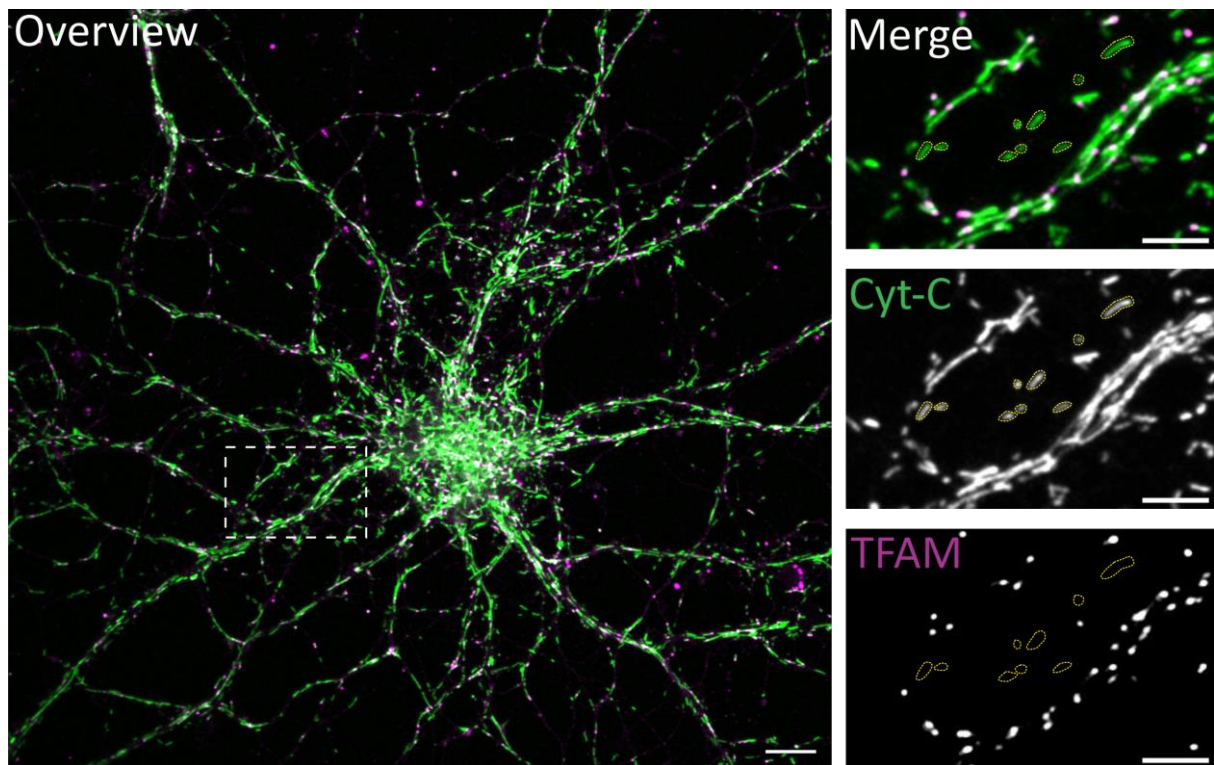
Figure 14: Subpopulation of neuronal mitochondria not harboring TFAM. *Overview of fixed DIV11 neurons stained for Cyt-C as mitochondrial marker and TFAM to represent nucleoids (scale bar 10 µm). The position of the magnification on the right side is highlighted by a dashed box. The magnification is shown as an overlay and the individual channels (scale bar 5 µm). Yellow lines highlight the position of small mitochondria without TFAM signal. Many of the small mitochondria do not show a TFAM signal.*

4.1.3 Analysis of axonal mitochondria

To test the hypothesis that the subset of mitochondria that do not carry a nucleoid are indeed mainly found in the axon and not in the dendrites, a way to automatically separate and analyze axonal and dendrite mitochondria was needed. The high connectivity between neurons makes it difficult to assess axonal and presynaptic mitochondria, especially when they are in close proximity to dendritic mitochondria. Even when using co-staining with an axon marker, it is often impossible to separate axonal and dendritic mitochondria and to assign them to a specific cell (Figure 15 A).
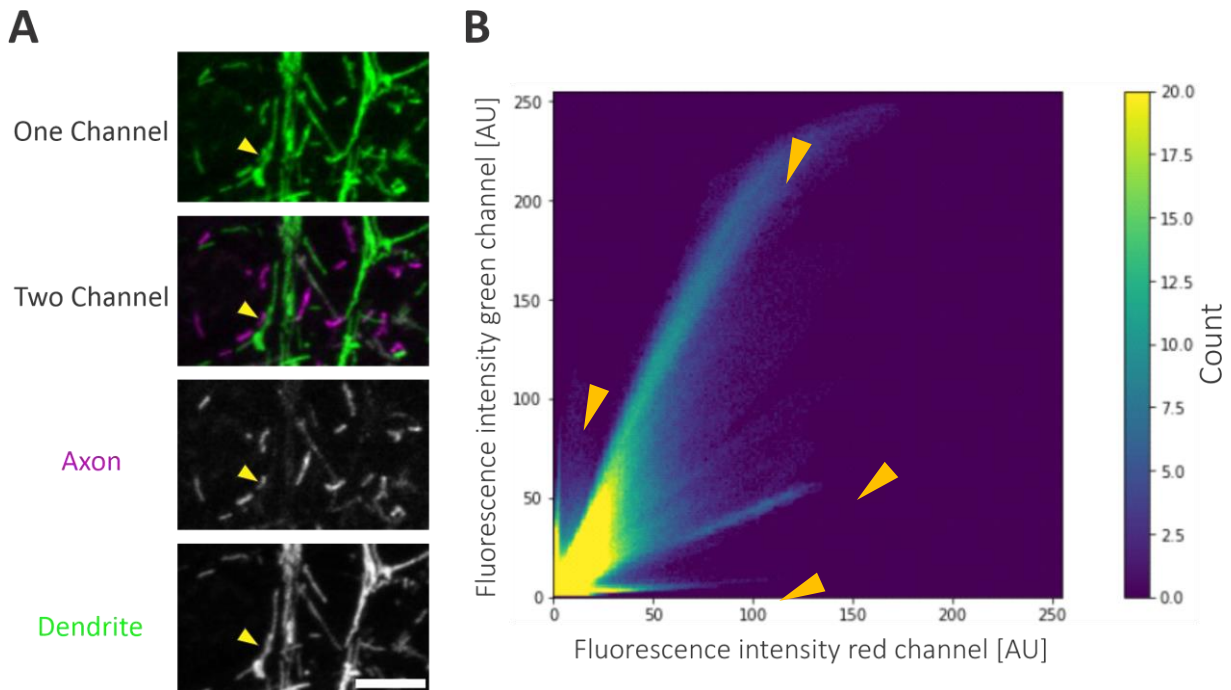
Figure 15: Identification and separation of mitochondria in individual cells. *A) Fluorescence images of a neuronal cell culture expressing different ratios of a red and a green fluorescent protein in their mitochondria simultaneously. Whereas it is impossible to separate the mitochondria in the one channel image, by using two channels for detection, the identification and separation of mitochondria from different cells is possible (indicated by yellow arrows; black and white images show the fluorescence signals of the spectral separated cells). Scale bar: 5 µm. B) A 2D histogram of the fluorescence intensities of the red and the green channel of an image containing the mitochondria of four different cells with four different ratios of the fluorescent proteins as they are indicated by the yellow arrows. Those ratios are used to separate the cells.*

To solve this problem, a principle used in connectomics was applied to distinguish between different neurons in a whole brain: The so-called "brainbow." Here, neurons off transgenic mice express a random ratio of three different FPs. This simultaneous expression of a red, a green, and a blue protein with different ratios results in a variety of uniquely stained neuronal cells allowing the separation of different cells by this ratios (Livet et al., 2007; Weissman et al., 2011). To limit the occupied spectral channels, in this study only mScarlet (red FP) and mNeonGreen (green FP) targeted to the mitochondria were used to transduce neuronal cells. Every transduced cell and thereby every mitochondrion of this cell is characterized by a

specific ratio of fluorescence intensities (Figure 15 B). The ratio is used to assign every pixel and thereby every mitochondrion to a specific cell.

By adapting the transduction efficiency, the labeled neurons with mitochondria-targeting mScarlet (red FP) and mNeonGreen (green FP) were growing far enough apart that the rather short growing dendrites did not overlap. The fluorescence images were acquired by placing the soma of a neuron in the center of the ROI. In this way, any mitochondrion that has a different red-to-green ratio than the mitochondria in the central soma is in an incoming axon of a distant neuron. In this way, the axonal mitochondria can be separated from the dendritic mitochondria of another cell.

This spectral separation of mitochondria from different cells enabled the automated analysis of axonal and dendritic mitochondria using a custom Python script, which was used in the following analysis of the nucleoid distribution in fixed neurons.

4.1.4   Nucleoid distribution in neurites

To assign the mitochondria without nucleoids found in Figure 14 to their subcellular location, neurons after 7 days in vitro (DIV7) were transduced with mitochondrial targeted mScarlet-I and mNeonGreen. At DIV14 cells were fixed and stained with antibody against the nucleoid marker TFAM (Figure 16 A/B). A three-color image was taken using a confocal microscope and the mitochondria were classified as described before (4.1.3) and analyzed for their nucleoid content. The analysis of the fluorescence images confirmed that the majority of mitochondria without a nucleoid were located in the axon. In fact, only 41 % of axonal mitochondria were TFAM-positive, whereas about 90 % of all dendritic mitochondria contained nucleoid with TFAM (Figure 16 C). However, dendritic mitochondria were, on average, larger than the axonal ones. If the number of TFAM spots was normalized with the mitochondrial size, the difference in TFAM distribution between dendrites and axons was not significant (Figure 16 D). For this experiment about ~20,000 mitochondria (biological replication, n=3) were analyzed.

The data demonstrates that there are two subpopulations of mitochondria in neurons: one population with nucleoids and one without. Most mitochondria lacking a nucleoid are small and are located in the axon rather than the dendrites. This raises the questions if the subpopulations are functionally different and how their distribution is regulated. Moreover, it is unclear whether the observed distribution is an age-dependent phenomenon and how it evolves during development. That is why the next experiment focuses on the nucleoid distribution in neurons of different ages.
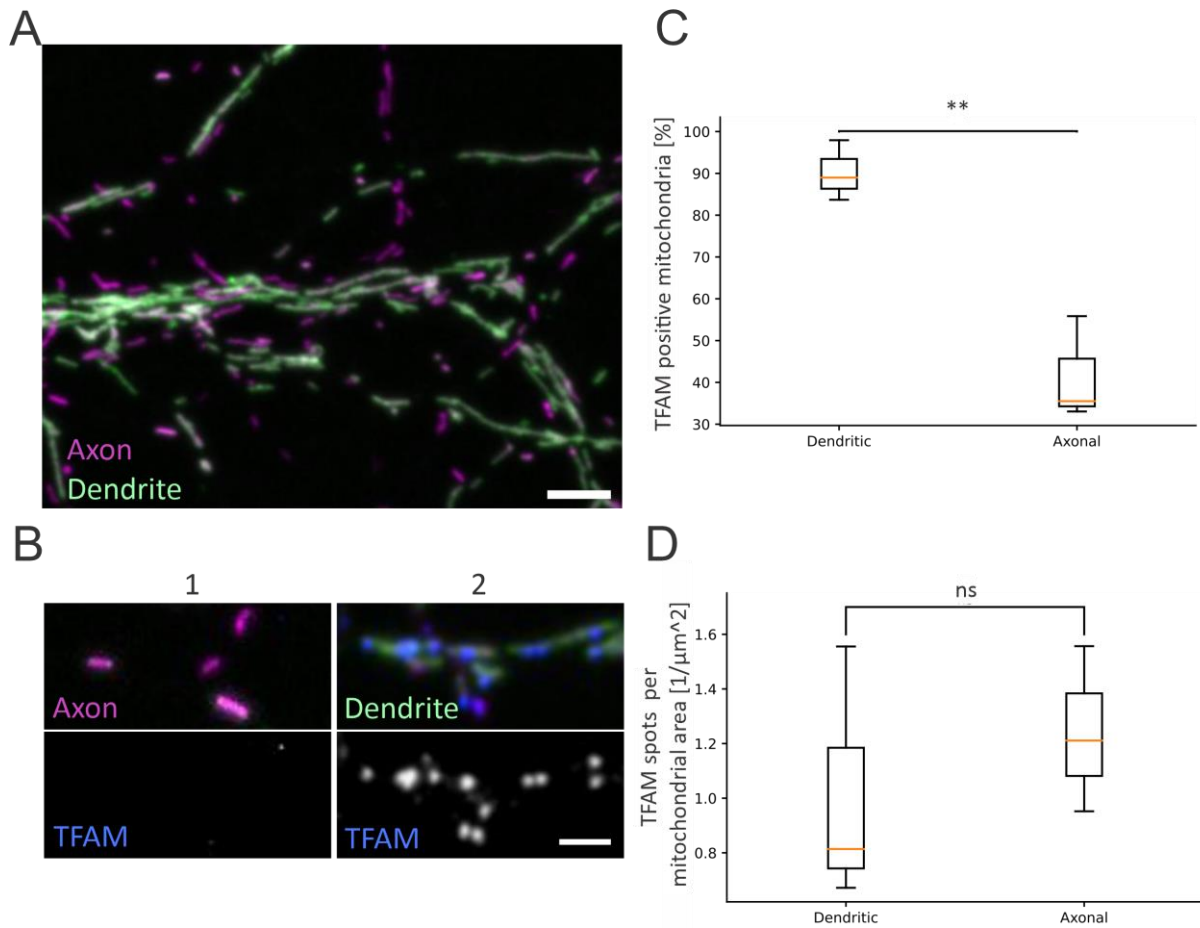
Figure 16: Heterogeneity of TFAM distribution in axonal and dendritic mitochondria. A) Fluorescence images of AAV-transduced DIV-14 neurons expressing mitochondrial mScarlet (magenta) and mitochondrial mNeonGreen (green). The mixed expression allows differentiation between individual cells. Scale bar: 5 μm. B) is showing two different overlay fluorescence images of axonal (1) or dendritic (2) mitochondria together with TFAM signaling (blue) also shown in gray below. Scale bar: 2 μm. C) Calculated percentage of TFAM positive mitochondria in dendrites and axons. The difference of 90 % dendritic TFAM positive mitochondria and 41 % axonal TFAM positive mitochondria is significant (**, p<0.005). D) TFAM spots in dendrites and axons normalized to mitochondrial area. On average dendrites have 1.0 and axons 1.2 TFAM spots per μm² of mitochondrial area. The difference between the two is not significant (ns, p>0.05). For the analysis ~20,000 mitochondria were included (biological replicates, n = 3).

4.1.5 Nucleoid distribution is age dependent

To investigate the dependency of the nucleoid distribution in axons on the age of the neurons, three different time points were chosen. An important developmental step in cultured primary neurons is the formation of functional synapses. To this end, the TFAM distribution in axonal mitochondria was compared at DIV7, DIV11, and DIV15. The time points were chosen to represent crucial stages of synaptogenesis. Before DIV7 little to no functional synapses are expected and at DIV15 most synapses should have formed. Unfortunately, the expression of the AAV-transduced FPs in DIV7 neurons lead to an impaired growth of the cells in culture and rendered the Brainbow method described above useless. Instead, the cells in this experiment

were stained with antibodies only. Mitochondria are visualized with an anti-Cyt-C antibody and an antibody against Neurofilament-H (NF) was used as a marker for the axon. Nucleoids were stained with TFAM and presynapses with the active zone protein Bassoon. The disadvantage of assigning mitochondria to the axon by staining with antibodies alone is that axonal mitochondria that overlap with dendritic mitochondria cannot be separated. In addition, the antibody against Neurofilament-H appears to stain only a portion of the axons present.
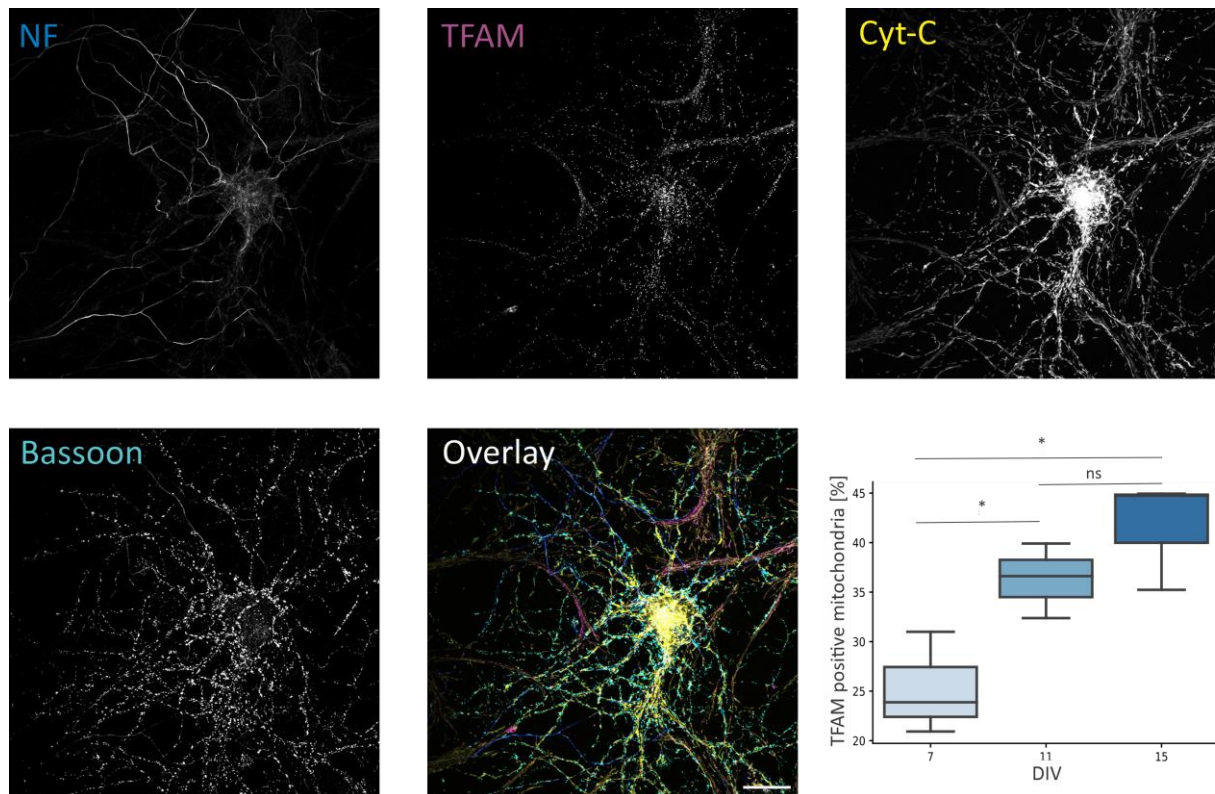
Figure 17: TFAM occurrence in axonal mitochondria increased between DIV7 and DIV15. *Neurons were isolated from rats, cultured and after 7, 11 and 15 days in vitro (DIV) fixed and immunolabelled against Cytochrome-c as mitochondrial marker, TFAM as nucleoid marker, Neurofilament-H (NF) as an axon marker and Bassoon as presynapse marker as shown by the example image (scale bar: 25 µm). The percentage of axonal mitochondria containing TFAM was plotted for 7, 11 and 15 days in vitro. Over time there is a significant (*, p<0.05) increase from DIV7 with on average 25 % TFAM positive mitochondria to DIV11 36 % mitochondria harboring mtDNA on average. Between DIV11 and DIV15 there is a small, not significant increase in the mean to 41 % (ns, p>0.05). Significance was calculated using a t-test using 176 images (biological replicate, n=3).*

The analysis of the immunofluorescence images showed that with increasing neuron age the percentage of TFAM-positive mitochondria in axons increases, from 25 % at DIV7 to 36 % at DIV11, to 41 % at DIV15. However, the slight increase between DIV11 and DIV15 from 36 % to 41 % was not significant. Although the total number of axonal TFAM-positive mitochondria increases by DIV15, more than half of axonal mitochondria still do not contain a nucleoid.

The time points chosen were based on references from the literature to best represent the development of synaptogenesis. However, the formation of functional synapses and neuronal connectivity are highly dependent on cultivation conditions, neuronal density, and the presence of glial cells, which may vary from experiment to experiment. Therefore, presynaptic density was analyzed using Bassoon staining of the same data set as in Figure 17. The number of presynapses detected by Bassoon staining increased significantly from DIV7 to DIV11 (Figure 18 A). However, it did not increase between DIV11 and DIV15. Instead, the average synapse area increases significantly from DIV11 to DIV15 (Figure 18 B), which is rather constant between DIV7 and DIV11.

The results suggest a correlation between the increase in axonal mitochondria containing TFAM and the number of presynapses over time.
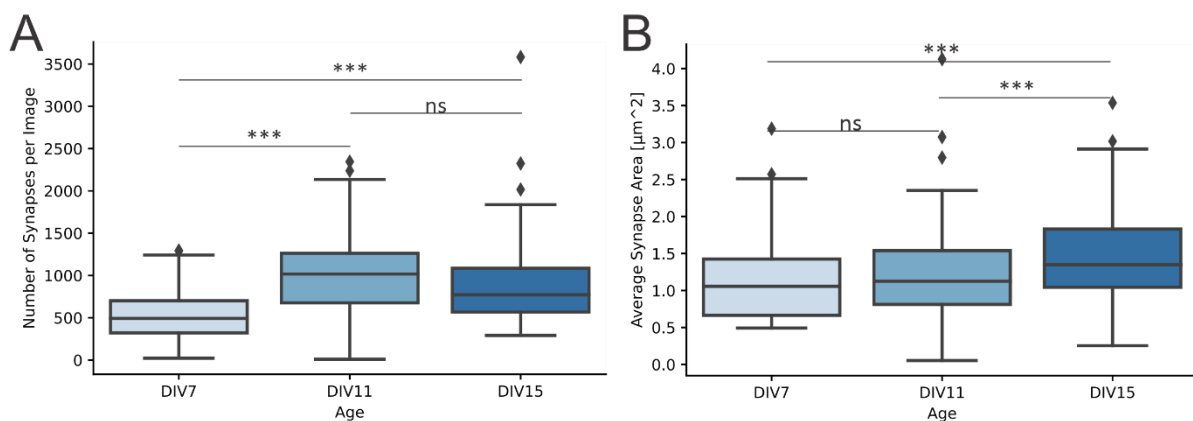
Figure 18: Change in the total number and size of synapses with increasing age of neurons. *The same data set as in Figure 17 was analyzed for the overall number of presynapses and their average size at the corresponding time points. A) The number of synapses per image was counted for the indicated time points. There is a significant increase in number of presynapses between DIV7 and DIV11 as well as DIV7 and DIV15, respectively (***, p<0.001). Between DIV11 and DIV15 there is no significant change (ns, p>0.05). B) The average synapse area in μm^2 at the indicated different age. The increase in synapse size between DIV11 and DIV15 is significant (***, p<0.001). Significance was calculated using a t-test using 176 images (n=3).*

The experiment showed that the number of axonal mitochondria with nucleoids increases with age and correlates with the number of presynapses and the size of the active zone. It also showed that between DIV11 and DIV15 the synaptogenesis seemed to be complete and changes in the number of TFAM-positive mitochondria were no longer significant. For this reason, the following closer look into the distribution of nucleoids in the axon and the presynaptic sites was done on cells grown for DIV14.

4.1.6   mtDNA presence is location dependent

The previous experiments revealed that the majority of mitochondria located in the axon do not carry a nucleoid. Yet, there is still a subpopulation of TFAM-positive mitochondria in this neuronal subcompartment. To get a more detailed view on their distribution, DIV14 neurons transduced with mitochondrial targeted mScarlet-I and mNeonGreen were fixed and immunolabeled with antibodies against TFAM and Bassoon and subsequently imaged on a confocal microscope. Presynaptic mitochondria were defined by the colocalization of the Bassoon signal with the mScarlet/mNeonGreen signal (Overlap > 0.05 μm^2).

Image analysis on the data showed that presynaptic mitochondria contained significantly (***, p<0.001) more often nucleoids (59 %) than non-synaptic axonal mitochondria (39 %, Figure 19). The experiment was performed three times (n=3). The analysis showed a significant difference in the ratio of TFAM positive mitochondria in presynapses and non-synaptic mitochondria in axons but also a high variation between the different experiments. Because of the higher energy demand in the presynapse, the demands on the mitochondria are expected to be higher than on the non-synaptic axonal mitochondria raising the question if there is a functional link to the selection of mitochondria with or without nucleoids.
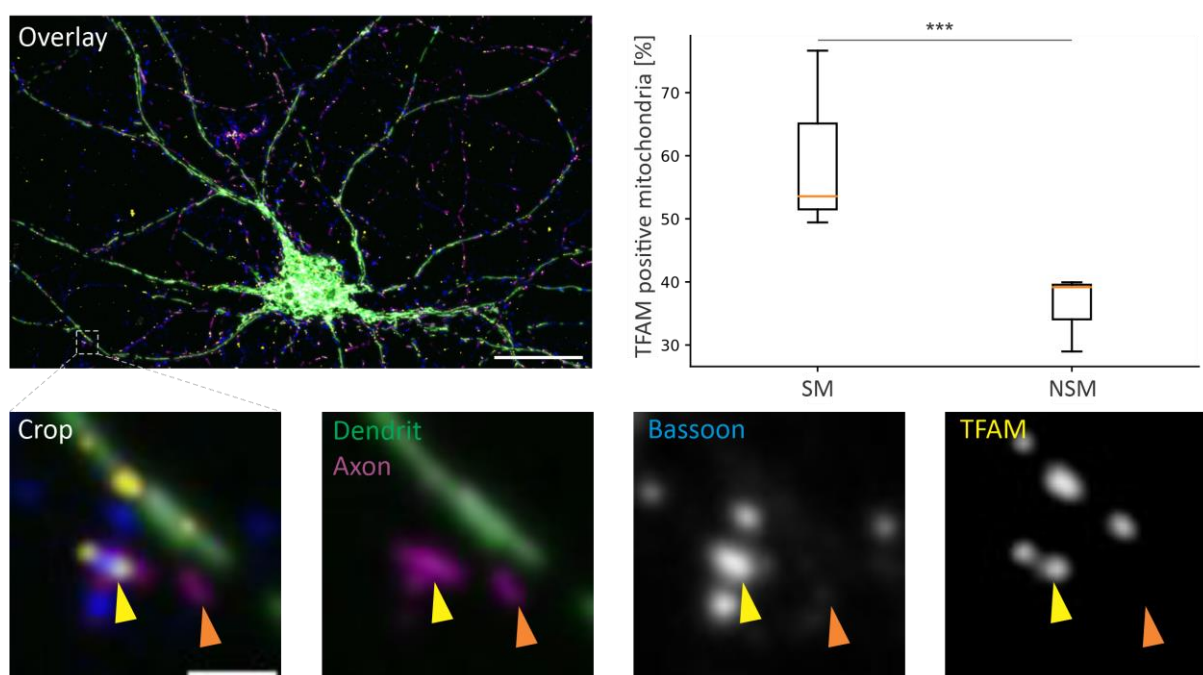
Figure 19: Presynaptic mitochondria more often carry mtDNA than non-synaptic mitochondria. Neuronal cell cultures expressing mitochondrial mScarlet-I and mitochondrial mNeonGreen were analyzed and axonal and dendritic mitochondria classified as previously described. Immunofluorescence labeling of Bassoon (blue) as synaptic marker was used to decide whether the mitochondria were synaptic or non-synaptic and TFAM staining (yellow) was used to distinguish between mitochondria with and without nucleoids (Overlay scale bar: 25 μm and Crop scale bar: 2 μm). Yellow arrow in the Crop image is pointing to a presynaptic mitochondrion harboring nucleoids. Orange arrow point to a non-synaptic axonal mitochondrion. The analysis shows that 59 % of synaptic mitochondria (SM) and 36 % of non-synaptic mitochondria (NSM) carry nucleoids. The difference

between SM and NSM is significant (***, p<0.001). Significance was calculated using a two-way ANOVA including ~13,000 mitochondria (n=3).

The data set in combination with an automated analysis enabled a further analysis. Hence, the size of mitochondria was compared with their TFAM content and intracellular localization (Figure 20 A). On average, non-synaptic axonal mitochondria containing TFAM had an area of 0.56 µm^2 (NSM +), non-synaptic axonal mitochondria without TFAM of 0.36 µm^2 (NSM -). Overall, mitochondria without TFAM signal are smaller than mitochondria with TFAM in the same location. Furthermore, on average, synaptic mitochondria containing TFAM had an area of 1.18 µm^2 (SM +), synaptic axonal mitochondria without TFAM of 0.51 µm^2 (SM +) and additionally, non-synaptic mitochondria appeared to be smaller than presynaptic mitochondria.

In addition, the number of TFAM spots per mitochondrial area was quantified (Figure 20 B). Here the analysis showed that the size of the mitochondrial area corresponds with the number of present mtDNA molecules. In general, the smaller the mitochondrion, the fewer nucleoids it contains, or the larger a mitochondrion, the more nucleoids it contains. This trend is roughly linear up to nine nucleoids per mitochondrion, after which the data are too sparse to draw a conclusion. Furthermore, with the size of the mitochondria the probability increases that not single mitochondria, but several clustered mitochondria are measured.
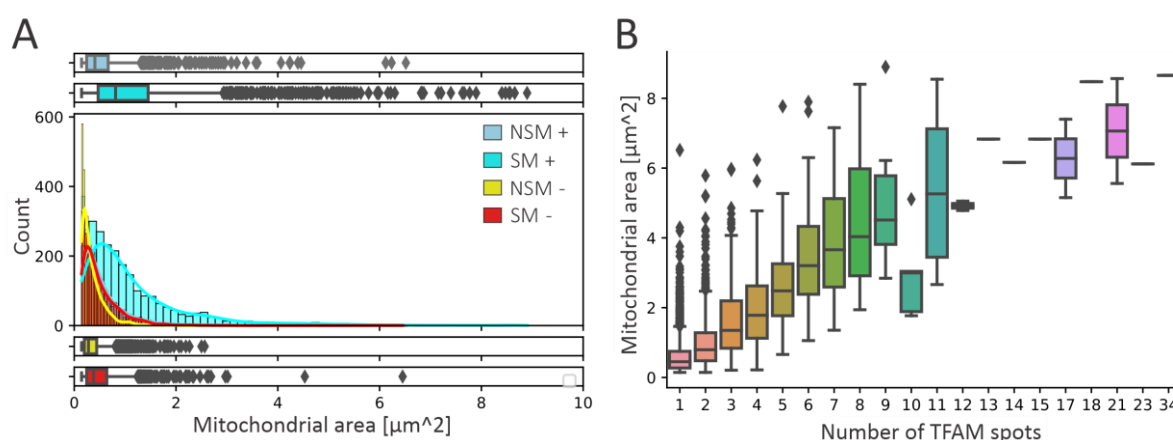
Figure 20: Correlation between mitochondrial size, nucleoid content and location. *The same data set as in Figure 17 was used for this analysis. The mitochondrial size was calculated as the amount of pixels occupied by the fluorescence signal. A) Size distribution plot of mitochondrial with (+) or without (-) TFAM signal and located in a presynapse (SM) or axonal mitochondria without synapse-association (NSM). On average, TFAM-positive mitochondria (1.18 µm^2 SM+, 0.56 µm^2 NSM+) are significantly (p<0.001) larger than TFAM-negative ones (0.51 µm^2 SM-, 0.36 µm^2 NSM-) in the same location. Also, synaptic mitochondria (SM) are larger than non-synaptic mitochondria (NSM). The size of mitochondria harboring mtDNA exhibit a distribution over a wider size range compared to mitochondria without mtDNA. B) Mitochondrial size (area in pixels) is plotted against the number of TFAM spots they harbor. The analysis shows a dependency between mitochondrial size and increasing number of TFAM spots.*

The finding that the majority of mitochondria in the axon lack nucleoids and that TFAM-positive mitochondria are enriched in the presynapse led to the assumption that mitochondria containing a nucleoid are preferentially selected to high energy-demanding areas such as the synaptic site. To determine whether the increased localization of mitochondria with nucleoids in the presynapse is due to functional selection driven by increased demands in the presynapse, a readout of actual neuronal activity and nucleoid content of mitochondria is required. To this end, an approach combining imaging in living cells and quantification of nucleoids in fixed cells is needed. In the following chapter, the development of a correlative microscopy approach is presented.

4.2 Correlative live and fixed cell microscopy

Cells constantly undergo dynamic processes to maintain their status-quo or adapt to changes in their environment. Various microscopy methods have been developed to study these processes, each method having its specific application focus and sample requirements. Widefield microscopy has a high frame rate, which makes it very suitable for the acquisition of fast and dynamic processes but with the downside of a low spatial resolution. Super-resolution microscopy (nanoscopy) techniques, such as STED or MINFLUX, on the other side, provide a spatial resolution well below the diffraction limit but are rather slow (Balzarotti et al., 2017; Hell & Wichmann, 1994). A possible approach to compensate for the individual disadvantages of the specific microscopy methods is the sequential acquisition of the same sample with the different methods: Correlative live and fixed cell microscopy.

In the following the development of a workflow combining live cell imaging on a widefield microscope, followed by on-stage fixation during image acquisition, immunofluorescence staining, and finally, using a confocal microscope, imaging of the same region previously identified during live cell acquisition is described. This setup and workflow is then used to correlate the activity of living neurons and the nucleoid content of their mitochondria.

4.2.1 Experimental setup

The setup used in this work is based on a widefield microscope that was modified to meet the specific requirements of live cell imaging and fixation on the stage needed for the experiments (Figure 21). To this end, the illumination light, fluorescence filters, camera and microscope stage were changed. In addition, an automated focus control was implemented, the on-stage fixation process was developed, and a compatible field stimulation device was built Supplementary Figure 5.
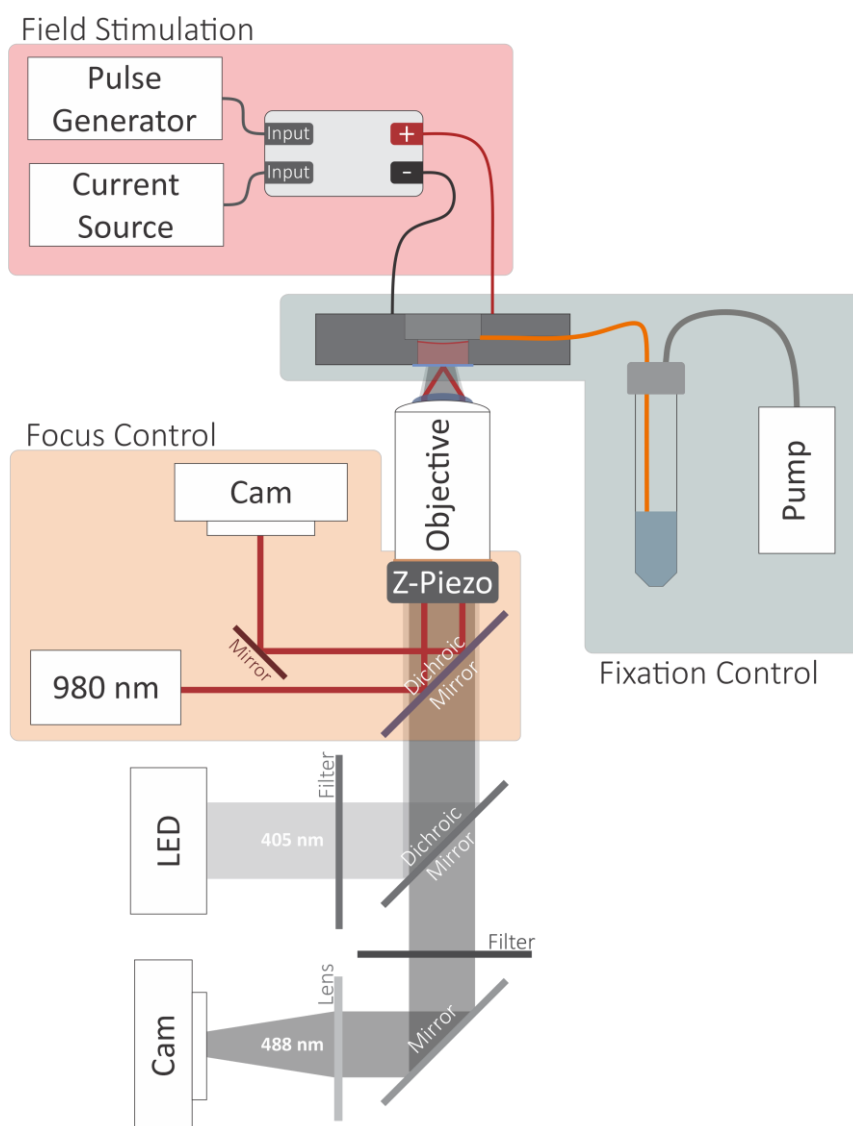
Figure 21: Schematic of the correlative fluorescence live cell microscopy with on stage fixation. *Illustration of the setup and its components used in this work. The grey box shows the fixation control with the pneumatic pump and the fixation chamber developed in this work. The orange box frames the custom-built autofocus control for stable imaging during and after fixation. The red box contains the field stimulation, which was custom made and used to trigger long term potentiation of the neuronal cells.*

4.2.1.1   Microscope

The microscope used for live cell imaging was a widefield fluorescence microscope (Olympus IX73) with a 100x/1.4 NA Olympus oil objective. To improve the signal-to-noise ratio in low-light conditions, the standard Olympus camera was replaced with an OrcaFlash 4.0 V3 sCMOS camera (Hamamatsu, Shizuoka, Japan). The use of this camera-based system has the advantage of a high-speed image acquisition combined with low intensity illumination and a high sensitivity, resulting in low phototoxicity during live cell acquisition. The low axial resolution of a widefield microscope is of less concern when applied to neuronal cell cultures, because the focus in this work is on the neurites, which grow as thin structures close to the coverslip (Figure 22). Neurites (A) can be imaged with low background and therefore high

contrast, while the three-dimensional structure of the soma (B) results in increased background.

To increase the speed of multicolor imaging, the halogen light source was replaced by a pE-4000 CoolLED (Andover, UK) with 16 LEDs of different wavelengths from 365 nm to 770 nm coupled with a multiband filter set. The CoolLED in combination with a multiband filter cube allows rapid switching between excitation wavelengths without the need to mechanically change the filter system during multi-color imaging. This allows fast consecutive acquisition of several fluorescence channels, reducing motion artifacts between the channels.
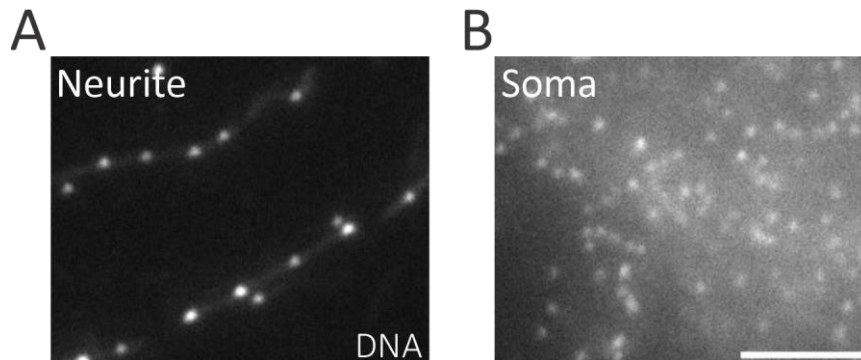
Figure 22: Widefield images of neurite and soma. Widefield live cell fluorescence images of neuronal subcompartments. The DNA was stained with the live cell dye PC3. (A)Low background signal in the flat and thin neurites. (B) In contrast, a high background is visible in the Soma, masking the fluorescence signals of the nucleoids in the mitochondria. Scale bar: 5 µm

4.2.1.2 On-stage fixation chamber

In order to be able to fix the cells on the stage at a given time point depending on the monitored cellular dynamics, a special specimen holder was designed (Figure 23). The holder was designed to be cost effective, easy to build and to use. It was cut from a piece of polyetheretherketone (PEEK) with the length and width dimensions of a standard microscope slide (26 mm x 76 mm), to fit any standard inverted microscope setup. The holder contains a horizontal central channel for the application of the fixation solution and a center hole with two diameters forming a chamber with a step (Figure 23, Figure 24 A). A small ledge is drilled at the bottom of the chamber for convenient insertion of a coverslip, which, once inserted, sits flush with the bottom of the chamber. The fixation channel delivers the fixative to the upper part of the chamber, while the culture medium is located in the lower part of the chamber.
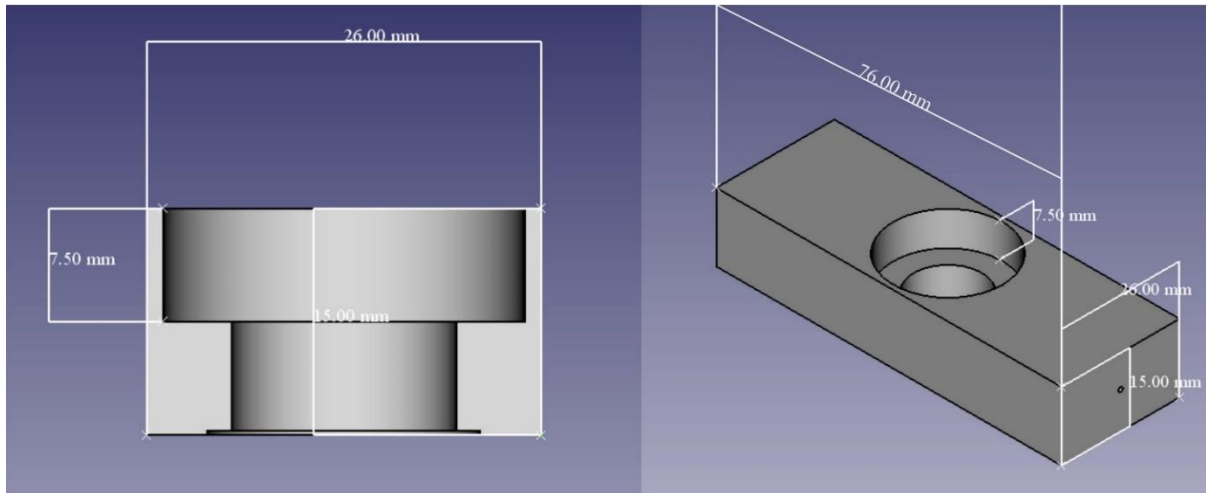
Figure 23: CAD drawing of the on stage fixation chamber. *The left side shows a side view of the main chamber with two different diameters and a small cavity at the bottom to accommodate the cover glass. The right side shows an overview of the chamber with its dimensions.*

A benefit of this design compared to a closed channel or diffusion devise that are commonly used is that installing and changing the fixation solution is easy without caring about remaining air bubbles or formaldehyde in the piping system, which could harm the cells. This is due to the separation of cells and culture medium at the bottom and fixative inlet at the top above the step. When the fixation protocol is started, the surface tension of the inflowing fixative causes a drop with a volume of about 500 μl at the edge of the step until it collapses into the medium all at once (Figure 24 B-C). This rapid addition of a large volume of fixative ensures a fast mixing with the cell culture medium and thus a fast fixation of the imaged cells.

The fixation chamber was designed to house coverslips with a diameter of 18 mm, which was tailored to the standard culturing conditions under which neurons are grown in 12 well plates. For the chamber assembly, the coverslip is taken from the 12 well plate and then mounted on the bottom of the chamber using a two compound glue (picodent twinsil). The design only allows for adding fluids to the chamber without the possibility to drain the present medium, which showed to be beneficial in terms of fixation as well as stability of the setup as presented in the following.
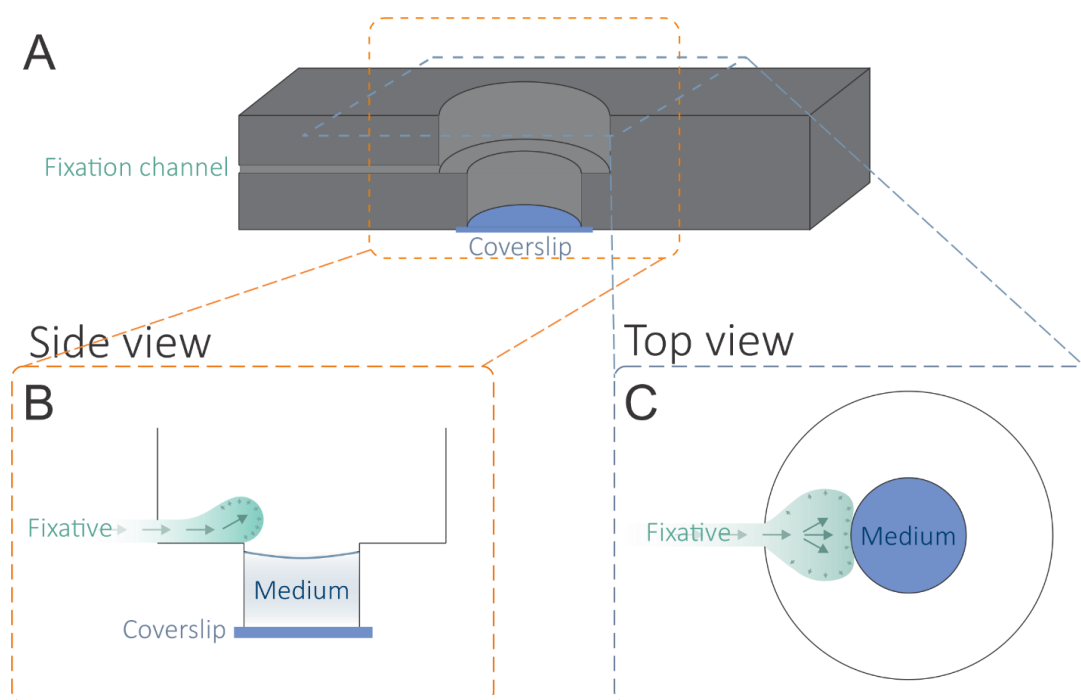
Figure 24: Illustration of the fixation process on the stage. *A) Cross-section of the fixation chamber with the fixation channel coming from the left and the main cavity in the center with two different diameters forming a stage separating medium and fixative. The cavity is closed at the bottom with the cover glass on which the neurons were seeded. B) Side view of the cavity showing the inflow of the fixative. Initially it forms a drop on the step before it eventually collapses into the medium. C) Top view into the fixation chamber showing the enlarged front of the inflowing fixative on the step.*

4.2.1.3 Focus control

During long imaging times as well as during the fixation process on the stage, a drift in the focus level can occur. To correct potential drifts, a laser-based focus control system was developed for the setup. For this purpose, a 980 nm laser (the wavelength is outside of the imaging window) was aligned to produce a total internal reflection at the coverslip; the reflected beam is going back through the objective and is then detected by another camera.

This focus control relies on the fact that, changes in the distance between the lens and the cover glass result in a change in the distance between the incoming and reflected laser light. The laser localization and its changes are recorded by the camera, and the center position of the beam is measured using a Center of Mass (CoM) algorithm in LabView. Position determination by CoM is less precise than using a Gaussian fit, but ultimately faster, which is advantageous in this application. Due to the comparatively poor Z-resolution of a widefield microscope, fluctuations in the single-digit nanometer range are not disturbing. This measured localization change corresponding to the distance can be used to feedback to a z-piezo stage positioned below the objective to return to the initial focus distance. A LabView program was written for the feedback loop that corrects the focus every 150 ms.

With this program the piezo position and the measured sample position can be recorded as shown in Figure 25. During measurement the on-stage fixation is initialized as marked by the

yellow arrow. Using this autofocus, the measured sample position around the focal plane at 0 µm varies with a standard deviation of only 0.0028 µm. Even after a drift caused by the application of the fixation solution, the sample position is immediately corrected and deviates only 17 nm from the focal plane for one time point (150 ms), while the piezo is correcting a drift of 680 nm.
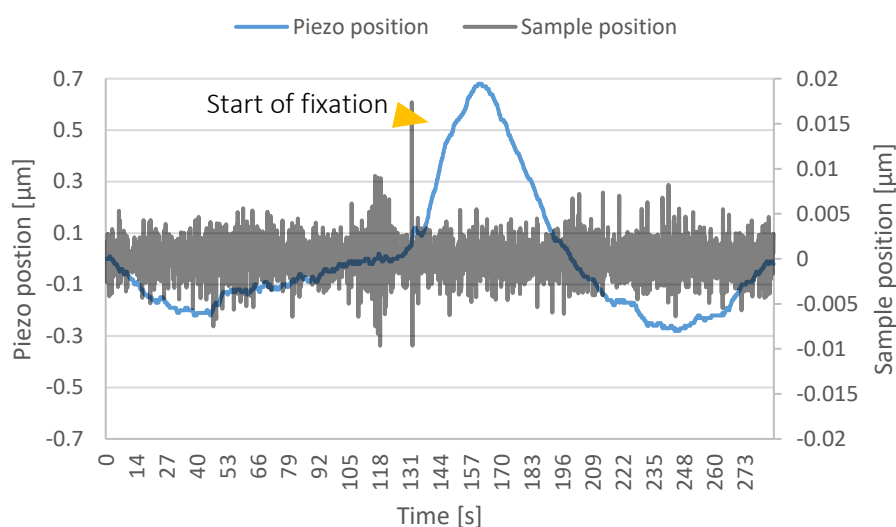
Figure 25: The autofocus effectively stabilizes the stage during imaging also during fixation. *The graph shows the relative positions of the piezo (blue) and the measured sample position (grey) from the focus level at zero over the time of 5 min. The yellow arrow indicates the time at which the fixative collapses into the medium. A thermally induced focus shift follows, which is corrected by the piezo while the sample position continues to fluctuate about the focal plane. The SD of the sample position is 0.0028 µm and 0.2434 µm of the piezo with a maximum distance to focus of 0.017 µm (sample) and 0.68 µm (piezo). The peak marked with the yellow arrow in the sample position is only spanning one measure point of 150 ms after which the stage is back at the initial focal position.*

Furthermore, the LabView program continuously analyses the image of the reflected laser. Changes in the refractive index of the cell medium results in a distorted reflection and therefore a distorted image of the reflected laser beam. This can be used for early detection of leaks in the chamber or edges on gridded coverslips.

4.2.2   Evaluation of fixation parameters

Fixation can cause artifacts by unspecific cross-binding of cellular structures. Especially for correlative imaging, the stability of the analysed structures during fixation is of special interest. The focus of this work was the analysis of neuronal mitochondria, so the application of a fixation method that conserves the neuronal and mitochondrial structure was of highest importance. On the other hand, a fast and direct fixation was needed to fix dynamic processes at a given time point without the production of artifacts.

Live cell microscopy of the cells during fixation provides an opportunity to directly evaluate artifacts caused by chemical fixation at the cellular level. Here, two ways of fixing cells were compared with regard to the preservation of the mitochondrial structure: replacement of the medium with fixative using a channel system and a rapid addition of fixative to the medium as used in the new system (Figure 26 A). In this experiment, Cox8a SNAP cells stained with SiR were fixed either in an ibidi channel slide (ibidi, Munich, Bavaria, Germany) or in the new fixation chamber developed in this work. Cells were imaged on a widefield system with 3 sec intervals. The addition of fixative resulted in less shrinkage of mitochondria compared with the exchange of fixative in neurons (Figure 26 B).

The temperature of the fixative also affected the structural changes during fixation. Usually, the fixative is prepared in advance to avoid disturbances during image acquisition. This also results in the fixative being brought to 37 °C and maintained at this temperature during imaging. However, the prolonged incubation at 37 °C leads to decomposition of the FA and thus to insufficient fixation of the sample and the introduction of structural artifacts.

Fixation generally resulted in a large decrease in fluorescence of the expressed fluorescent proteins during imaging (Supplementary Figure 2). Some FPs, such as the SypHer3s and GCaMP6s sensors used in this work, lose their fluorescence completely and irreversibly. This proved beneficial for subsequent antibody stainings, as the fluorescence channel previously occupied by these proteins was now free for an additional signal.
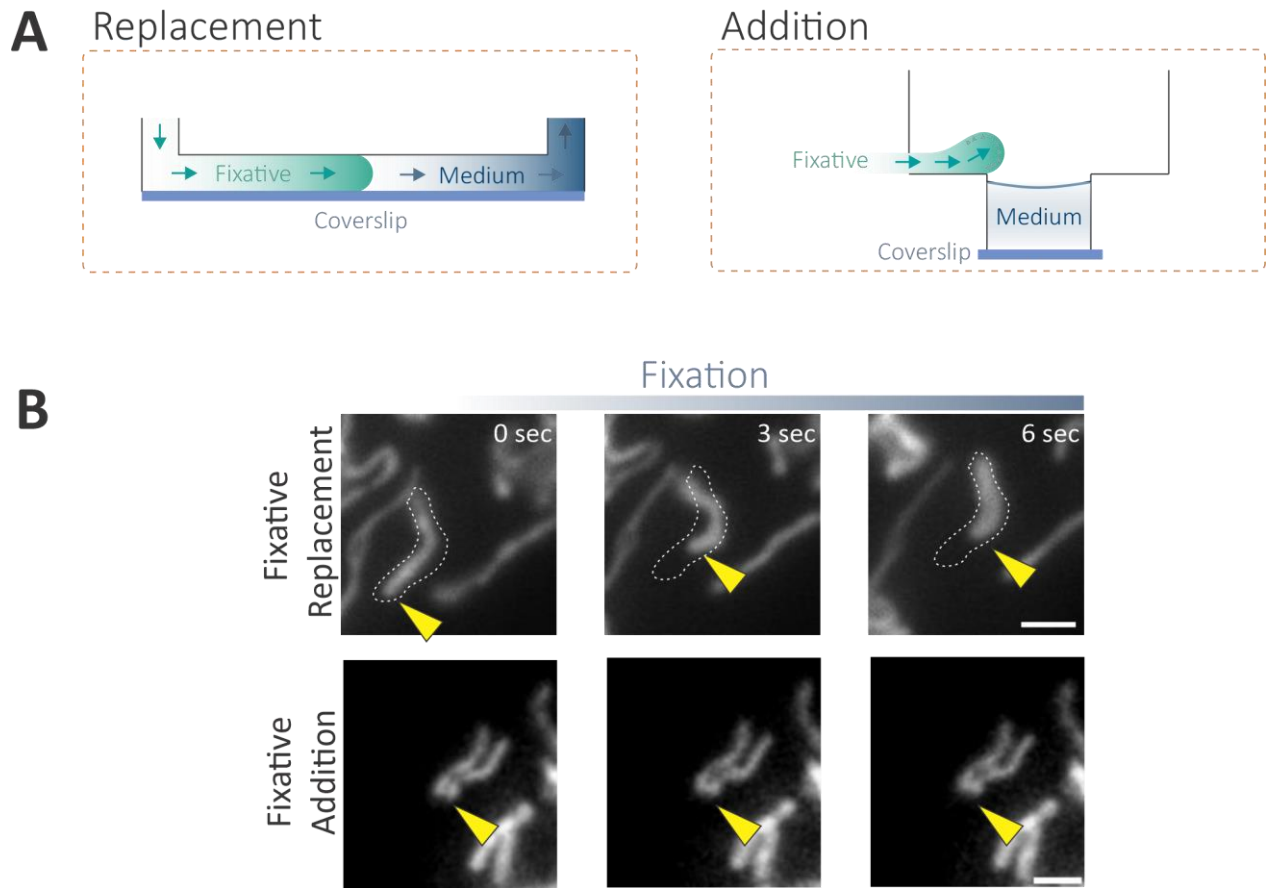
Figure 26: Evaluation of fixative application for on-stage fixation. *Fixation can lead to morphological changes of the cells and its organelles depending on the method the fixative is delivered to the cells. A) Schematic drawings of two possible methods to deliver the fixative to the cells on stage. The left image shows a standard channel system where the fixative slowly replaces the cell culture medium. The right image shows a method (developed in this thesis) where a larger volume of the fixative is build up prior to a sudden release into the cell culture medium. B) Live-cell fluorescence imaging of mitochondria in HeLa cells expressing Cox8a-SNAP labeled with silicon rhodamine during fixation with 4 % FA in PHEM-Buffer. The upper row of images shows the succession of fixation when the fixative replaces the medium. The highlighted mitochondrion shrinks and changes its morphology over time. The lower row of images shows the succession when the fixative is rapidly added to the medium. Here, the changes in structure are minimal, if any at all. Images where corrected for bleaching. Scale bar: 2 µm.*

To evaluate the changes of inner mitochondrial architecture due to fixation, a stable HeLa cell line expressing Cox8a-SNAP was used. With this cell line, it was possible to image cristae in living cells using STED microscopy (Stephan et al., 2019). However, to combine the staining with immunofluorescence is challenging as the crista structure is very sensitive and gets lost during fixation and permeabilization. This is why, different buffer systems and permeabilization reagents were tested, imaged on a STED microscope and evaluated, with a rating from no preservation of crista structure ("-") to good preservation of crista structure ("+++") (Table 6). The Cox8a SNAP staining was performed prior to fixation as described by Stephan et al. (2019) with only the buffer systems or permeabilization reagents exchanged.

Table 6: Evaluation of crista preservation under different conditions

	PBS	Hepes	PHEM
Saponin	+	++	+++
Triton	-	+	+
No permeablication	+	++	++

The best structural preservation of the inner mitochondrial cristae structure was achieved with PHEM buffer and saponin (Table 6, Figure 27 A). In this combination, individual crista are still visible in STED microscopy, in contrast to standard fixation with PBS and Triton, in which the inner mitochondrial architecture is severely altered (Figure 27 B). The preservation of the cristae can be easily compared by evaluating line profiles along the mitochondrial axis for both conditions, where individual cristae are clearly visible only under PHEM conditions (Figure 27 C).

Furthermore, by using FA and GA fixation, saponin permeabilisation and PHEM buffer, Furthermore, by using combined FA and GA fixation, saponin permeabilisation and PHEM buffer, immunofluorescence gets possible while still preserving cristae structure. The full protocol is described in the methods section 3.2.4. DNA in mitochondria was stained with an anti-dsDNA antibody (IG) and a secondary IG coupled to AF594 in HeLa Cox-SNAP cell line. The nucleoids occupied gaps between the otherwise tightly stacked cristae (Figure 27 D). The combination with antibody staining makes this protocol an interesting option for the analysis of crista structure with protein distribution at the endogenous level, taking advantage of the high versatility of antibodies.
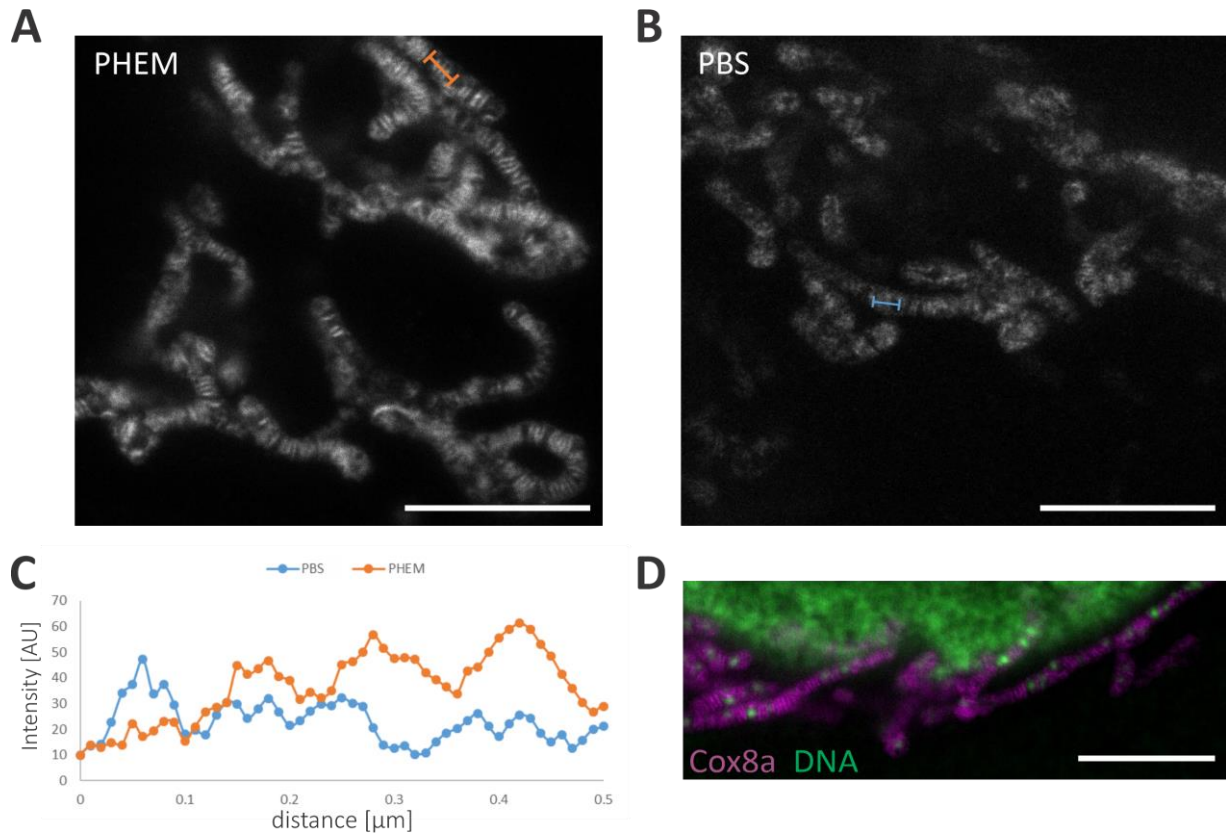
Figure 27: Comparison of fixation quality between PHEM- and PBS-buffered formaldehyde. *A) STED image of mitochondrial cristae that were fixed with 4 % formaldehyde (FA) and 0.2 % glutaraldehyde (GA) in PHEM buffer. The fixation with PHEM-FA-GA shows good structure preservation as individual cristae are still identifiable. B) STED image of mitochondrial cristae that were fixed with 4 % FA and 0.2 % GA in PBS buffer. The structure preservation is worse than with the PHEM-FA-GA fixation. The signal from the Cox8a-SNAP staining is very diffuse and individual cristae are hardly recognizable. C) Intensity profiles over 0.5 µm of the trajectories shown in A) (PHEM buffer fixation, orange) and B) (PBS buffer fixation, blue). D) Two color STED image of a Cox8a-SNAP (magenta) HeLa cell with additional immunostaining against dsDNA (green). Scale bars: 5 µm.*

With the developments shown so far, improved live cell imaging and on-stage fixation with minimal artifacts in mitochondria have been provided. This forms the basis for subsequent correlation of live cell microscopy and immunofluorescence microscopy and ensures that the procedure affects the sample as little as possible to reduce artifacts due to stress responses during imaging or fixation artifacts. To complete the correlation workflow, the region already imaged must now be recovered on the next microscope.

4.2.3 Retrieving the Region Of Interest for correlative microscopy

To increase the information content of a sample, cells observed in live cell microscopy can now be stained with antibodies and observed with a microscope at higher spatial resolution. One of the main issues when transferring a sample from one microscope to another is the difficulty to find the previously identified regions of interest on the new system.
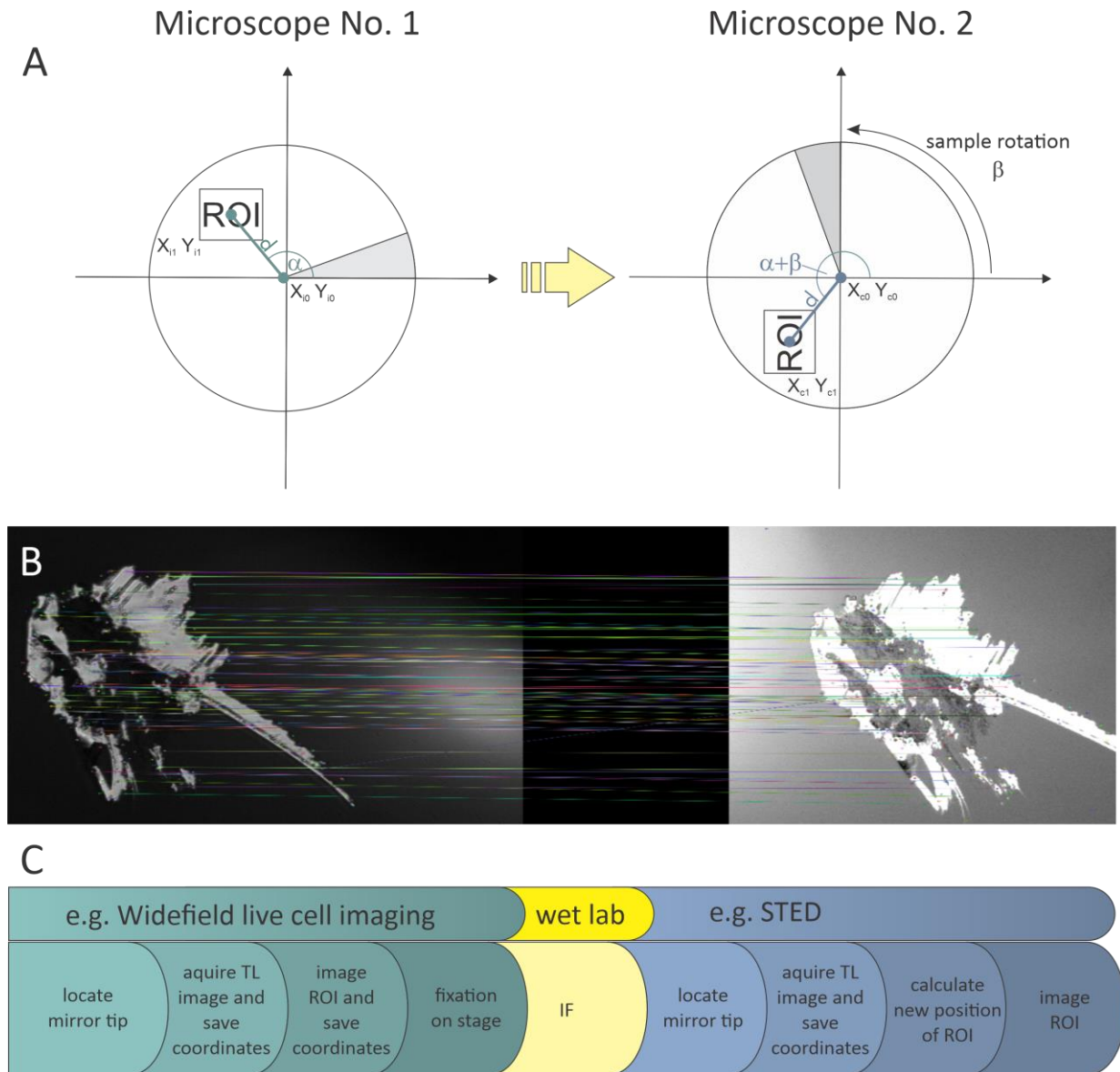
Figure 28: Image registration and retrieval of regions of interest for correlative microscopy. *The transfer of a coverslip from one microscope to another can induce translation and rotation of the previously defined regions of interest (ROI). Registration of individual features on the sample can help in retrieving the predefined regions. A) Illustration of a coverslip with a defined ROI at the coordinates Xi1/Yi1. The position of the ROI from the center point Xi0/Yi0 can be described as a vector with the angle α and the length d. The grey area illustrates an aluminum mirror on the coverslip. When the sample is moved to microscope 2, an additional angle β is introduced by which the sample is turned in relation to the position on microscope 1. The relative position of the ROI towards the center point stays the same. B) Transmission light image of a scratch introduced into the aluminum mirror surface. This scratch is imaged on microscope 1 and then again on microscope 2. Colored lines between the images mark matching features found in both images. Image registration software can calculate the translation and rotation of these features between the two images and depending on that calculate*

the position of the predefined ROI. C) Illustration of the workflow for the correlation of the same sample and the same ROI between two microscopes with an immunofluorescence staining (IF) step in between.

In order to solve this issue of retrieving the regions of interest (ROI), a registration of the ROI in relation to the position of a reference point was made (Figure 28). The problem using only one reference point is rotation of the sample due to handling between the two microscopes. To compensate for that, image registration is used. In the following the complete workflow is described.

For the reference point a small area of the coverslips was sputter-coated with aluminum, creating a small pointed mirror (grey area in the coordinate system of Figure 28 A). Before seeding the cells, a scratch on the mirror is introduced by running the tips of a metal tweezer over the surface to create unique features in the thin aluminum layer (Figure 28 B).

At the microscope used for live cell imaging, the mirror on the coverslip is located, then the initial coordinates are saved as the position of the stage (Xi0,Yi0) and a transmission light (TL) image is taken of the scratch. After this initial registration of the scratch, the cells are imaged and their positions (ROIs) are saved as new coordinate pairs [(Xi1, Yi1); (Xi2, Yi2); … ;(Xin, Yin)]. After the acquisition of live cell image sequences, the sample is fixed on stage in the fixation chamber and dismounted from the sample holder. After immunostaining is performed off stage, the coverslip is mounted on a coverslide for immunofluorescence microscopy (or nanoscopy).

On the new microscopy setup the scratch in the mirror is located, its coordinates (Xc0,Yc0) are saved and a TL image is taken. To compensate for any induced translation and rotation of the sample during handling, a feature detection in Python is done on the TL images of the scratch using the "Scale-Invariant Feature Transform" (SIFT) algorithm (see section 3.3.9). It is able to detect unique features like spikes, grooves or holes of the scratch. The location of the individual features on the first image is then registered onto the second image using the "Fast Library for Approximate Nearest Neighbors" (FLANN) algorithm (see section 3.3.9). The matches between the two images of the same area can be illustrated with colored lines as shown in Figure 28 B. Those matches are used to estimate the affine matrix, which can be decomposed to receive the angle of rotation beta as well as (X,Y) translation and scaling. With this, the new position of the ROI on the new microscopy setup can be calculated. To do so, the angle alpha and the distance d is calculated out of the (Xi0,Yi0) and (Xi1,Yi0) coordinates using *Equation 2* and Equation 3:

Equation 2

$$d = \sqrt{(Xi0 - Xi1)^2 + (Yi0 - Yi1)^2}$$

Equation 3

$$alpha = \tan^{-1}\frac{Yi0 - Yi1}{Xi0 - Xi1}$$

Now the new position of the ROI (Xc1,Yc1) can be calculated using (Xc0,Yc0) as offset point and the corrected angle alpha+beta using Equation 4 and Equation 5:

Equation 4

$$Xc1 = Xc0 + d * \sin(alpha + beta)$$

Equation 5

$$Yc1 = Yc0 + d * \cos(alpha + beta)$$

This provides a fast and easy way to localize the same recorded ROIs on two different setups. However, depending on the properties of microscopes used in the second imaging step some adjustments on the calculations have to be done to adapt to different microscopy stages. For example, the stage coordinates of the two different microscopes may be mirrored and rotated towards each other. Also, depending on the alignment of the system the pixel coordinate system may be rotated to the stage coordinate system. Therefore, a system specific rotation correction factor has to be measured. The Python code for the retrieval of the ROI is appended in the supplementary section (8.2.1). For adaptation of the code, the above-mentioned factors of rotation and orientation of the stage must be changed to the system specifications. This new way of retrieving ROIs allows quick and easy correlation of a variety of different microscopes with minimal setup requirements.

This imaging workflow provides solutions for the three major obstacles when performing correlative live cell imaging: The dedicated on-stage fixation chamber ensures a reliable and structure preserving as well as rapid fixation. Together with the optimized fixation parameters, it provides the foundation for the subsequent immuno-labeling of the sensitive mitochondrial structures in neurons. Finally, retrieving the regions of interest on a second imaging system with respect to a reference point allows combining live cell imaging and immunofluorescence. With this approach, the possible connection between synaptic activity, neuronal mitochondria and the presence of nucleoids was investigated.

4.3 Interplay between neuronal and mitochondrial function to the mtDNA distribution

The developed setup not only allows targeted fixation of live imaged cells at a defined time point for correlative microscopy, but also enables precise tracking of neurons after and during electrical stimulation of neurons due to its high stability and temporal resolution.

The presence of two distinct subpopulations of mitochondria defined by nucleoid content and the accumulation of mitochondria containing nucleoids in the presynapse raises several questions. One of these is whether mitochondria lacking nucleoids exhibit impaired function. To test whether mitochondria with nucleoids are more active than those without, their matrix pH was compared during the stimulation of neuronal activity.

4.3.1 Influence of mtDNA content on mitochondrial function

Mitochondria with nucleoids are enriched in the presynapse, a region with high energy demand as well as the need of Ca^{2+} regulation. This could indicate that mitochondria containing nucleoids are particularly active in energy production and Ca^{2+} buffering compared to nucleoid free mitochondria. A pH gradient between the cytosol and the mitochondrial matrix is fundamental for mitochondrial functions like ATP synthesis but also Ca^{2+} buffering. The gradient is generated via the OXPHOS complexes, whose central components are encoded by mitochondrial DNA. To test this, the matrix pH of mitochondria with and without nucleoids was compared during the stimulation of neurons.

To test if the presence of a nucleoid has an influence on mitochondrial matrix pH, the ratiometric FP SypHer3s was expressed in neurons and targeted to the mitochondrial matrix (Ermakova et al., 2018). SypHer3s is excitable at wavelengths of 405 nm and 488 nm and emits in both cases at 525 nm. The shift in the excitation wavelength is dependent on the protonation state of the chromophore. So, the ratio of the emission intensity, after sequential recording of the intensities excited by 405 nm and 488 nm, is a measure for the pH. A higher ratio of F488 to F405 for example, corresponds to a higher pH of the environment. The forced depolarization of the plasma membrane by electrical stimulation of neurons should result in a higher activity of the neurons and thus a higher demand for energy and ion buffering capabilities. This could translate into changes in the mitochondrial pH. Possible differences in mitochondria with and without nucleoids could indicate different functional capabilities. The focus in this work was on the pH differences between single mitochondria rather than on the exact pH values. Hence, no calibration curve was generated to correlate the ratio to a specific pH-value.

First, neurons expressing mitochondrial targeted SypHer3s were imaged sequentially using 488 and 405 nm excitation every second, subsequently nucleoids were detected using the live cell dye N-arylpyridocyanine (PC3) by pipetting the dye into the imaging chamber on top of the microscope. This was done after the SypHer3s measurements to avoid interference of the anionic dye with the pH of the mitochondrial matrix during the ratiometric measurements.
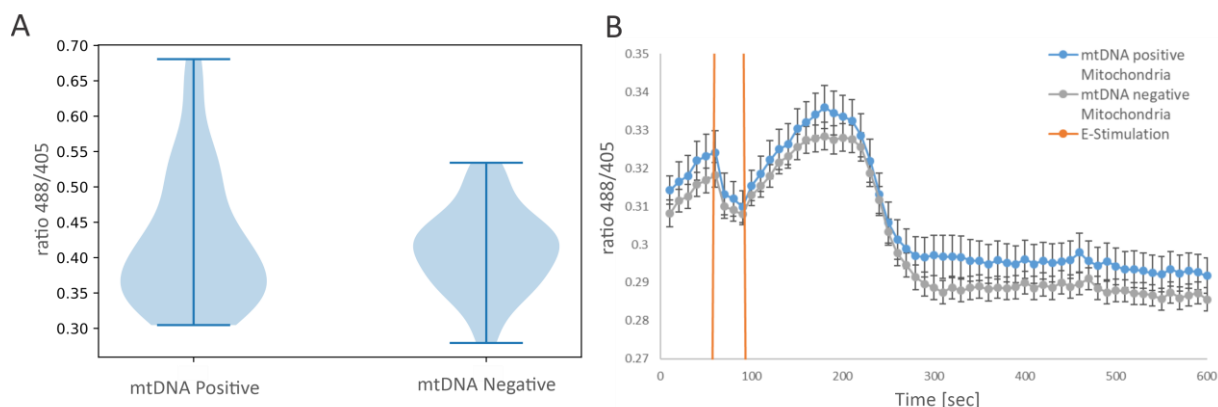
Figure 29: Influence of nucleoid presence on the pH of the mitochondrial matrix. For the evaluation of matrix pH, the mitochondrial pH sensor SypHer3s was expressed in neurons and imaged with 405 and 488 nm excitation. The ratio of the emission at 488nm to the emission at 405nm is plotted. Nucleoids were identified by subsequent staining using PC3. A) F_{488}/F_{405} fluorescence ratio in silenced neurons under 1 µm TTX treatment averaged over 200 time points (0-200 sec). The mean value of nucleoid positive mitochondria at 0.42 is not significantly higher than that of nucleoid negative mitochondria at 0.41 B) Plot of a representative time course of the F_{488}/F_{405} ratio with 1 sec intervals. After 60 sec, a field stimulation is applied with pulses of 20 Hz for 30 s and 10 V per centimeter (orange lines) to stimulate neuronal activity. The F_{488}/F_{405} ratio of mtDNA positive and negative mitochondria drops during stimulation, followed by a rise to the maximum at about 200 sec and a fall to a new baseline at about 300 sec. The F_{488}/F_{405} ratio of mtDNA positive mitochondria (grey) is slightly higher than that of mtDNA negative mitochondria (blue). Both curves follow the same course, indicating similar mitochondrial activity independent of mtDNA content.

To compare the matrix pH measurement of mitochondria with and without nucleoids, neurons were imaged in the presence of 1 µM of the voltage gated sodium channel inhibitor Tetrodotoxin (TTX). This should inhibit spontaneous neuronal activity and the resulting fluctuations in mitochondrial pH over time. Fluctuations in matrix pH triggered by neuronal activity complicate analysis and comparison between different mitochondrial populations. Single static mitochondria were analyzed independent of their subcellular localization in the neuron and averaged over 200 time points (0-200 sec). On average, mitochondria harboring nucleoids (Figure 29 A) have a F_{488}/F_{405} ratio of 0.42 and mitochondria without nucleoids (Figure 29 A) F_{488}/F_{405} ratio of 0.41, suggesting a similar pH in the mitochondrial matrix in the resting state.

Even though the analysis of mitochondrial matrix pH does not show a significant difference of the average, the violin plot shows a different distribution with a part of mitochondria with higher F_{488}/F_{405} ratio in the case of mtDNA positive mitochondria suggesting a subpopulation of mtDNA positive mitochondria with a higher matrix pH . However, in this analysis, no differentiation between presynaptic and non-synaptic mitochondria was made. Labeling of neurons in living cells, e.g. with AAV, is not 100 % efficient. Therefore, using a genetic encoded presynaptic marker, presynaptic mitochondria could be classified as non-synaptic due to the

lack of labeling and the intertwined growth of the neurons. For this reason, no presynaptic marker was used in this live cell experiment.

To compare the changes in matrix pH of mitochondria under active stress conditions, long-term potentiation (LTP) was induced with a field stimulation device at 10 Hz for 30 seconds. Electrical stimulation forces neurons to release neurotransmitters. The high frequency and long duration of the stimulus depletes the SV pool and releases increased neurotransmitters. This leads to an increased demand on the presynaptic mitochondria. High-frequency stimulation eventually leads to synaptic adaptation and an increase in synaptic strength, known as LTP. This can occur in various ways, e.g., through the recruitment of additional neurotransmitter receptors at the postsynapse.

Neurons were imaged every second for a time period of 600 sec. After 60 sec, the LTP was initialized. Start and stop of the LTP is illustrated by the orange lines (Figure 29 B). In the blue curve, the F_{488}/ F_{405} ratio of nucleoid positive mitochondria is plotted and in the grey curve the F_{488}/ F_{405} ratio of mitochondria without nucleoids. Both curves are dropping during the LTP followed by an increase to the local maximum and a decrease to a new baseline, both show the same course. The changes in the mitochondrial matrix pH suggest a fluctuation of the chemical and electrical gradient of the mitochondria in response to the stimulation. Also during this time course, mitochondria containing nucleoids have a slightly higher mitochondrial pH, but the differences are not significant.

In conclusion, the established setup allows for analysis of mitochondrial matrix pH of individual mitochondria with a temporal resolution of 1 second for longer periods of time during and after the stimulation of neurons. However, this experiment did not show a significant difference in mitochondrial matrix pH activity between mitochondria with and those without nucleoids and therefore a significant difference in activity could not be shown. The data suggest a subpopulation of mitochondria with nucleoids with a higher matrix pH. However, no location assignment of mitochondria to the dendrites, axons or presynapses could be made in this experiment. Future experiments with mitochondrial location assignment and using additional sensors for mitochondrial activity must show whether this subpopulation consists of presynaptic mitochondria that are more active under the increased demands in the presynapse.

In addition to the functionality of the two mitochondrial subpopulations, the accumulation of observed selection at the presynapse also raises the question of what controls mitochondrial selection in the presynapse. To address this question, the correlative approach is used to investigate whether the distribution of nucleoids depends on synaptic activity.

4.3.2 Correlation of neuronal activity and nucleoid distribution

To investigate the interplay between neuronal activity and the nucleoid distribution a mitochondrial targeted mScarlet-I and the Ca^{2+} sensor Axon-GCaMP6s, which accumulates in the axon, were expressed in neuronal cells. The mitochondrial mScarlet-I allows the detection of the synaptic mitochondria, while the GCaMP6s intensity is used to identify active axons with an elevated intracellular Ca^{2+} level. Live cell time series were imaged on a widefield microscope with 1-sec intervals for 5 min to observe spontaneous neuronal activity before the fixation.

After fixation on the stage, TFAM as a maker for nucleoids and Bassoon as a marker for the active zone were labelled by immunofluorescence and the sample was subsequently imaged on a confocal microscope. In the following, mitochondria were analysed for their TFAM presence in correlation to the Bassoon signal as well as the signal from live cell Ca^{2+} imaging. The correlation of these fluorescence signals should give information about nucleoid distribution in mitochondria in a functional context.

The analysis showed that 70 % of all mitochondria present in an active presynapse were TFAM-positive. This local accumulation of mitochondria with nucleoids in active presynapses is higher compared to the 59 % of mitochondria with nucleoids in the average presynapse (disregarding their activity level) and the 36 % of non-synaptic axonal mitochondria (see Figure 19). It is worth mentioning, however, that TFAM staining underestimates the total mtDNA content in the neuronal culture by about 10 %, as shown previously (see Figure 19). This means that the number of mitochondria with a nucleoid in the presynapse could be higher than the 70% reported here.
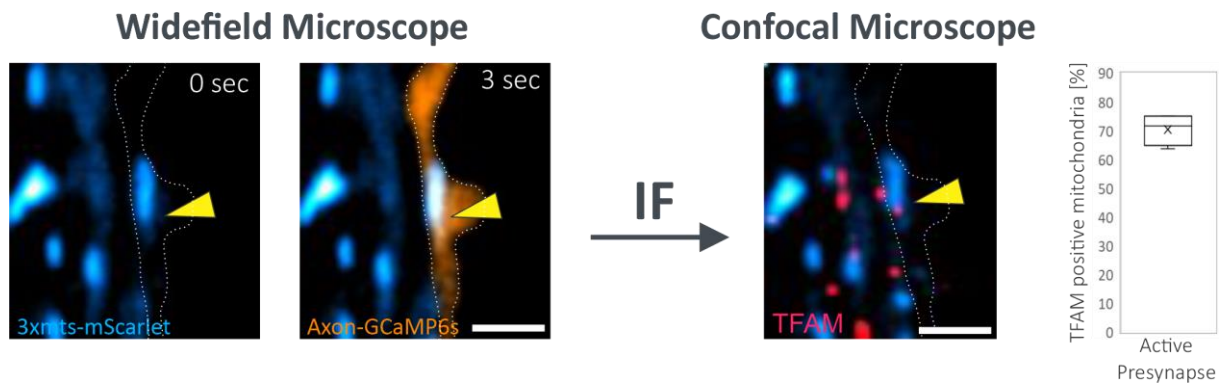
Figure 30: Correlative live and fixed cell microscopy of active presynapses*. Left side) Fluorescence images of neuronal cells expressing mScarlet (blue) targeted to the mitochondrial matrix and the Ca^{2+} sensor GCaMP6s (orange). Shown are two time points taken 3 sec apart on a widefield microscope. The yellow arrow indicates a mitochondrion in a presynaptic bouton. Low intensity GCaMP6s is seen at 0 sec and high intensity at 3 sec, which signals a Ca^{2+} influx into the presynapse. Right side) Fluorescence image after fixation and immunofluorescence staining (IF) against TFAM (red). The correlated image to the right shows the TFAM distribution in the same ROI. The graph shows the percentage of mitochondria with TFAM signal in an active presynapse. For the analysis ~150 presynapses per experiment (n=3) were analyzed. Scale bar: 2 µm.*

This finding led to the idea that mitochondria with a nucleoid are selectively accumulated at active presynaptic sites, due to the locally increased demand for this organelle. To further test this, a biochemical modulation of synaptic activity was performed. In the following section, the impact of this modulation on the accumulation of mitochondria with nucleoids at the presynapse was analyzed.

4.3.3   Functional dependency of mtDNA presence

To investigate if there is a functional selection of mtDNA harboring mitochondria depending on the demands of presynapses, the neuronal activity was blocked with the voltage gated sodium channel inhibitor Tetrodotoxin (TTX). To this end, neurons at DIV7 were incubated with 1 µM TTX in the cell culture medium for 7 days. This long suppression of neuronal activity could have unwanted side effects on the interplay between cells and reduce the number of complete synapses consisting of pre- and postsynapses. To test if TTX treatment impairs synaptogenesis the neuronal connectivity in control and TTX treated cells was analyzed. For this reason, the presynaptic marker Bassoon and the postsynaptic marker Shank2 were detected via immunofluorescence. In a fully connected synapse, the two signals should overlap when examined with a confocal microscope. So the colocalization was determined by calculating the Pearson correlation coefficient between both markers. The results presented in Figure 31 show no significant difference in the correlation coefficient between the untreated control and TTX-treated samples.
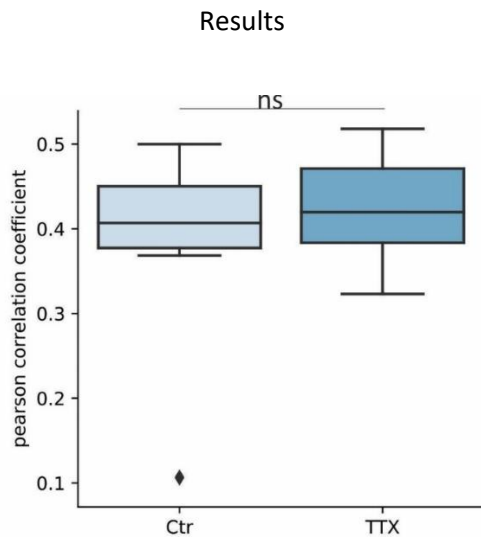
Figure 31: Evaluation of neuronal connectivity upon TTX treatment. *The neuronal connectivity of DIV 14 neurons under control conditions (Ctr) and under TTX treatment were evaluated. As a marker for the proximity of the presynapse and the postsynapse the presynaptic marker Bassoon and the postsynaptic marker Shank were immunolabelled and imaged. Subsequently, the pearson correlation coefficient between both fluorescence signals was calculated. The average Pearson correlation coefficient of the conditions is 0.387 for Ctr and 0.425 TTX, but t-test showed that the difference is not significant (ns, $p>0.05$).*

The fact that there is no difference in neuronal connectivity between control and TTX treatment should rule out further effects of TTX on neurons beyond its mechanism of action to reversibly block sodium ion channels. This enabled the use of Tetrodotoxin for the following experiment.

To test whether synaptic activity affects TFAM distribution, neuronal cells were silenced by TTX treatment. Differences in the presence of mtDNA in mitochondria located in either the presynapse or axon were then examined. TTX treatment of cells was performed as previously described. To assess the reversibility of the potential changes, some of the inhibitor-treated cells were transferred to medium without TTX and incubated for a 24-hour washout period (WO). All samples were double transduced with mitochondrial targeted mScarlet-I and mNeonGreen and immunostained for the nucleoid marker TFAM and the presynapse marker Bassoon. The analysis focused on TFAM presence in presynaptic and non-synaptic mitochondria of the axon and was performed as described before (4.1.3) by using the spectral separation of mitochondria from different cells.
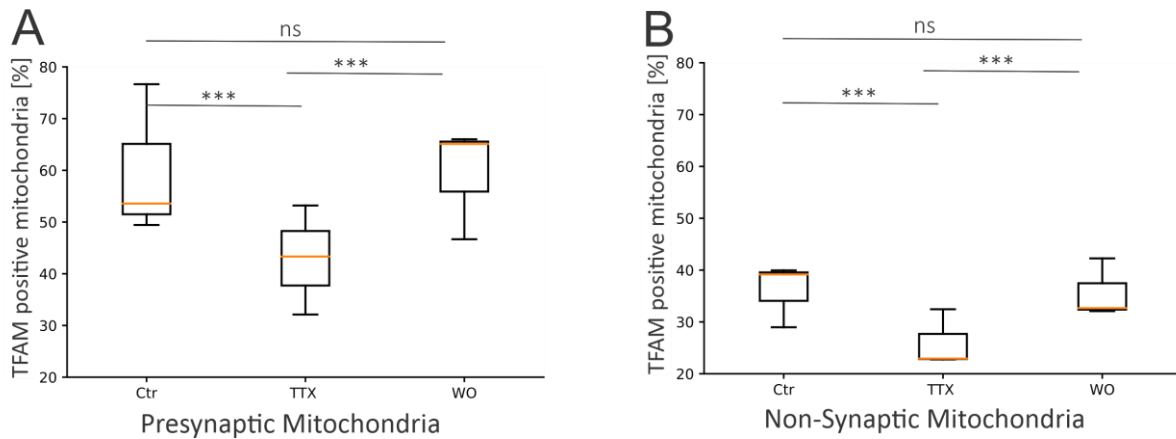
Figure 32: Synaptic activity influences TFAM distribution. *Neurons were treated with 1 µm Tetrodotoxin (TTX) for 7 days to suppress their activity, and both presynaptic as well as non-synaptic mitochondria were examined for the presence of TFAM signals. A) In the control (Ctr) of presynaptic mitochondria, 59 % were TFAM positive, under TTX influence an average of 44 % and after a 24h washout (WO) an average of 61 % of mitochondria were TFAM positive. The percentage of TFAM positive mitochondria in control (Ctr) and after the TTX washout (WO) is significantly higher than during TTX treatment (***, p<0.001). The difference between Ctr and WO is not significant (ns, p>0.05). B) TFAM occurrence in non-synaptic mitochondria under the same conditions as in A). The presence of TFAM in mitochondria showed a mean of 36 % TFAM positive mitochondria under control conditions, 28 % under TTX treatment and 38 % after wash out. Ctr and WO are significantly higher than TTX (***, p<0.001). However, the difference between Ctr and WO is not significant (ns, p>0.05). In comparison, TFAM proportion is significantly higher in presynaptic mitochondria (**, p<0.01) than in non-synaptic axonal mitochondria, regardless of conditions.*

The analysis of mitochondria in the presynapse under the different conditions showed a drop in the amount of TFAM-positive mitochondria in TTX treated neurons down to 44 % compared to the untreated control with an average of 59 % mitochondria containing mtDNA (Figure 32 A). After the 24 h wash out step, 61 % of the presynaptic mitochondria are TFAM positive again. The difference between the untreated control and the wash out is not significant (ns, p>0.05).

To test whether this effect is limited to the presynaptic area, the TFAM content of non-synaptic axonal mitochondria was also analysed (Figure 32 B). As already shown in previous experiments (4.1.6), the percentage of TFAM positive mitochondria was significantly lower in non-synaptic axons (36 %) than in presynaptic mitochondria (54 %) (p<0.01). Like mitochondria in the presynapse, the non-synaptic mitochondria also showed a similar significant drop of TFAM content upon TTX treatment (***, p<0.001). In the control, 36 % of axonal mitochondria contained mtDNA, whereas only 28 % of mitochondria showed a positive TFAM signal after TTX inhibition of presynaptic activity. After TTX wash out, the amount of non-synaptic axonal mitochondria containing mtDNA increased to 38 %, approximately reaching the level without neurotoxin administration.

If the idea of active selection of mitochondria based on local energy demand is true, a general decrease in mtDNA content in mitochondria can be expected after 7 days of TTX treatment, regardless of their subcellular location. Since under these conditions the energy demand of the whole cell is lower due to the inhibited neuronal activity. Nevertheless, it is worth noting that even under TTX treatment, the amount of mitochondria with nucleoids in the presynapse is still higher (44 %) than the amount of non-synaptic axonal mitochondria in the untreated control (36 %). In addition, the changes in the presence of TFAM-positive mitochondria between control and TTX conditions are greater in the presynapse (15 % difference, from 59 % to 44 %) than in non-synaptic mitochondria (8 % difference, from 36 % to 28 %). This suggests that the energy demand and selection of mitochondria with mtDNA is higher in the presynapses than in the rest of the axon and consequently the changes in this substructure are more pronounced. Taken together, the results show that the distribution of nucleoids indeed depends on the demand: Lower neuronal activity leads to fewer mitochondria containing nucleoids, whereas higher neuronal activity (after TTX washing) leads to an accumulation of mtDNA-containing mitochondria. Moreover, this process appears to vary depending on the subcellular location.

The results presented in this thesis show that mitochondria in the axon of neurons can be divided into two subpopulations: Mitochondria with and those without nucleoids. Further investigation showed that during synaptogenesis the proportion of mitochondria with nucleoids in axons is increasing and most presynaptic mitochondria carried a mtDNA molecule. This raised the question of whether there is a functional relationship between mitochondria with nucleoids and presynaptic activity. To address this question, it was first necessary to establish a correlative workflow for live cell imaging. To this end, a novel live cell chamber was developed that allows for gentle live observation and rapid fixation of cells. In combination with a fixation protocol specifically designed for mitochondria, the cells could be chemically fixed without artifacts. An aluminum mirror was used as a reference point, which, together with an image registration algorithm, enables the retrieval of previously determined ROIs on a new microscopy system. With this new correlative live to fixed cell microscopy workflow it was possible to confirm a relationship between neuronal activity and the selection of mitochondria containing nucleoids in the presynapse. This is also confirmed by imaging data from fixed cells whose neuronal activity was biochemically modulated with the neurotoxin TTX. In these treated cells the neuronal activity is blocked and the presynaptic mitochondria were less likely to contain mtDNA than in untreated cells. The restoration of nucleoid density and distribution after TTX wash out hints to an active selection mechanisms that ensures the distribution of mitochondria with nucleoids to the presynaptic sites.

5 Discussion

Many studies focus on the subcellular distribution of mitochondria in neurons as their distribution is important for the maintenance of cell compartments far from the nucleus (Mandal & Drerup, 2019; Sheng, 2017; Sheng & Cai, 2012). To date, little is known about the cellular distribution of mtDNA in neurons. This is of particular interest because mtDNA encodes 13 important proteins involved in oxidative phosphorylation (Wallace, 1994). An open question is how the mtDNA is distributed throughout the cell and whether this distribution plays a role in neuronal function. The focus of this work was therefore to study the distribution of mitochondrial nucleoids in neurons and investigate whether there is a relationship between the presence of mitochondria and synaptic activity. Over the course of the studies, it became apparent that a large proportion of axonal mitochondria do not harbor nucleoids and those that do have a nucleoid are preferentially located in the presynapse. To investigate whether the selective accumulation in the presynapse is driven by synaptic activity, a correlative light microscopy workflow was established to connect the functional information obtained by live cell imaging with the endogenous protein distribution visualized by immunofluorescence imaging. The results obtained with this new method suggest that functional selection of mitochondria harboring a nucleoid is dependent on the specific requirements of the presynapse. For better understanding and readability, the technical developments for the correlative approach are discussed first, followed by the findings on the distribution of mitochondrial nucleoids and their relationship to presynaptic activity.

5.1 Technical developments for correlative microscopy

Correlative microscopy allows to compensate for the drawbacks of different microscopy methods by combining them in a sequential approach (Balint et al., 2013; Tam et al., 2014; Xiang et al., 2018). Even though this work focuses on the combination of live and fixed cell microscopy, the established computational retrieval of the ROI can also be used to correlate different microscopy techniques on fixed cells or for sequential staining and retrieving of the ROI for multiplexing on the same microscope.

Live cell microscopy enables the researcher to observe cellular dynamics using FPs or to perform temporal and local resolved functional readouts using different FP sensors (Ermakova et al., 2018). Due to the spectral properties and the availability of dyes and optical systems in conventional microscopy, there are typically four spectral channels (blue, green, red, far-red) which can be separated in a standard approach resulting in the same number of possible structures to label simultaneously. However, the speed of multichannel imaging can be limited by a sequential acquisition of each channel and it is challenging to tag and express multiple targets without artifacts at the correct expression level for every target in the same cells (Ratz et al., 2015; Snapp, 2009; Zimmermann et al., 2003). Therefore, often only one or two channels can be recorded at a time, which limits the number of structures that can actually be observed simultaneously.

When imaging fixed cells on the other hand, the sample is stable, imaging speed is not an issue and the focus is often set on a better resolution. Furthermore, fixed cells enable the use of antibodies to label specific endogenous proteins. In a conventional approach up to four different targets can be labelled and visualized, but this can be increased using multiplexing approaches (Agasti et al., 2017; Gómez-García et al., 2018)

The correlation of both imaging concepts results in an information dense dataset providing a link between cellular dynamics or functions and the structural information or protein distribution. However, if the observed process in the living cell is too fast and a high frame rate is needed, only a limited amount of positions or cells can be recorded in the same experiment. Nevertheless, this approach gives the unique ability to record the heterogeneous history of single organelles or whole cells and place it in context with the protein distribution.

In this work, the three major challenges to realize correlative microscopy of live cells and immunofluorescence microscopy of fixed cells were addressed. First, the adaptation of a microscopic setup for imaging and fixation on stage, second, the fixation process itself, and third, the recovery of ROIs on a second microscope.

5.1.1 Design of the experimental setup and workflow

5.1.1.1 Microscope

In this work, the conventional widefield microscope Olympus IX73 was used to image living cells. Using a widefield microscope has multiple benefits for the visualization of dynamic processes in living cells. The light dose is relatively low, which decreases bleaching and phototoxicity (Magidson & Khodjakov, 2013). In addition, capturing whole cells with a digital camera is many times faster than a line scanning approach, reducing motion artifacts and allowing faster events to be recorded. The disadvantage of a widefield system can be the blurred image with less contrast in thicker samples, which is due to out-of-focus light (Elliott, 2020).

However, in this work, the focus was on visualizing axonal mitochondria of primary rat hippocampal neurons. As those structures are thin and grow flat on the coverslip, out of focus light is negligible and the relevant structures and their dynamics could be visualized in living cells using a standard widefield microscope.

To further optimize the microscope, it was equipped with a new, more sensitive camera which allowed for a lower excitation light power, reducing the phototoxic effects of high light doses. This reduces the stress on the cell and minimizes the introduction of artifacts from observation prior to fixation. To increase the ability of capturing fast multicolor images, the fluorescence light source was replaced with 16 LEDs of different wavelengths from 365 nm to 770 nm that allowed faster switching between excitation light wavelengths. In addition, for the detection multi-bandpass filter sets were used. This combination allowed the channels to be changed without having to mechanically change the filters. The fast sequential imaging of the channels reduces temporal gaps and thus motion artifacts. However, depending on the experiments

the researcher wishes to perform, these modifications may not be necessary, but they do provide a great deal of flexibility in adjusting the imaging parameters and to the requirements for different fluorophores.

5.1.1.2 On-stage fixation chamber

To enable easy and fast fixation on stage directly after the acquisition of live cell data, a novel fixation chamber was developed in this work. The considerations for the design were to build a cheap, easy to manufacture, reusable, and easy to use device. This design takes a new approach and is therefore compared to the two commonly used approaches, perfusion and channel systems. Perfusion systems are open chambers with an inflow and outflow placed directly in the medium. Channels are closed systems with inflow and outflow.

PEEK (polyetheretherketone) material was chosen for the own fixation chamber. The material price per chamber is less than 15 €. It has strong chemical resistance to solvents, acids and bases. It is very resistant to radiation and can be easily sterilized with UV light. It also has a high mechanical strength, which makes it a perfect material for objects of everyday use. The simple design of the chamber allows it to be built with standard tools that should be present in a well equipped workshop. For compatibility, the width and length of the chamber is set to match a standard glass slide and thus should fit into most microscope stages. In addition, the chamber can be easily washed, sterilized and reused. In contrast, most commercially available channel systems for live cell microscopy are designed as disposable products which makes them less sustainable and more expensive as they have to be bought repeatedly over the course of an experiment.

Another advantage of the new live cell chamber over systems using perfusion or microfluidics lies in the strict separation between the cell culture medium in the chamber and the toxic fixative. In the commercial perfusion and channel slides the direct connection between the inflow and the cavity holding the cells allows for a slow and prematurely contamination of the culture medium with the fixative. This can severely impact the cellular behavior during live cell imaging. In addition, in the perfusion systems the cells further away from the inflow will be fixed later and result in an inhomogeneous fixation process over time. This might have an impact on time critical measurements and the interpretation of data obtained from this experiment if part of the whole cell ensemble is fixed faster or earlier than the rest. When using the channel slides it is also important to prevent the formation of air bubbles in the fluid path as they can lead to increased shear forces and disrupt the delicate neuronal cells.

The newly designed live cell chamber bypasses this issue by physically separating the inflow from the cavity holding the cells and the cell culture medium. Furthermore, the open construction make bubble handling obsolete.

After initialization the fixative is pumped onto a ledge above the cells, building up a droplet over a wide front until it collapses into the cavity containing the medium and the cells (Figure 24 B). This results in the rapid addition of a large volume of fixative to the cavity ensuring a

fast, air bubble free and uniform mixing of the two fluids across all cells. The decoupling of the piping also allows the piping to be easily and quickly changed to the next chamber after the experiment. However, a disadvantage of this new device is the low variation of the exact fixation timing. A slow flowrate of the fixative is required to build up the droplet, and the time point of the drop falling into the medium can vary with each experiment. Typically, a full run of the fixation from initiation to release of the drop took about 15 +/- 5 sec. Thus, if to the second accurate fixation timing accurate to the second is required for an experiment, a closed channel would be a better option. However, in the experiments done during this work the timing was sufficient.

The inflow of the fixative is driven by a pneumatic pump which allows a fine control over the flow rate. The integration of the pump control into the control software of the microscope enables remote control of fixation or an automated fixation triggered by predefined events like an increase of fluorescence in the cells that is detected by automated image analysis. This would be especially helpful for infrequent and random events. Although there is a certain variability in the time needed for the full fixation, the use of an automated pump ensures the reproducibility of the overall fixation process. Fixation can also be performed manually using a syringe. However, manual fixation may result in sample movement if the tubing is not optimally connected introducing large imaging artifacts.

In summary, this low-cost chamber allows easy robust and artifact free fixation on stage when the fixation timing does not need to be set to seconds. The ease and carefree handling of the instrument increases throughput and also allows compatibility with standard culturing and staining protocols.

5.1.1.3 Focus control

To compensate for the mechanical and temperature z-drift caused by the fixation process, the microscope used in this work was equipped with a homemade laser-based focus control. One advantage of a laser-based focus control is that it does not require additional excitation of a marker-fluorophore, as is the case with an intensity-based autofocus. This reduces sample bleaching and phototoxicity and is many times faster. A commercial version of a laser-based focus control was not available for the microscope used in this work. The laser beam that was reflected from the cover glass to give feedback about the position of the microscope stage also had the advantage that the uniformity of the detected spot could be used as an indicator of changes in refractive index. These changes can be cause by medium accumulating under the life cell chamber due to a leaky attachment of the cover glass or air bubbles in the system. This was handy for fast problem detection during imaging in the early developmental phases of the fixation chambers.

This autofocus thus allowed undisturbed observation of the marked structures before, during and after fixation.

5.1.2 Evaluation of fixation parameters,

The chemical fixation for immunofluorescence staining is a crucial point of optimal sample preparation. It has to accomplish a reliable and stable fixation of sensitive cellular structures and avoid the introduction of fixation artifacts or destruction or cloaking of epitopes for antibodies. Possible fixation artifacts are especially visible in super-resolution microscopy and can impair the image analysis (Maunsbach, 1965; Pereira et al., 2019; Wurm et al., 2010). Here, due to the established on-stage fixation system, the cells can be imaged during the fixation process and possible (structural) changes can be observed directly. For instance, the mitochondrial movement stopped in less than a second after addition of 4 % FA to the medium and the fluorescence of mNeonGreen was reduced to 50 % in about 20 sec (SD 2.6). However, studies have shown, that fixation can take more than an hour for cytosolic and membrane proteins on the molecular level (Huebinger et al., 2018; Tanaka et al., 2010)

To evaluate the fixation procedure on a suborganelle level, HeLa cells stably expressing Cox8a-SNAP were chosen. Using this cell line, crista structures in living cells could be visualized using STED microscopy (Stephan et al., 2019), but up to this time point, the preservation and visualization of this structure after fixation was challenging. These delicate structures are notoriously hard to image as standard chemical fixation and permeabilisation does not preserve the membrane structures. As shown in the results (Figure 27 A-B), the PHEM buffer showed the best preservation of the mitochondrial inner membrane and crista structure. For efficient fixation of cristae, the addition of 0.2 % Glutaraldehyde to the 4 % Formaldehyde was beneficial, however this is not compatible with all antibody stainings.

A standard procedure in typical FA fixation is to preheat the fixative to 37 °C to avoid providing a temperature shock to the cells (Wurm et al., 2010). In our hands this increased the likelihood of mitochondria shrinking during fixation especially during long time experiments with fixation after a random occurring event. In this kind of experiment, the FA solution was kept at 37 °C for several hours, thereby reducing the stability of the fixative. Hence, to avoid the fixative to degenerate, in all following experiments of this work it was not preheated but used at 4 °C to RT. A 2019 study shows that cold FA with a similar buffer to the PHEM buffer does not lead to increased formation of actin filament artifacts during fixation. In contrast, when a PBS buffer was used, the fixation temperature made a difference for structure preservation. The colder the fixative, the less preserved were the actin filaments (Pereira et al., 2019). However, fixation quality strongly depends on the structure and cell type to be fixed as well as the antibodies used. Therefore, the conditions have to optimized for the analysed structure and the experiment. Usually, for an antibody staining of inner cellular structures, permeabilization of the cell membrane is required. Typically, detergents are used to remove cellular lipids to allow antibodies to enter the cell and different detergents might have different effects on intracellular membranes (Bhairi & Mohan, 1997; Seeman et al., 1973). Whereas Triton X-100 was shown to disrupt the crista structure, saponin was mild enough to enable antibodies to enter the mitochondrial matrix and IMM space, as shown in chapter 4.2.2, while still preserving the crista structure. Saponin appeared to permeabilize most mitochondria but

some parts of the mitochondrial network seemed not to be penetrated by the antibody upon this treatment (Supplementary Figure 3). The formation of pores due to saponin is cholesterol dependent (de Groot & Müller-Goymann, 2016). Therefore, different membrane compositions of single mitochondria could prevent the antibody staining.

So far, the visualization of specific proteins and the crista architecture was only possible by correlative light and electron microscopy (CLEM), but CLEM experiments often need long and complicated preparations. The sample preparation developed here is much easier. During this work, M`Saad et al. presented another way of visualizing cristae in light microscopy by using a NHS ester to label all primary amines of the proteins and subsequently expanding the structure using a polymer framework (expansion microscopy). Because of the high protein density in the cristae and IMM space, a detailed mitochondrial ultrastructure is visible (M'Saad & Bewersdorf, 2020). This approach does not only highlight the mitochondrial structure, but also shows the whole proteome of the cell giving an overview of many subcellular structures. This can be suboptimal for automated analysis, as selective recognition of individual structures is difficult and can only be achieved by pattern recognition or similar methods, if at all. In addition, the protocol presented in this work requires fewer steps. This fixation protocol provides a rapid way to obtain and label intact cristae. This can help to study protein distributions as a function of crista structure. In this work, the protocol was used to ensure the best possible fixation of mitochondria, i.e., artifact-free and structure-preserving. The effort of developing this protocol was taken because live cell imaging itself but also fixation carries the risk of artifacts. This would be particularly problematic for further use in immunofluorescence in correlative microscopy.

5.1.3   Retrieving the Region Of Interest for correlative microscopy

Up to now, most studies using correlative light microscopy have used a combination of live cell widefield microscopy and the super resolution microscopy technique STORM. This allowed the use of one microscopy setup without the need to transfer the samples to another setup to create correlative data (Balint et al., 2013; Tam et al., 2014). However, if in correlative experiments the microscope setup has to be changed or the sample needs to be relocated for additional preparation steps, for example a subsequent immunofluorescence staining as done during this work, the retrieving of a previously defined region of interest (ROI) is of highest importance. The most common approach to retrieve the ROI is adapted from correlative light and electron microscopy (CLEM). For electron microscopy, cells can be grown on an electron dense gold grid where single cells can be located based on a coordinate system embedded into the grid. This was adapted for light microscopy where a grid with a coordinate system is laser cut into a glass coverslip (Xiang et al., 2018). Unfortunately, those grid coverslips are expensive, are fragile during handling and show altered refraction of light at the grid edges, which leads to distortions in the acquired images and can affect the autofocus. Furthermore, the squares and numbers on the coverslip are only visible while using transmitted light and

are obscured by cells growing on edges or by mounting media with a refractive index close to that of glass.

To ensure a simple orientation and high contrast a method to retrieve the ROI using only one reference point was developed during this work, which can be located with the naked eye. For this purpose, a small pointed area of aluminum is sputter coated on the coverslip. The pointed end of the mirror is used as the reference point. Individual markers are introduced by scratching the surface of the aluminum mirror with a tweezer. The distance between the reference point and the predefined ROIs is fixed, only the rotation in relation to the microscope stage is changed due to the sample movement and handling between the two recordings. The missing angle of rotation can be calculated by using automated image registration and feature detection of two images of the reference point that were recorded on both microscope systems. With this, the predefined ROIs can be easily be located on a different microscopy setup. After setting setup specific parameters for the individual microscopes once, the computational approach is easy and fast to use. If the experimental design allows for multiple positioning, the advantages of this approach are fully realized. Also, the calculation has to be done only once, compared to the use of gridded coverslips, where each ROI has to be found using the edges that are difficult to detect. Furthermore, this approach is compatible with a laser based autofocus and super-resolution microscopy and can be applied on basically any microscope, which is able to record the mirror and to pass through the XY coordinates of the stage. For the computing, the only requirement is the freely available programing language Python. To be independent of the microscope computer equipment, the script was running on the online programming platform Jupyter (www.jupyter.org). Therefore, there is no need to install Python and the required packages on every computer.

In conclusion, the on-stage fixation was optimized towards easy handling and highest compatibility with most workflows for cell culture and immunofluorescence staining. The fixation protocol was optimized to preserve mitochondrial ultrastructure as much as possible. The retrieving of the ROI was streamlined towards a fast and reliable method, which is super-resolution and autofocus friendly. These new and simple methods facilitated the handling and adaptation of the workflow thereby increasing the throughput. The development of the correlative live and fixed cell microscopy approach was a prerequisite for the study of the distribution of mitochondrial nucleoids and their possible influence on neuronal activity, which is discussed below.

5.2 mtDNA distribution in neuronal mitochondria

Examination of mitochondrial DNA distribution in neurons showed that most axonal mitochondria are deficient in mtDNA (Figure 16) and that axonal mitochondria harboring nucleoids preferentially accumulate in presynapses (Figure 19). In the following, the results of nucleoid labeling, discrimination of different cells and analysis are discussed.

5.2.1 Nucleoid visualization in neurons

The results presented in section 4.1.4 show that 90% of dendritic but only 41% of axonal mitochondria contain a nucleoid. It is possible that earlier studies overlooked this fact because of difficulties in detecting the mtDNA with DNA antibodies in primary neurons as explained in chapter 4.1.1 (Kroubouzos et al., 1992). Also studies about mitochondrial replication in axons using BrdU do not show an mtDNA counterstaining (Amiri & Hollenbeck, 2008), which might lead to an underestimation of mtDNA numbers present in neurons. Unfortunately, most chemical DNA dyes like picogreen show high background and cannot be fixed without additional RNAse treatment (Ashley et al., 2005). The live cell dye PC3 used in this work is a non-commercial dye gifted by Kakishi Uno (Uno et al., 2021) but it cannot be fixed as well. The overexpression of fusion-constructs of marker proteins with nucleoid proteins such as TFAM may alter the number of nucleoids (Ikeda et al., 2015). This makes this method unsuitable as a nucleoid marker for this study. In addition, the intertwined structures of neurons make it difficult to distinguish between cells overexpressing a particular protein and cells that do not. For this reason multiple antibodies with a specificity for proteins associated with the mitochondrial DNA were tested for this work. Under all tested antibodies only the antibody against the mitochondrial transcription factor A (TFAM) from abcam (ab131607) showed sufficient specificity and signal to noise ratio. However, a recent study showed that the amount of TFAM decorating the nucleoids varies with the degree of transcriptional and replicative activity of the mtDNA (Brüser et al., 2021). These different TFAM concentrations could lead to a weaker immunostaining signal of some nucleoids and thus an underestimation of the mtDNA present in the mitochondria. Therefore, is was necessary to compare the TFAM staining to a second dsDNA staining to estimate the error of undetected nucleoids due to their high activity and thus lower TFAM decoration.

The analysis of the TFAM-dsDNA co-staining showed that about 10 % of the nucleoids do not have a TFAM signal and therefore can be expected to be active. To test this, active replication was visualized with a two-hour treatment of BrdU and active transcription was visualized with overexpression of TEFM-HA (Figure 13). After the analysis of the fluorescence images the data show that there is only a very low colocalization between the BrdU signal (2 %, indicating replication) and the signal of the TEFM-HA with TFAM (11 %, indicating transcription) respectively. This experiment shows that the majority of nucleoids are also inactive in primary rat hippocampal neurons, as previously shown in epithelial HDFA cells by Brüser et al. (2021). As described in the introduction (1.3) the mtDNA is especially susceptible to mutations during the replication process and an increased nucleoid activity could lead to accumulation of

mutations in the mitochondrial DNA of non-dividing neuronal cells. These findings suggests that a subpopulation of inactive nucleoids that are protected from mutational stress also exists in neuronal mitochondria.

Even though the changes in the staining protocol made it possible to analyze the colocalisation level of dsDNA and TFAM, the quality of the dsDNA antibody staining was of low quality and still showed unspecific background signal. The necessary high pH values for this new staining protocol proved to be incompatible with other antibodies, making co-stainings difficult. For this reason, the continued use of TFAM as a marker during this work was a compromise between a high signal-to-noise ratio for nucleoid detection and the ability to perform co-staining with the other required protein markers on the one hand. While accepting a slight underrepresentation of the total nucleoid number on the other as this does not change the main conclusions of this work.

5.2.2 Analysis of axonal mitochondria

Both, in the whole brain and in culture, neurons grow very densely and form many connections between dendrites and axons, which is why there is much spatial overlap of cellular features. This makes it difficult to manually assign mitochondria to a single cell and even impossible for automated analysis. Typically, axon-specific markers, such as Neurofilament visualization as used and shown in Figure 17, are used to identify individual axons and distinguish between different neurons. Additionally, the scaffolding protein of the active zone, Bassoon, is detected as a standard marker for presynaptic sites, which are also located in the axon. When stained together with a mitochondria-specific signal, these two markers should appear in close proximity to each other and help assign individual mitochondria to individual cells. Unfortunately, this is not without problems. In particular, Neurofilament detection is unreliable because it often marks only fractions of axons in the recorded image. Rather than relying on markers for the axon as an indication of whether or not a mitochondrion is located in the investigated cell, the adaptation of the "Brainbow" concept as described in the results (4.1.3, Figure 15, Figure 16) was the solution (Livet et al., 2007; Weissman et al., 2011). In this method, the mitochondria themselves provide information about their association to a particular cell. The neurons are co-transfected with two constructs resulting in the simultaneous expression of two mitochondrial targeted fluorescent proteins, whose individual ratio to each other varies in each cell. This means that all mitochondria with the same ratio belong to the same cell, so that overlapping dendritic and axonal mitochondria can be efficiently assigned to individual cells according to their color of fluorescence. Adapting the "Brainbow" concept for this work also allowed the development of a simpler automated image analysis, as the complex steps of structure recognition and colocalization analysis to assign mitochondria to different origins are no longer required.

In the context of this work, this strategy proved to be advantageous over the usual approach, as it allows better separation of mitochondria from different cells in close proximity to each other.

5.2.3   Subpopulation of mitochondria

The finding that the majority of mitochondria in an axon does not carry mtDNA indicates the existence of two subpopulations of mitochondria in neurons defined by their nucleoid content. This is surprising giving the importance of mitochondrial encoded proteins for mitochondrial function and the expected high demands in the axon and especially in the presynapse (Pulido & Ryan, 2021; Sheng, 2017). Thus, these two subpopulations of mitochondria must maintain their functionality in distant parts of the neuron. Below, a possible explanation for the emergence of the two mitochondrial populations and how slow protein turnover might maintain these populations is discussed.

5.2.3.1   mtDNA distribution is independent of fission in axons
Mitochondria are organized as a dynamic network that undergoes continuous fission and fusion events and spreads throughout the cell body (Lackner, 2014). The balance between fission and fusion regulates the length of individual mitochondria. In general, more fission leads to a higher number of smaller mitochondria, more fusion results in longer mitochondria (Lewis et al., 2018). As illustrated in Figure 4 axonal mitochondria were found to be smaller on average than dendritic ones.

This implies a mechanism that either selects small mitochondria or controls the fission of larger mitochondrial tubules into shorter sections prior to their transport into the axon. With a high number of small mitochondria in the axon a higher fission than fusion rate is expected, but it is unclear how the mtDNA distribution is regulated during this process. Lewis et al. postulate that in U2OS epithelial cells, ER contact sites mediate mitochondrial fission, contributing to mtDNA replication and an even separation of daughter mtDNA at the cleavage site. This ensures that nucleoids are evenly distributed throughout the network (Lewis et al., 2016). If this mechanism was the same in neuronal cells, one would expect the mtDNA to be evenly distributed during fission, i.e. each mitochondrion emerging from a cleavage site would receive one nucleoid. This would result in an increased number of nucleoids per mitochondrial area in the axon.

In contrast, random fission without additional mtDNA replication would result in a higher number of individual mitochondria, while the overall number of nucleoids per cell stays the same. This is confirmed by the data presented in this work, which show no significant difference in the number of nucleoids per overall mitochondrial area between the long dendritic and small axonal mitochondria (Figure 16). Specifically, this could means that longer mitochondria undergo fission at axon entry independent of mtDNA content, and their mtDNA load is consequently randomly distributed among the newly formed smaller mitochondria. Analysing the nucleoid distribution depending on mitochondrial size as shown in Figure 20 B

is further evidence that the distribution of mtDNA in neurons is not regulated by fission and fusion events. This is because when a long mitochondrion with one or more nucleoids is randomly divided into multiple mitochondria of different lengths, the longer of the resulting mitochondria are statistically more likely to have one or more nucleoid, while smaller mitochondria are less likely. This is also reflected in the data (e.g. an axonal mitochondrion with one nucleoid is on average >1 μm^2 and a mitochondrion harbouring 9 nucleoids is on average between 4-6 μm^2, Figure 20 B).

Random mitochondrial fission without a regulated distribution of mtDNA at axonal entry would have several advantages: it saves resources by not upregulating mtDNA replication, which would be necessary to load each mitochondrion with a nucleoid. This would also prevent the introduction of aberrations due to increased mutation rates during replication in the mtDNA.

5.2.3.2 Protein turnover and distribution

The proteins encoded in the mitochondrial genome are essential for mitochondrial function due to their role in OXPHOS complexes (Larsson et al., 1998; Lee et al., 2008). If these proteins were not evenly distributed among the mitochondria, this would lead to impairment of individual mitochondria over time. This is why the finding that the majority of axonal mitochondria are deficient in mtDNA is surprising. It raises the question how mitochondria with and without nucleoids distribute the proteins encoded by the mtDNA to ensure sufficient functionality in a potentially energy-intensive environment. A simple answer would be that protein distribution is managed by the constant exchange of newly synthesized proteins via fission and fusion of the mitochondria inside the axon. Cagalinec et al. show that fission and fusion of neuronal mitochondria is strongly modulated by the mitochondrial mobility and length (Cagalinec et al., 2013). They report that longer mitochondria are more prone to fission and mobile mitochondria are more likely to fuse with others. In this sense a sufficient distribution of mtDNA encoded proteins to nucleoid free mitochondria would require a high mitochondrial mobility, but especially in older specimen, the mitochondrial mobility is decreasing (Milde et al., 2015).

The rate of fission and fusion required to supply all mitochondria with the necessary proteins also depends on the turnover of these proteins. According to SILAC experiments in neuronal cultures, the half-life of mitochondrial proteins is significantly longer than that of other proteins, which is surprising given the expected high ROS exposure in these organelles. The mtDNA-encoded proteins ND1 and ND5 for example showed a half-life of 10.23 and 9.73 days, while these proteins in a glia enriched culture showed a half-life of 3.75 and 4.81 days (Dörrbaum et al., 2018).

The mixing of mitochondria with and without nucleoids and ultimately their proteins by fission and fusion, as well as the longer lifespan of mitochondrial proteins in neurons, may contribute to the stability of the two mitochondrial subpopulations presented here.

5.2.4 Influence of mtDNA content on mitochondrial function

To test if mitochondria with or without mtDNA are functionally different, the relative matrix pH-value as a marker for mitochondrial activity was studied under different conditions using the genetically encoded ratiometric fluorescent probe SypHer3s. The two main functions of mitochondria in synapses are ATP synthesis and Ca^{2+} buffering (Lewis et al., 2018; Rangaraju et al., 2014). Both processes are depending on an electro-chemical gradient between matrix and IMM space. ATP synthesis is dependent on the electrical membrane potential and the pH gradient, whereas ion transport is mainly driven by the pH gradient (Poburko et al., 2011). Therefore, matrix pH differences were chosen as a marker for mitochondrial activity. A functional impairment of mitochondria without nucleoids could support the idea of selection at the presynapse by mitophagy. This idea is based on studies showing that damaged mitochondria are removed by autophagy. However, these studies assume rather extreme cases in which mitochondria are depolarized with drugs or high ROS stress is induced by specific FPs (Ashrafi et al., 2014; Ashrafi & Schwarz, 2015; Van Laar et al., 2011). On the other hand, how basal mitophagy is regulated for maintenance under physiological conditions in neurons has not been fully elucidated. (Grenier et al., 2013; Martinez-Vicente, 2017).

The baseline under neuronal inactive conditions showed a tendency of a higher pH in mitochondria with nucleoids compared to those without mtDNA. After the induction of action potentials by triggering the neuron with a series of electrical pulses, the mean ratio of the fluorescent probe increases for roughly 1.5 min which might indicate a higher energy demand due to neuronal processes reconstituting the cell potential and the uptake and loading of the synaptic vesicle pool as wells as recovery of the Ca^{2+} homeostasis. Apart from that, mitochondria with and without nucleoids show the same behavior.

In both cases the differences showed to be not significant, but the violin plot in Figure 29 A indicates a different distribution of pH-values between mitochondria with and without nucleoids. Because of the fast experimental procedure a pure live cell based experiment was conducted. For analysis, small immobile mitochondria were chosen without considering the exact positioning of the mitochondria in the cell. Therefore, the different distribution could account for a subpopulation located in the presynapse. It was reported that synaptic mitochondria show a higher matrix pH (Ermakova et al., 2018). This is in line with the increased accumulation of mitochondria with nucleoids in the presynapse found here. As well as with the different distribution found in the violin plot for the nucleoid positive mitochondria. However, the small number of mitochondria located in the presynapse compared to the axonal ones would not influence the average significantly in an analysis were no differentiation between the locations is done. For that reason, the mitochondrial matrix pH should be evaluated taking the subcellular localization of the mitochondria into account using the correlative light microscopy workflow developed in this thesis. Furthermore, using also different fluorescent sensors to detect ATP and Ca^{2+} in the mitochondrial matrix could deliver a more direct link on the functionality of the mitochondria.

5.3　Impact of neuronal activity on mtDNA distribution

The data presented in this work showed a clear preference for mitochondria with nucleoids in presynapses emphasizing the importance of a direct supply of mitochondrial encoded proteins in the presynaptic mitochondria. One hypothesis would be that this selection is driven by the increased demands on the mitochondrion by the presynaptic environment. However, the location alone does not clearly show this. To investigate the dependency of distribution due to synaptic activity in a heterogeneous system under physiological conditions a combination of live-cell and immunofluorescence microscopy is needed. To that reason, the new correlative microscopy workflow was designed (4.2). Only the development of a new on-stage fixation chamber and the adaptation of fixation parameters and the microscope setup allows the combination of information on neuronal activity obtained by live cell microscopy with structural information on mitochondria obtained by immunofluorescence microscopy on the same sample. The method was used to investigate the possible relationship between synaptic activity and mitochondrial nucleoid distribution.

5.3.1　Neuronal activity influences mitochondrial selection

A question arising from the experiments presented so far is whether neuronal activity affects the distribution of nucleoids. A common approach to visualize synaptic activity for fixed cell microscopy is by using antibodies against proteins in the luminal domain of a synaptic vesicle, like synaptotagmin for example (Afuwape et al., 2017; Sara et al., 2005). For this purpose, the antibodies are added to the culturing medium and upon exocytosis of the synaptic vesicles (SV) the luminal side is being exposed at the plasma membrane were the antibody can bind its specific epitope. Because after exocytosis the proteins diffuse on the plasma membrane, the resulting fluorescence signal after immunostaining shows a high plasma membrane background. Furthermore, the binding of the antibody could be sterically affecting the vesicle recycling. This might limit the sensitivity of the assay. Another method of visualizing synaptic activity is the use of styryle dyes (Lazarenko et al., 2018). Those dyes are also applied to the cell culture medium where they bind unspecific to the entire plasma membrane. Upon vesicle recycling, the dye is taken up with the SV. After a washout of the excess dye only the labeled intracellular SVs remain fluorescent and can be imaged. However, those dyes can exhibit a high background. In addition, extensive washing can lead to disruption of the mitochondrial network in neurons, as they are very sensitive to changes in the medium.

As a consequence, the axonal targeted Ca^{2+} sensor GCaMP6s as a synaptic activity marker together with the mitochondrial matrix-targeted mScarlet-I as marker for mitochondria was used in this study. The advantage of the Ca^{2+} sensor is that synaptic activity can be immediately monitored live during image acquisition and no extensive wash steps are required that stress the cells additionally. It also provides a high temporal resolution offering additional information about frequency and intensity of single synaptic events. Furthermore, the fact that the Ca^{2+} sensor cannot be fixed frees up a detection channel and allows multiplexing.

The data obtained during the live cell measurement to identify active synaptic sites was combined with subsequent immunofluorescence staining against the protein TFAM associated with the mtDNA. Analysis showed that around 70 % of mitochondria present at the active presynaptic site were TFAM positive (Figure 30). The percentage of 59 % mitochondria with nucleoids at the presynaptic site (Figure 19) might be contradictory to the aforementioned 70 % mtDNA-harbouring mitochondria in active synapses. This discrepancy can be explained by the fact that here, only synapses that were active at the time of live imaging were investigated. Whereas in the previous experiment, all synaptic mitochondria were analyzed, including mitochondria in inactive or less active synapses. The proportion of 70 % mitochondria with nucleoids in the active synapse might be biased by nucleoids involved in replication or transcription, which cannot be visualized by TFAM staining (Figure 13). With the experimental design used here, it cannot be ruled out that there are local differences in nucleoid activity. For example, synapses that have an above average activity and therefore a higher demand for energy could eventually lead to an increased nucleoid activity. This would result in a higher number of obscured nucleoids in the presynapses that are undetectable by TFAM staining. However, up to now, there is no evidence that synaptic activity has an influence on nucleoid activity. This can be examined in future experiments using the correlative workflow of live cell imaging developed in this work by correlating presynaptic activity with nucleoid activity as a function of their subcellular location.

The extended protocol for live cell imaging and the fact that only one ROI (about 20-40 synapses) can be analyzed per coverslip due to time constraints of the experiment limits sample throughput. But the extra time to measure high numbers of samples is well spend: Imaging of fixed cells can only provide snapshots of dynamic events that must be interpreted in a temporal context. In contrast, the correlative approach used here provides immediate and objective information about the history of individual cells and their organelles in a single experiment. This eliminates the even more time-consuming serial experiments for imaging individual events and the subjective reconstruction of the processes that occur between the individual measurements.

The results of this experiment suggest that mitochondria carrying a nucleoid preferentially accumulate at active presynapses. The presence of a nucleoid-positive mitochondrion might have an advantage in providing energy for the locally increased ATP requirements. In addition, the presynapse might benefit from the ability of mitochondria to buffer Ca^{2+} and thus contribute to Ca^{2+} homeostasis. Thus, mitochondria with mtDNA may be functionally more stable compared to those without mtDNA and their presence at the presynapse could contribute to synaptoplasticity by stabilizing active synaptic sites (Lees et al., 2019).

5.3.2   Synaptic silencing reduces selection pressure

The previous experiment showed that active presynapses are predominantly occupied by mitochondria with a nucleoid. To test whether there is a connection between the presence of mtDNA-loaded mitochondria located at the presynaptic site and the activity level of the synapse, all neuronal activity was blocked using Tetrodotoxin (TTX). This neurotoxin selectively and reversibly blocks voltage-activated sodium channels, resulting in inhibition of action potentials, and effectively "silencing" neuronal activity (Moczydlowski, 2013). If synaptic activity has an influence on the distribution of nucleoids in the axon, the reduction of action potentials should be visible in a change of number or distribution of TFAM signals.

After growing the cells in medium spiked with TTX for seven days, the cells were chemically fixed. Presynaptic and postsynaptic sites in the axon were then detected by immunofluorescently labeling the presynaptic active zone protein Bassoon (Frank et al., 2010), which is involved in the SV tethering and Shank2, which is a scaffold protein involved in building the postsynaptic density (Monteiro & Feng, 2017). A colocalization of the fluorescence signals of both proteins during fluorescence microscopy implies the formation of a complete and functional synapse. For this reason, the calculated Pearson correlation coefficient between the two signals can be used as an indicator of overall neuronal connectivity and thus as a marker of the general state of the neuronal cell culture. The analysis of the Pearson correlation coefficient between neurons of a control culture and those of a culture treated with TTX showed no significant difference in their neuronal connectivity (Figure 31). This suggests that the application of Tetrodotoxin to a DIV7 neuronal cell culture for seven days does not interfere with normal cell growth and synaptogenesis. The result also allowed the use of TTX to modulate neuronal activity for the following experiment.

Neurons (DIV7) were transduced with the "brainbow" constructs (Figure 15) and then cultivated for seven days either in normal cell culture medium or in medium spiked with TTX. At DIV14 the cells were chemically fixed and immunostained against TFAM to identify mitochondria carrying a nucleoid. Analysis of control cells grown without the influence of TTX showed that 59 % of presynaptic mitochondria and only 36 % of non-synaptic axonal mitochondria harbored a nucleoid. This is further evidence for the heterogeneous distribution of nucleoids toward a preferred localization in the presynaptic site. In TTX-treated neurons, the proportion of mtDNA-bearing mitochondria decreased significantly to 44 % in presynaptic and to 28% in non-synaptic mitochondria. The decreased presence of mitochondria with nucleoids in the TTX treated cells can be explained with the overall diminished neuronal activity regardless of the subcellular structure (presynapse or axon stem) of the neurons during this time period. The changes of TFAM-content caused by the modulation of neuronal activity affected the mitochondria in the axon as well as in the presynapse. Still, the higher percentage of TFAM positive (nucleoid harboring) mitochondria in the silenced presynapses compared to those in the axon might be explained by the local higher energetic demand for the maintenance of the SV resting pool as well as the maintenance of the membrane potential even under TTX treatment (Pulido & Ryan, 2021). Yet, the changes in the presynapse are more

pronounced (15 % change in the presynapse to 8 % change in the axon) indicating that modulation of neuronal activity has a higher impact on the presynapses than on the rest of the axon. Most strikingly, after wash out of the TTX with fresh cell culture medium, the proportion of mitochondria with a nucleoid in the presynapse as well as in the axon increased approximately to the level of control cells within only 24 h of cultivation (WO, Figure 32). This can be explained with the sudden increase of neuronal activity and the associated higher demand for energy as well as Ca^{2+} buffering capabilities. Again, the change in nucleoid distribution is higher for the presynapse (+ 17 % change) compared to the rest of the axon (+ 10 % change). Normally, site-specific selection events of TFAM-positive mitochondria occur over several days during neuronal development, as shown by the accumulation of TFAM-positive mitochondria in the axon over time (Figure 17, 4.1.5). By intentionally turning neuronal activity off and on, as is done by the TTX treatment and wash out, these selection events might be condensed into a 24-hour window. The rapid increase in the total number of nucleoid-bearing mitochondria within this time frame points to their active selection towards local demanding sites. Preliminary data also suggest that mitochondria in the axonal growth cone, which is also a highly energy-intensive region, are also enriched in TFAM (nucleoids) (Supplementary Figure 4). This supports the idea that the selective force is determined exclusively by local demands on the mitochondria and not by the site itself. This is also the reason why partial selection also occurs in the non-synaptic axonal mitochondria when TTX is washed out. This leads to the hypothesis that selection pressure is positively correlated with mitochondrial requirements. That is, low demands mean low selection pressure, whereas high demands lead to increased selection pressure.

Due to the shortcomings of the TFAM staining the actual numbers of mitochondria with nucleoids might be even higher, as nucleoids involved in replication or transcription can only be insufficiently detected. Given the proven connection between nucleoid content and neuronal activity it would be interesting to focus on active nucleoids under the conditions described here. There might be a higher replication and translation rate of local nucleoids short after TTX wash out, as the supply of fresh mitochondria and mtDNA from the soma could be too slow to ease the demands of the sudden increase of neuronal activity.

Taken together the results from this experiment show that overall nucleoid number and distribution can be influenced by neuronal activity. Also, there are hints that there is a selection process of mitochondria with nucleoids at the presynaptic site, and furthermore, that this selection process is active because it can rapidly answer to changing demands in the neuron.

5.3.3   Potential mitochondrial selection mechanisms

The data shown in this work suggest that the process of active mitochondrial selection is somehow regulated by local demand, which is given, for example, by presynaptic activity. However, the open question is what is the mechanism behind this active selection of mtDNA-bearing mitochondria. The increasing overall density of mitochondria with nucleoids in the axon during synaptogenesis (Figure 17) is arguing against a pure redistribution of mitochondria but rather directing to a relative increase in nucleoids. This could happen in two ways: by increased mtDNA replication or by increased degradation of mitochondria without nucleoids due to the accumulation of functional deficiencies under high workloads. Visualizing the mtDNA replication or lysosomes after TTX wash out could clarify if the accumulation of mtDNA positive mitochondria is due to nucleoid replication and/or mitochondrial degradation.

If mtDNA replication is increased with triggered neuronal activity, it should manifest in a higher signal of newly synthesized mtDNA detectable by BrdU incorporation. This would support the idea of additional DNA synthesis as reason for the accumulation. But, an increased replication rate would also result in a relative increase of mitochondria with more than one nucleoid and maybe an increase of overall mitochondrial area to accommodate the additional nucleoids. Together with an also increased fission rate, this would result in an increase in the number of single mitochondria throughout the axon. These questions should be relatively easy to answer, as all tools and workflows needed were already established. However, an increase in mtDNA replication would not fully explain the higher accumulation of mitochondria containing nucleoids especially in the presynapse.

Selection via degradation on the contrary could be a sufficient explanation, assuming that mitochondria arrive at the presynapse with the same rate independent of nucleoid content and that mitochondria without nucleoids have a higher degradation rate under increased demands as given by the presynapse. An increase in lysosomal markers colocalizing with TFAM-negative mitochondria during and after the 24-hour wash out compared with control conditions may indicate selection by degradation. The higher mitophagy would result in a shift in the mitochondrial population towards mitochondria with nucleoids. This would also increase the probability of a presynaptic site to colocalize with a TFAM-positive mitochondrion. So far the results presented in this work describe the selection process of mitochondria with nucleoids in neurons from DIV0 to DIV14, which is considered to be the neuronal developmental stage or synaptogenesis with a high synaptic plasticity. A 2022 study reports that autophagosomes in the adult brain are actually enriched with mitochondria containing nucleoids (Goldsmith et al., 2022). At first glance, this finding contradicts the idea of mitophagy-mediated selection of mitochondria with nucleoids by degradation of nucleoid-less mitochondria. In the adult brain synaptic plasticity is reduced and stable connections between pre-and postsynapses are established (Waites et al., 2005). These active synapses are depending on a stable supply of energy and robust homeostasis of ions to fulfil their function. In this case mitophagy of damaged mitochondria could serve housekeeping

purposes, as the possible accumulation of mutated nucleoids poses a major threat for the functionality of the synapses and thus to non-dividing neurons as found in the adult brain. Additionally, there seems to be a greater age-dependent mtDNA deletion in synaptic mitochondria compared with non-synaptic mitochondria (Stauch et al., 2014). A possible active selection of mitochondria with nucleoids at the presynaptic site could locally replenish the mitochondria that are discarded and degraded by mitophagy. In the adult brain, this process is likely to be more subtle and part of the background noise of organelle and protein turnover and as such hard to identify.

Two possible mechanisms of action are proposed that could be mediating the selection process, namely increased mtDNA replication and mitophagy. While increased mtDNA replication with all its consequences (more nucleoids, more single mitochondria) cannot be excluded and might be part of the complete process, selection by mitophagy might be the main reason for the accumulation of mitochondria with nucleoids at the presynaptic site. Preferential degradation of mtDNA-less mitochondria could lead to local accumulation of mitochondria bearing a nucleoid, increasing the likelihood of colocalization with a presynapse. These possible mechanisms need to be further investigated in future experiments to elucidate the role of mitophagy and mtDNA replication in the relationship between synaptic activity and mitochondrial mtDNA content.

In summary, the data show that mitochondria in the axon can be subdivided into two populations: those with and those without nucleoids. These subpopulations initially appear to be randomly distributed and then locally selected according to need. In this process, mitochondria with nucleoids are preferred in locations with high demands. In the case of the presynapse, the requirement is not limited to the provision of energy, but is also characterized by calcium buffering. These requirements appear to exert selection pressure on mitochondria resulting in the seen accumulation of mitochondria containing nucleoids in the presynapse.

6 Conclusion and Outlook

In conclusion, the data presented in this thesis show that the mitochondria present in the neuronal axon can be divided into two subpopulations: One with nucleoids and one without. The mitochondria with nucleoids are predominantly found in the vicinity of the presynapse while those without show a more random distribution throughout the axon. The correlative imaging of live cell dynamics and fixed cell protein distributions was able to reveal a link between presynaptic activity and the presence of nucleoids in the local mitochondria. The discovery that there is a local activity driven selection pressure preferring mitochondria containing nucleoids was further supported by biochemical modulation of neuronal activity. The inhibition of neuronal activity by TTX significantly decreased the amount of mitochondria with nucleoids in the presynapse. Ultimately, this resulted in the hypothesis that mitochondria lacking nucleoids might be degraded more rapidly under increased stress by presynaptic activity. This would lead to the observed accumulation of mitochondria with nucleoids in the presynapse. To test whether this assumption is correct, future experiments should focus on mitochondrial degradation (mitophagy) as a possible selection mechanism. One way this could be done includes the analysis of the localization and distribution of lysosomal markers in combination with synaptic and mitochondrial markers. The elevated synaptic activity after TTX washout increases the selection pressure on the mitochondria. If the postulated hypothesis is correct, this should lead to a higher number of mitophagy events that preferentially degrade nucleoid-free mitochondria.

In the present study, the analysis of the matrix pH was not able to discern significant differences in mitochondrial function between mitochondria with or without nucleoids. For this reason, future experiments should focus on mapping mitochondria at the presynapse with labels for pH as well as ATP and calcium concentration and membrane potential. This should give a better overview of possible dysfunction of mitochondria without nucleoids and could help to understand why mitochondria containing nucleoids are preferred at the active presynapse.

The development and design of the novel live cell chamber presented here was a crucial part of this work. Only with this correlative approach it was possible to combine the functional history of synaptic activity with mitochondrial protein distributions and locations in fixed cells. Hence, the method has been optimized to provide an easily adaptable platform that enables an increase in the throughput of correlative light microscopy experiments. The technical developments presented in this work are not limited to the observation of mitochondria in neurons, but can be used for a variety of questions and combinations of different microscopes. They allow a better study of heterogeneous populations under physiological conditions than would be possible using fixed or live cells alone. In addition, a graphical user interface could be added to the code to make image registration and ROI retrieval accessible to a wider user group. In the future, developments could also include full automation of the microscopy process, with fixation automatically triggered by predefined events detected by deep learning algorithms.

7 References

Abbe, E. (1873). Beiträge zur Theorie des Mikroskops und der mikroskopischen Wahrnehmung. *Archiv für mikroskopische Anatomie*, *9*(1), 413-468. https://doi.org/10.1007/BF02956173

Achimovich, A. M., Ai, H., & Gahlmann, A. (2019). Enabling technologies in super-resolution fluorescence microscopy: reporters, labeling, and methods of measurement. *Current Opinion in Structural Biology*, *58*, 224-232. https://doi.org/10.1016/j.sbi.2019.05.001

Adams, K. L., & Palmer, J. D. (2003). Evolution of mitochondrial gene content: gene loss and transfer to the nucleus. *Molecular Phylogenetics and Evolution*, *29*(3), 380-395. https://doi.org/10.1016/S1055-7903(03)00194-5

Afuwape, O. A., Wasser, C. R., Schikorski, T., & Kavalali, E. T. (2017). Synaptic vesicle pool-specific modification of neurotransmitter release by intravesicular free radical generation. *The Journal of physiology*, *595*(4), 1223-1238. https://doi.org/10.1113/JP273115

Agasti, S. S., Wang, Y., Schueder, F., Sukumar, A., Jungmann, R., & Yin, P. (2017). DNA-barcoded labeling probes for highly multiplexed Exchange-PAINT imaging. *Chemical Science*, *8*(4), 3080-3091. https://doi.org/10.1039/C6SC05420J

Altmann, R. (1894). *Die Elementarorganismen und ihre Beziehungen zu den Zellen*. Verlag von Veit & Comp.

Amiri, M., & Hollenbeck, P. J. (2008). Mitochondrial biogenesis in the axons of vertebrate peripheral neurons. *Developmental Neurobiology*, *68*(11), 1348-1361. https://doi.org/10.1002/dneu.20668

Aschrafi, A., Natera-Naranjo, O., Gioio, A. E., & Kaplan, B. B. (2010). Regulation of axonal trafficking of cytochrome c oxidase IV mRNA. *Molecular and Cellular Neuroscience*, *43*(4), 422-430. https://doi.org/10.1016/j.mcn.2010.01.009

Ashley, N., Harris, D., & Poulton, J. (2005). Detection of mitochondrial DNA depletion in living human cells using PicoGreen staining. *Experimental Cell Research*, *303*(2), 432-446. https://doi.org/10.1016/j.yexcr.2004.10.013

Ashrafi, G., de Juan-Sanz, J., Farrell, R. J., & Ryan, T. A. (2020). Molecular Tuning of the Axonal Mitochondrial Ca(2+) Uniporter Ensures Metabolic Flexibility of Neurotransmission. *Neuron*, *105*(4), 678-687 e675. https://doi.org/10.1016/j.neuron.2019.11.020

Ashrafi, G., & Ryan, T. A. (2017). Glucose metabolism in nerve terminals. *Current Opinion Neurobiology*, *45*, 156-161. https://doi.org/10.1016/j.conb.2017.03.007

Ashrafi, G., Schlehe, J. S., LaVoie, M. J., & Schwarz, T. L. (2014). Mitophagy of damaged mitochondria occurs locally in distal neuronal axons and requires PINK1 and Parkin. *Journal of Cell Biology*, *206*(5), 655-670. https://doi.org/10.1083/jcb.201401070

Ashrafi, G., & Schwarz, T. L. (2015). PINK1-and PARK2-mediated local mitophagy in distal neuronal axons. *Autophagy*, *11*(1), 187-189. https://doi.org/10.1080/15548627.2014.996021

Balaban, R. S., Nemoto, S., & Finkel, T. (2005). Mitochondria, oxidants, and aging. *Cell*, *120*(4), 483-495. https://doi.org/10.1016/j.cell.2005.02.001

References

Balint, S., Verdeny Vilanova, I., Sandoval Alvarez, A., & Lakadamyali, M. (2013). Correlative live-cell and superresolution microscopy reveals cargo transport dynamics at microtubule intersections. *Proceedings of the National Academy of Sciences*, *110*(9), 3375-3380. https://doi.org/10.1073/pnas.1219206110

Balzarotti, F., Eilers, Y., Gwosch, K. C., Gynnå, A. H., Westphal, V., Stefani, F. D., Elf, J., & Hell, S. W. (2017). Nanometer resolution imaging and tracking of fluorescent molecules with minimal photon fluxes. *Science*, *355*(6325), 606-612. https://doi.org/10.1126/science.aak9913

Barazzoni, R., Short, K. R., & Nair, K. S. (2000). Effects of Aging on Mitochondrial DNA Copy Number and Cytochromec Oxidase Gene Expression in Rat Skeletal Muscle, Liver, and Heart*. *Journal of Biological Chemistry*, *275*(5), 3343-3347. https://doi.org/10.1074/jbc.275.5.3343

Bates, M., Jones, S. A., & Zhuang, X. (2013). Stochastic optical reconstruction microscopy (STORM): a method for superresolution fluorescence imaging. *Cold Spring Harbor Protocols*, *2013*(6), pdb. top075143. https://doi.org/10.1101/pdb.top075143

Bean, B. P. (2007). The action potential in mammalian central neurons. *Nature Reviews Neuroscience*, *8*(6), 451-465. https://doi.org/10.1038/nrn2148

Betzig, E., Patterson, G. H., Sougrat, R., Lindwasser, O. W., Olenych, S., Bonifacino, J. S., Davidson, M. W., Lippincott-Schwartz, J., & Hess, H. F. (2006). Imaging intracellular fluorescent proteins at nanometer resolution. *Science*, *313*(5793), 1642-1645. https://doi.org/10.1126/science.1127344

Bhairi, S. M., & Mohan, C. (1997). *Detergents*. Calbiochem-Novabiochem.

Bindels, D. S., Haarbosch, L., van Weeren, L., Postma, M., Wiese, K. E., Mastop, M., Aumonier, S., Gotthard, G., Royant, A., Hink, M. A., & Gadella, T. W., Jr. (2017). mScarlet: a bright monomeric red fluorescent protein for cellular imaging. *Nature Methods*, *14*(1), 53-56. https://doi.org/10.1038/nmeth.4074

Bogenhagen, D. F. (2012). Mitochondrial DNA nucleoid structure. *Biochimica et Biophysica Acta (BBA) - Gene Regulatory Mechanisms*, *1819*(9), 914-920. https://doi.org/10.1016/j.bbagrm.2011.11.005

Bottanelli, F., Kromann, E. B., Allgeyer, E. S., Erdmann, R. S., Wood Baguley, S., Sirinakis, G., Schepartz, A., Baddeley, D., Toomre, D. K., Rothman, J. E., & Bewersdorf, J. (2016). Two-colour live-cell nanoscale imaging of intracellular targets. *Nature Communications*, *7*, 10778. https://doi.org/10.1038/ncomms10778

Bradski, G. (2000). The OpenCV Library. *Journal of Software Tools*. *3*, 120

Brüser, C., Keller-Findeisen, J., & Jakobs, S. (2021). The TFAM-to-mtDNA ratio defines inner-cellular nucleoid populations with distinct activity levels. *Cell Reports*, *37*(8), 110000. https://doi.org/10.1016/j.celrep.2021.110000

Burger, W., & Burge, M. J. (2016). Scale-Invariant Feature Transform (SIFT). In W. Burger & M. J. Burge (Eds.), *Digital Image Processing: An Algorithmic Introduction Using Java* (pp. 609-664). Springer London. https://doi.org/10.1007/978-1-4471-6684-9_25

Cagalinec, M., Safiulina, D., Liiv, M., Liiv, J., Choubey, V., Wareski, P., Veksler, V., & Kaasik, A. (2013). Principles of the mitochondrial fusion and fission cycle in neurons. *Journal of Cell Science*, *126*(Pt 10), 2187-2197. https://doi.org/10.1242/jcs.118844

References

Chagnon, P., Gee, M., Filion, M., Robitaille, Y., Belouchi, M., & Gauvreau, D. (1999). Phylogenetic analysis of the mitochondrial genome indicates significant differences between patients with Alzheimer disease and controls in a French-Canadian founder population. *American Journal of Medical Genetics*, *85*(1), 20-30. https://doi.org/10.1002/(sici)1096-8628(19990702)85:1<20::aid-ajmg6>3.0.co;2-k

Chang, D. D., & Clayton, D. A. (1984). Precise identification of individual promoters for transcription of each strand of human mitochondrial DNA. *Cell*, *36*(3), 635-643. https://doi.org/10.1016/0092-8674(84)90343-X

Chen, T.-W., Wardill, T. J., Sun, Y., Pulver, S. R., Renninger, S. L., Baohan, A., Schreiter, E. R., Kerr, R. A., Orger, M. B., & Jayaraman, V. (2013). Ultrasensitive fluorescent proteins for imaging neuronal activity. *Nature*, *499*(7458), 295-300. https://doi.org/10.1038/nature12354

Chinnery, P. F., & Gomez-Duran, A. (2018). Oldies but Goldies mtDNA Population Variants and Neurodegenerative Diseases. *Frontiers in Neuroscience*, *12*. https://doi.org/10.3389/fnins.2018.00682

Chinnery, P. F., Samuels, D. C., Elson, J., & Turnbull, D. M. (2002). Accumulation of mitochondrial DNA mutations in ageing, cancer, and mitochondrial disease: is there a common mechanism? *The Lancet*, *360*(9342), 1323-1325. https://doi.org/10.1016/s0140-6736(02)11310-9

Citri, A., & Malenka, R. C. (2008). Synaptic Plasticity: Multiple Forms, Functions, and Mechanisms. *Neuropsychopharmacology*, *33*(1), 18-41. https://doi.org/10.1038/sj.npp.1301559

Clay Montier, L. L., Deng, J. J., & Bai, Y. (2009). Number matters: control of mammalian mitochondrial DNA copy number. *Journal of Genetics and Genomics*, *36*(3), 125-131. https://doi.org/10.1016/S1673-8527(08)60099-5

Conchello, J.-A., & Lichtman, J. W. (2005). Optical sectioning microscopy. *Nature Methods*, *2*(12), 920-931. https://doi.org/10.1038/nmeth815

Cong, L., Ran, F. A., Cox, D., Lin, S., Barretto, R., Habib, N., Hsu, P. D., Wu, X., Jiang, W., Marraffini, L. A., & Zhang, F. (2013). Multiplex Genome Engineering Using CRISPR/Cas Systems. *Science*, *339*(6121), 819-823. https://doi.org/ 10.1126/science.1231143

Costa, C. J., & Willis, D. E. (2018). To the end of the line: Axonal mRNA transport and local translation in health and neurodegenerative disease. *Developmental Neurobiology*, *78*(3), 209-220. https://doi.org/10.1002/dneu.22555

Cremer, C. (2011). Lichtmikroskopie unterhalb des Abbe-Limits. Lokalisationsmikroskopie. *Physik in unserer Zeit*, *42*(1), 21-29. https://doi.org/10.1002/piuz.201101251

D'Erchia, A. M., Atlante, A., Gadaleta, G., Pavesi, G., Chiara, M., De Virgilio, C., Manzari, C., Mastropasqua, F., Prazzoli, G. M., Picardi, E., Gissi, C., Horner, D., Reyes, A., Sbisà, E., Tullo, A., & Pesole, G. (2015). Tissue-specific mtDNA abundance from exome data and its correlation with mitochondrial transcription, mass and respiratory activity. *Mitochondrion*, *20*, 13-21. https://doi.org/10.1016/j.mito.2014.10.005

de Boer, P., Hoogenboom, J. P., & Giepmans, B. N. G. (2015). Correlated light and electron microscopy: ultrastructure lights up! *Nature Methods*, *12*(6), 503-513. https://doi.org/10.1038/nmeth.3400

References

de Groot, C., & Müller-Goymann, C. C. (2016). Saponin Interactions with Model Membrane Systems - Langmuir Monolayer Studies, Hemolysis and Formation of ISCOMs. *Planta Medica*, *82*(18), 1496-1512. https://doi.org/10.1055/s-0042-118387

Dean, K. M., & Palmer, A. E. (2014). Advances in fluorescence labeling strategies for dynamic cellular imaging. *Nature Chemical Biology*, *10*(7), 512-523. https://doi.org/10.1038/nchembio.1556

Dolle, C., Flones, I., Nido, G. S., Miletic, H., Osuagwu, N., Kristoffersen, S., Lilleng, P. K., Larsen, J. P., Tysnes, O. B., Haugarvoll, K., Bindoff, L. A., & Tzoulis, C. (2016). Defective mitochondrial DNA homeostasis in the substantia nigra in Parkinson disease. *Nature Communications*, *7*, 13548. https://doi.org/10.1038/ncomms13548

Dörrbaum, A. R., Kochen, L., Langer, J. D., & Schuman, E. M. (2018). Local and global influences on protein turnover in neurons and glia. *Elife*, *7*. https://doi.org/10.7554/eLife.34202

Dunsing, V., Luckner, M., Zühlke, B., Petazzi, R. A., Herrmann, A., & Chiantia, S. (2018). Optimal fluorescent protein tags for quantifying protein oligomerization in living cells. *Scientific Repeports*, *8*(1), 10634. https://doi.org/10.1038/s41598-018-28858-0

Edland, S. D., Silverman, J. M., Peskind, E. R., Tsuang, D., Wijsman, E., & Morris, J. C. (1996). Increased risk of dementia in mothers of Alzheimer's disease cases: evidence for maternal inheritance. *Neurology*, *47*(1), 254-256. https://doi.org/10.1212/wnl.47.1.254

Eichenbaum, H., Otto, T., & Cohen, N. J. (1992). The hippocampus—what does it do? *Behavioral and Neural Biology*, *57*(1), 2-36. https://doi.org/10.1016/0163-1047(92)90724-I

Elliott, A. D. (2020). Confocal Microscopy: Principles and Modern Practices. *Current Protocols Cytometry*, *92*(1), e68. https://doi.org/10.1002/cpcy.68

Elson JL, Samuels DC, Turnbull DM, & PF, C. (2001). Random intracellular drift explains the clonal expansion of mitochondrial DNA mutations with age. *The American Journal of Human Genetics.*, *68(3):802-806*. https://doi.org/10.1086/318801

Ermakova, Y. G., Pak, V. V., Bogdanova, Y. A., Kotlobay, A. A., Yampolsky, I. V., Shokhina, A. G., Panova, A. S., Marygin, R. A., Staroverov, D. B., Bilan, D. S., Sies, H., & Belousov, V. V. (2018). SypHer3s: a genetically encoded fluorescent ratiometric probe with enhanced brightness and an improved dynamic range. *Chemical Communications*, *54*(23), 2898-2901. https://doi.org/10.1039/c7cc08740c

Farge, G., Mehmedovic, M., Baclayon, M., van den Wildenberg, S. M., Roos, W. H., Gustafsson, C. M., Wuite, G. J., & Falkenberg, M. (2014). In vitro-reconstituted nucleoids can block mitochondrial DNA replication and transcription. *Cell Reports*, *8*(1), 66-74. https://doi.org/10.1016/j.celrep.2014.05.046

Fieni, F., Bae Lee, S., Jan, Y. N., & Kirichok, Y. (2012). Activity of the mitochondrial calcium uniporter varies greatly between tissues. *Nature Communications*, *3*(1), 1317. https://doi.org/10.1038/ncomms2325

Filograna, R., Koolmeister, C., Upadhyay, M., Pajak, A., Clemente, P., Wibom, R., Simard, M. L., Wredenberg, A., Freyer, C., Stewart, J. B., & Larsson, N. G. (2019). Modulation of mtDNA copy number ameliorates the pathological consequences of a heteroplasmic mtDNA mutation in the mouse. *Science Advances*, *5*(4), eaav9824. https://doi.org/doi:10.1126/sciadv.aav9824

References

Fisher, R. P., Lisowsky, T., Parisi, M., & Clayton, D. A. (1992). DNA wrapping and bending by a mitochondrial high mobility group-like transcriptional activator protein. *Journal of Biological Chemistry*, *267*(5), 3358-3367. https://doi.org/10.1016/S0021-9258(19)50739-6

Fontana, G. A., & Gahlon, H. L. (2020). Mechanisms of replication and repair in mitochondrial DNA deletion formation. *Nucleic Acids Research*, *48*(20), 11244-11258. https://doi.org/10.1093/nar/gkaa804

Förster, T. (1948). Zwischenmolekulare energiewanderung und fluoreszenz. *Annalen der Physik*, *437*(1-2), 55-75. https://doi.org/10.1002/andp.19484370105

Frank, T., Rutherford, M. A., Strenzke, N., Neef, A., Pangršič, T., Khimich, D., Fejtova, A., Gundelfinger, E. D., Liberman, M. C., Harke, B., Bryan, K. E., Lee, A., Egner, A., Riedel, D., & Moser, T. (2010). Bassoon and the synaptic ribbon organize Ca²+ channels and vesicles to add release sites and promote refilling. *Neuron*, *68*(4), 724-738. https://doi.org/10.1016/j.neuron.2010.10.027

Goldsmith, J., Ordureau, A., Harper, J. W., & Holzbaur, E. L. F. (2022). Brain-derived autophagosome profiling reveals the engulfment of nucleoid-enriched mitochondrial fragments by basal autophagy in neurons. *Neuron*, *110*(6), 967-976.e968. https://doi.org/10.1016/j.neuron.2021.12.029

Goldstein, D. S. (2010). Adrenaline and Noradrenaline. *Encyclopedia of Life Science,* 1-8. https://doi.org/10.1002/9780470015902.a0001401.pub2

Gómez-García, P. A., Garbacik, E. T., Otterstrom, J. J., Garcia-Parajo, M. F., & Lakadamyali, M. (2018). Excitation-multiplexed multicolor superresolution imaging with fm-STORM and fm-DNA-PAINT. *Proceedings of the National Academy of Sciences*, *115*(51), 12991-12996. https://doi.org/ 10.1073/pnas.1804725115

Gray, M. W., Burger, G., & Lang, B. F. (1999). Mitochondrial Evolution. *Science*, *283*(5407), 1476-1481. https://doi.org/ 10.1126/science.283.5407.1476

Grenier, K., McLelland, G.-L., & Fon, E. A. (2013). Parkin-and PINK1-dependent mitophagy in neurons: will the real pathway please stand up? *Frontiers in Neurology*, *4*, 100. https://doi.org/10.3389/fneur.2013.00100

Grotjohann, T., Testa, I., Reuss, M., Brakemann, T., Eggeling, C., Hell, S. W., & Jakobs, S. (2012). rsEGFP2 enables fast RESOLFT nanoscopy of living cells. *Elife*, *1*, e00248. https://doi.org/10.7554/eLife.00248

Guo, B., Zhai, D., Cabezas, E., Welsh, K., Nouraini, S., Satterthwait, A. C., & Reed, J. C. (2003). Humanin peptide suppresses apoptosis by interfering with Bax activation. *Nature*, *423*(6938), 456-461. https://doi.org/10.1038/nature01627

Hajnoczky, G., Robb-Gaspers, L. D., Seitz, M. B., & Thomas, A. P. (1995). Decoding of C osolic Calcium Oscillations in the Mitochondria. *Cell, 82*(3), 415-424. https://doi.org/10.1016/0092-8674(95)90430-1

Han, Y., Zhang, Z., Liu, W., Yao, Y., Xu, Y., Liu, X., Kuang, C., & Hao, X. (2021). A Labeling Strategy for Living Specimens in Long-Term/Super-Resolution Fluorescence Imaging. *Frontiers in Chemistry*, *8* , 601436. https://doi.org/10.3389/fchem.2020.601436

Hara, T., Nakamura, K., Matsui, M., Yamamoto, A., Nakahara, Y., Suzuki-Migishima, R., Yokoyama, M., Mishima, K., Saito, I., Okano, H., & Mizushima, N. (2006). Suppression of

basal autophagy in neural cells causes neurodegenerative disease in mice. *Nature*, *441*(7095), 885-889. https://doi.org/10.1038/nature04724

Harman, D. (1981). The aging process. *Proceedings of the National Academy of Sciences*, *78*(11), 7124-7128. https://doi.org/ 10.1073/pnas.78.11.7124

Harman, D. (2002). Aging: A Theory Based on Free Radical and Radiation Chemistry. *Science of Aging Knowledge Environment*, *2002*(37), cp14-cp14. https://doi.org/ 10.1126/sageke.2002.37.cp14

Harris, C. R., Millman, K. J., van der Walt, S. J., Gommers, R., Virtanen, P., Cournapeau, D., Wieser, E., Taylor, J., Berg, S., Smith, N. J., Kern, R., Picus, M., Hoyer, S., van Kerkwijk, M. H., Brett, M., Haldane, A., Del Rio, J. F., Wiebe, M., Peterson, P., Gerard-Marchant, P., Sheppard, K., Reddy, T., Weckesser, W., Abbasi, H., Gohlke, C., & Oliphant, T. E. (2020). Array programming with NumPy. *Nature*, *585*(7825), 357-362. https://doi.org/10.1038/s41586-020-2649-2

Harris, Julia J., Jolivet, R., & Attwell, D. (2012). Synaptic Energy Use and Supply. *Neuron*, *75*(5), 762-777. https://doi.org/10.1016/j.neuron.2012.08.019

Harris, L. J., Skaletsky, E., & McPherson, A. (1998). Crystallographic structure of an intact IgG1 monoclonal antibody. *Journal of molecular biology*, *275*(5), 861-872. https://doi.org/10.1006/jmbi.1997.1508

Hashimoto, Y., Niikura, T., Tajima, H., Yasukawa, T., Sudo, H., Ito, Y., Kita, Y., Kawasumi, M., Kouyama, K., & Doyu, M. (2001). A rescue factor abolishing neuronal cell death by a wide spectrum of familial Alzheimer's disease genes and Aβ. *Proceedings of the National Academy of Sciences*, *98*(11), 6336-6341. https://doi.org/10.1073/pnas.101133498

Hell, S. W., & Wichmann, J. (1994). Breaking the diffraction resolution limit by stimulated emission: stimulated-emission-depletion fluorescence microscopy. *Optics Letters*, *19*(11), 780-782. https://doi.org/10.1364/OL.19.000780

Hellenkamp, B., Schmid, S., Doroshenko, O., Opanasyuk, O., Kühnemuth, R., Rezaei Adariani, S., Ambrose, B., Aznauryan, M., Barth, A., Birkedal, V., Bowen, M. E., Chen, H., Cordes, T., Eilert, T., Fijen, C., Gebhardt, C., Götz, M., Gouridis, G., Gratton, E., Ha, T., Hao, P., Hanke, C. A., Hartmann, A., Hendrix, J., Hildebrandt, L. L., Hirschfeld, V., Hohlbein, J., Hua, B., Hübner, C. G., Kallis, E., Kapanidis, A. N., Kim, J.-Y., Krainer, G., Lamb, D. C., Lee, N. K., Lemke, E. A., Levesque, B., Levitus, M., McCann, J. J., Naredi-Rainer, N., Nettels, D., Ngo, T., Qiu, R., Robb, N. C., Röcker, C., Sanabria, H., Schlierf, M., Schröder, T., Schuler, B., Seidel, H., Streit, L., Thurn, J., Tinnefeld, P., Tyagi, S., Vandenberk, N., Vera, A. M., Weninger, K. R., Wünsch, B., Yanez-Orozco, I. S., Michaelis, J., Seidel, C. A. M., Craggs, T. D., & Hugel, T. (2018). Precision and accuracy of single-molecule FRET measurements—a multi-laboratory benchmark study. *Nature Methods*, *15*(9), 669-676. https://doi.org/10.1038/s41592-018-0085-0

Henry, B. (1740). IX. An account of Mr. Leeuwenhoek's microscopes. *The Royal Society*, *41503–519*. http://doi.org/10.1098/rstl.1739.0085

Hodgkin, A. L., & Huxley, A. F. (1952). A quantitative description of membrane current and its application to conduction and excitation in nerve. *The Journal of Physiology*, *117*(4), 500-544. https://doi.org/10.1113/jphysiol.1952.sp004764

References

Hofmann, M., Eggeling, C., Jakobs, S., & Hell, S. W. (2005). Breaking the diffraction barrier in fluorescence microscopy at low light intensities by using reversibly photoswitchable proteins. *Proceedings of the National Academy of Sciences*, *102*(49), 17565-17569. https://doi.org/ 10.1073/pnas.0506010102

Huebinger, J., Spindler, J., Holl, K. J., & Koos, B. (2018). Quantification of protein mobility and associated reshuffling of cytoplasm during chemical fixation. *Scientific Reports*, *8*(1), 17756. https://doi.org/10.1038/s41598-018-36112-w

Hunter, J. D. (2007). Matplotlib: A 2D graphics environment. *Computing in Science & Engineering*, *9*(03), 90-95. https://doi.org/10.1109/MCSE.2007.55

Ikeda, M., Ide, T., Fujino, T., Arai, S., Saku, K., Kakino, T., Tyynismaa, H., Yamasaki, T., Yamada, K.-i., Kang, D., Suomalainen, A., & Sunagawa, K. (2015). Overexpression of TFAM or Twinkle Increases mtDNA Copy Number and Facilitates Cardioprotection Associated with Limited Mitochondrial Oxidative Stress. *Public Library of Science One*, *10*(3), e0119687. https://doi.org/10.1371/journal.pone.0119687

Ikonen, M., Liu, B., Hashimoto, Y., Ma, L., Lee, K. W., Niikura, T., Nishimoto, I., & Cohen, P. (2003). Interaction between the Alzheimer's survival peptide humanin and insulin-like growth factor-binding protein 3 regulates cell survival and apoptosis. *Proceedings of the National Academy of Sciences*, *100*(22), 13042-13047. https://doi.org/10.1073/pnas.2135111100

Jakobs, S., Stephan, T., Ilgen, P., & Brüser, C. (2020). Light Microscopy of Mitochondria at the Nanoscale. *Annual Review of Biophysics*, *49*(1), 289-308. https://doi.org/10.1146/annurev-biophys-121219-081550

Jakobs, S., Stoldt, S., & Neumann, D. (2011). Light microscopic analysis of mitochondrial heterogeneity in cell populations and within single cells. *High Resolution Microbial Single Cell Analytics*, 1-19. https://doi.org/10.1007/10_2010_81

Kang, D., Kim, S. H., & Hamasaki, N. (2007). Mitochondrial transcription factor A (TFAM): Roles in maintenance of mtDNA and cellular functions. *Mitochondrion*, *7*(1), 39-44. https://doi.org/10.1016/j.mito.2006.11.017

Keppler, A., Gendreizig, S., Gronemeyer, T., Pick, H., Vogel, H., & Johnsson, K. (2003). A general method for the covalent labeling of fusion proteins with small molecules in vivo. *Nature Biotechnology*, *21*(1), 86-89. https://doi.org/10.1038/nbt765

Khusnutdinova, E., Gilyazova, I., Ruiz-Pesini, E., Derbeneva, O., Khusainova, R., Khidiyatova, I., Magzhanov, R., & Wallace, D. C. (2008). A mitochondrial etiology of neurodegenerative diseases: evidence from Parkinson's disease. *Annals of the New York Academy Sciences*, *1147*, 1-20. https://doi.org/10.1196/annals.1427.001

Kitada, T., Asakawa, S., Hattori, N., Matsumine, H., Yamamura, Y., Minoshima, S., Yokochi, M., Mizuno, Y., & Shimizu, N. (1998). Mutations in the parkin gene cause autosomal recessive juvenile parkinsonism. *Nature*, *392*(6676), 605-608. https://doi.org/10.1038/33416

Korzynska, A., Strojny, W., Hoppe, A., Wertheim, D., & Hoser, P. (2007). Segmentation of microscope images of living cells. *Pattern Analysis and Applications*, *10*(4), 301-319. https://doi.org/10.1007/s10044-007-0069-7

References

Kroubouzos, G., Tosca, A., Konstadoulakis, M. M., & Varelzidis, A. (1992). Poly-L-lysine causes false positive results in ELISA methods detecting anti-dsDNA antibodies. *Journal Immunological Methods*, *148*(1-2), 261-263. https://doi.org/10.1016/0022-1759(92)90180-2

Kukat, C., Wurm, C. A., Spahr, H., Falkenberg, M., Larsson, N. G., & Jakobs, S. (2011). Super-resolution microscopy reveals that mammalian mitochondrial nucleoids have a uniform size and frequently contain a single copy of mtDNA. *Proceedings of the National Academy of Sciences*, *108*(33), 13534-13539. https://doi.org/10.1073/pnas.1109263108

Lackner, L. L. (2014). Shaping the dynamic mitochondrial network. *BMC Biology*, *12*(1), 35. https://doi.org/10.1186/1741-7007-12-35

Laissue, P. P., Alghamdi, R. A., Tomancak, P., Reynaud, E. G., & Shroff, H. (2017). Assessing phototoxicity in live fluorescence imaging. *Nature Methods*, *14*(7), 657-661. https://doi.org/10.1038/nmeth.4344

Larsson, N.-G., Wang, J., Wilhelmsson, H., Oldfors, A., Rustin, P., Lewandoski, M., Barsh, G. S., & Clayton, D. A. (1998). Mitochondrial transcription factor A is necessary for mtDNA maintance and embryogenesis in mice. *Nature Genetics*, *18*(3), 231-236. https://doi.org/10.1038/ng0398-231

Lazarenko, R. M., DelBove, C. E., & Zhang, Q. (2018). Fluorescent Measurement of Synaptic Activity Using FM Dyes in Dissociated Hippocampal Cultured Neurons. *Bio-Protocol*, *8*(2). https://doi.org/10.21769/BioProtoc.2690

Lee, C., Yen, K., & Cohen, P. (2013). Humanin: a harbinger of mitochondrial-derived peptides? *Trends in Endocrinology & Metabolism*, *24*(5), 222-228. https://doi.org/10.1016/j.tem.2013.01.005

Lee, W., Choi, H.-I., Kim, M.-J., & Park, S.-Y. (2008). Depletion of mitochondrial DNA up-regulates the expression of MDR1 gene via an increase in mRNA stability. *Experimental & Molecular Medicine*, *40*(1), 109-117. https://doi.org/10.3858/emm.2008.40.1.109

Lees, R. M., Johnson, J. D., & Ashby, M. C. (2019). Presynaptic Boutons That Contain Mitochondria Are More Stable. *Frontiers Synaptic Neuroscience*, *11*, 37. https://doi.org/10.3389/fnsyn.2019.00037

Lewis, S. C., Uchiyama, L. F., & Nunnari, J. (2016). ER-mitochondria contacts couple mtDNA synthesis with mitochondrial division in human cells. *Science*, *353*(6296), aaf5549. https://doi.org/10.1126/science.aaf5549

Lewis, T. L., Jr., Kwon, S. K., Lee, A., Shaw, R., & Polleux, F. (2018). MFF-dependent mitochondrial fission regulates presynaptic release and axon branching by limiting axonal mitochondria size. *Nature Communications*, *9*(1), 5008. https://doi.org/10.1038/s41467-018-07416-2

Li, C., Tebo, A. G., & Gautier, A. (2017). Fluorogenic labeling strategies for biological imaging. *International Journal of Molecular Sciences*, *18*(7), 1473.

Li, Y., Lim, S., Hoffman, D., Aspenstrom, P., Federoff, H. J., & Rempe, D. A. (2009). HUMMR, a hypoxia- and HIF-1alpha-inducible protein, alters mitochondrial distribution and transport. *Journal of Cell Biology*, *185*(6), 1065-1081. https://doi.org/10.1083/jcb.200811033

References

Lichtman, J. W., & Conchello, J.-A. (2005). Fluorescence microscopy. *Nature Methods*, *2*(12), 910-919. https://doi.org/10.1038/nmeth817

Livet, J., Weissman, T. A., Kang, H., Draft, R. W., Lu, J., Bennis, R. A., Sanes, J. R., & Lichtman, J. W. (2007). Transgenic strategies for combinatorial expression of fluorescent proteins in the nervous system. *Nature*, *450*(7166), 56-62. https://doi.org/10.1038/nature06293

Lukinavičius, G., Reymond, L., D'Este, E., Masharina, A., Göttfert, F., Ta, H., Güther, A., Fournier, M., Rizzo, S., Waldmann, H., Blaukopf, C., Sommer, C., Gerlich, D. W., Arndt, H.-D., Hell, S. W., & Johnsson, K. (2014). Fluorogenic probes for live-cell imaging of the cytoskeleton. *Nature Methods*, *11*(7), 731-733. https://doi.org/10.1038/nmeth.2972

M'Saad, O., & Bewersdorf, J. (2020). Light microscopy of proteins in their ultrastructural context. *Nature Communications*, *11*(1), 3850. https://doi.org/10.1038/s41467-020-17523-8

Magidson, V., & Khodjakov, A. (2013). Circumventing photodamage in live-cell microscopy. *Methods in Cell Biology*, *114*, 545-560. https://doi.org/10.1016/B978-0-12-407761-4.00023-3

Mali, P., Yang, L., Esvelt, K. M., Aach, J., Guell, M., DiCarlo, J. E., Norville, J. E., & Church, G. M. (2013). RNA-Guided Human Genome Engineering via Cas9. *Science*, *339*(6121), 823-826. https://doi.org/ 10.1126/science.1232033

Mandal, A., & Drerup, C. M. (2019). Axonal transport and mitochondrial function in neurons. *Frontiers in Cellular Neuroscience*, *13*, 373. https://doi.org/10.3389/fncel.2019.00373

Martinez-Vicente, M. (2017). Neuronal mitophagy in neurodegenerative diseases. *Frontiers in Molecular Neuroscience*, *10*, 64. https://doi.org/10.3389/fnmol.2017.00064

Masters, B. R. (2010). The development of fluorescence microscopy. *Encyclopedia of Life Sciences*, 1-9. https://doi.org/10.1002/9780470015902.a0022093

Maunsbach, A. B. (1965). The influence of different fixatives and fixation methods on the ultrastructure of rat kidney proximal tubule cells. *Journal of ultrastructure research*, *15*(3-4), 242-282. https://doi.org/10.1016/S0022-5320(66)80110-7

McKinney, W. (2010). Data structures for statistical computing in python. In *Proceedings of the 9th Python in Science Conference* (Vol. 445, No. 1, pp. 51-56).

Milde, S., Adalbert, R., Elaman, M. H., & Coleman, M. P. (2015). Axonal transport declines with age in two distinct phases separated by a period of relative stability. *Neurobiology of Aging*, *36*(2), 971-981. https://doi.org/10.1016/j.neurobiolaging.2014.09.018

Miller, K. E., & Samuels, D. C. (1997). The Axon as a Metabolic Compartment: Protein Degradation, Transport, and Maximum Length of an Axon. *Journal of Theoretical Biology*, *186*(3), 373-379. https://doi.org/10.1006/jtbi.1996.0355

Mink, J. W., Blumenschine, R. J., & Adams, D. B. (1981). Ratio of central nervous system to body metabolism in vertebrates: its constancy and functional basis. *American Journal of Physiology-Regulatory, Integrative and Comparative Physiology*, *241*(3), R203-R212. https://doi.org/10.1152/ajpregu.1981.241.3.R203

Minsky, M. (1988). Memoir on inventing the confocal scanning microscope. *Scanning*, *10*(4), 128-138. https://doi.org/10.1002/sca.4950100403

References

Mironov, S. L. (2006). Spontaneous and evoked neuronal activities regulate movements of single neuronal mitochondria. *Synapse*, *59*(7), 403-411. https://doi.org/10.1002/syn.20256

Moczydlowski, E. G. (2013). The molecular mystique of tetrodotoxin. *Toxicon*, *63*, 165-183. https://doi.org/10.1016/j.toxicon.2012.11.026

Monteiro, P., & Feng, G. (2017). SHANK proteins: roles at the synapse and in autism spectrum disorder. *Nature Reviews Neuroscience*, *18*(3), 147-157. https://doi.org/10.1038/nrn.2016.183

Monzio Compagnoni, G., Di Fonzo, A., Corti, S., Comi, G. P., Bresolin, N., & Masliah, E. (2020). The Role of Mitochondria in Neurodegenerative Diseases: the Lesson from Alzheimer's Disease and Parkinson's Disease. *Molecular Neurobiology*, *57*(7), 2959-2980. https://doi.org/10.1007/s12035-020-01926-1

Moriyama, Y., Maeda, M., & Futai, M. (1992). The role of V-ATPase in neuronal and endocrine systems. *Journal of Experimental Biology*, *172*(1), 171-178. https://doi.org/10.1242/jeb.172.1.171

Morten, K. J., Ashley, N., Wijburg, F., Hadzic, N., Parr, J., Jayawant, S., Adams, S., Bindoff, L., Bakker, H. D., Mieli-Vergani, G., Zeviani, M., & Poulton, J. (2007). Liver mtDNA content increases during development: A comparison of methods and the importance of age- and tissue-specific controls for the diagnosis of mtDNA depletion. *Mitochondrion*, *7*(6), 386-395. https://doi.org/10.1016/j.mito.2007.09.001

Muzio, M. R., & Cascella, M. (2020). Histology, axon. *Histology, Axon. StatPearls Publishing, Treasure Island*.

Nass, M. M. (1966). The circularity of mitochondrial DNA. *Proceedings of the National Academy of Sciences*, *56*(4), 1215-1222. https://doi.org/ 10.1073/pnas.56.4.1215

Parakatselaki, M.-E., & Ladoukakis, E. D. (2021). mtDNA Heteroplasmy: Origin, Detection, Significance, and Evolutionary Consequences. *Life*, *11*(7), 633. https://doi.org/10.3390/life11070633

Pathak, D., Shields, L. Y., Mendelsohn, B. A., Haddad, D., Lin, W., Gerencser, A. A., Kim, H., Brand, M. D., Edwards, R. H., & Nakamura, K. (2015). The Role of Mitochondrially Derived ATP in Synaptic Vesicle Recycling. *Journal of Biological Chemistry*, *290*(37), 22325-22336. https://doi.org/10.1074/jbc.M115.656405

Patron, M., Granatiero, V., Espino, J., Rizzuto, R., & De Stefani, D. (2019). MICU3 is a tissue-specific enhancer of mitochondrial calcium uptake. *Cell Death & Differentiation*, *26*(1), 179-195. https://doi.org/10.1038/s41418-018-0113-8

Pédelacq, J. D., Cabantous, S., Tran, T., Terwilliger, T. C., & Waldo, G. S. (2006). Engineering and characterization of a superfolder green fluorescent protein. *Nature Biotechnology*, *24*(1), 79-88. https://doi.org/10.1038/nbt1172

Pekkurnaz, G., & Wang, X. (2022). Mitochondrial heterogeneity and homeostasis through the lens of a neuron. *Nature Metabolism*. https://doi.org/10.1038/s42255-022-00594-w

Pereira, P. M., Albrecht, D., Culley, S., Jacobs, C., Marsh, M., Mercer, J., & Henriques, R. (2019). Fix Your Membrane Receptor Imaging: Actin Cytoskeleton and CD4 Membrane Organization Disruption by Chemical Fixation. *Frontiers in Immunology*, *10*, 675. https://doi.org/10.3389/fimmu.2019.00675

References

Pinto, M., & Moraes, C. T. (2014). Mitochondrial genome changes and neurodegenerative diseases. *Biochimica et Biophysica Acta (BBA) - Molecular Basis of Disease*, *1842*(8), 1198-1207. https://doi.org/10.1016/j.bbadis.2013.11.012

Pleiner, T., Bates, M., Trakhanov, S., Lee, C.-T., Schliep, J. E., Chug, H., Böhning, M., Stark, H., Urlaub, H., & Görlich, D. (2015). Nanobodies: site-specific labeling for super-resolution imaging, rapid epitope-mapping and native protein complex isolation. *Elife*, *4*, e11349. https://doi.org/10.7554/eLife.11349

Poburko, D., Santo-Domingo, J., & Demaurex, N. (2011). Dynamic regulation of the mitochondrial proton gradient during cytosolic calcium elevations. *Journal of Biological Chemistry*, *286*(13), 11672-11684. https://doi.org/10.1074/jbc.M110.159962

Popov, V., Medvedev, N. I., Davies, H. A., & Stewart, M. G. (2005). Mitochondria form a filamentous reticular network in hippocampal dendrites but are present as discrete bodies in axons: A three-dimensional ultrastructural study. *Journal of Comparative Neurology*, *492*(1), 50-65. https://doi.org/10.1002/cne.20682

Prasher, D. C., Eckenrode, V. K., Ward, W. W., Prendergast, F. G., & Cormier, M. J. (1992). Primary structure of the Aequorea victoria green-fluorescent protein. *Gene*, *111*(2), 229-233. https://doi.org/10.1016/0378-1119(92)90691-H

Pulido, C., & Ryan, T. A. (2021). Synaptic vesicle pools are a major hidden resting metabolic burden of nerve terminals. *Science Advances*, *7*(49), eabi9027. https://doi.org/10.1126/sciadv.abi9027

Pyle, A., Anugrha, H., Kurzawa-Akanbi, M., Yarnall, A., Burn, D., & Hudson, G. (2016). Reduced mitochondrial DNA copy number is a biomarker of Parkinson's disease. *Neurobiology of Aging*, *38*, 216.e217-216.e210. https://doi.org/10.1016/j.neurobiolaging.2015.10.033

Rak, M., Su, C. H., Xu, J. T., Azpiroz, R., Singh, A. M., & Tzagoloff, A. (2016). Regulation of mitochondrial translation of the ATP8/ATP6 mRNA by Smt1p. *Molecular Biology of the Cell*, *27*(6), 919-929. https://doi.org/10.1091/mbc.E15-09-0642

Rangaraju, V., Calloway, N., & Ryan, T. A. (2014). Activity-driven local ATP synthesis is required for synaptic function. *Cell*, *156*(4), 825-835. https://doi.org/10.1016/j.cell.2013.12.042

Rangaraju, V., Lauterbach, M., & Schuman, E. M. (2019). Spatially Stable Mitochondrial Compartments Fuel Local Translation during Plasticity. *Cell*, *176*(1-2), 73-84 e15. https://doi.org/10.1016/j.cell.2018.12.013

Ratz, M., Testa, I., Hell, S. W., & Jakobs, S. (2015). CRISPR/Cas9-mediated endogenous protein tagging for RESOLFT super-resolution microscopy of living human cells. *Scientific Reports*, *5*(1), 1-6. https://doi.org/10.1038/srep09592

Reznik, E., Miller, M. L., Şenbabaoğlu, Y., Riaz, N., Sarungbam, J., Tickoo, S. K., Al-Ahmadie, H. A., Lee, W., Seshan, V. E., Hakimi, A. A., & Sander, C. (2016). Mitochondrial DNA copy number variation across human cancers. *Elife*, *5*. https://doi.org/10.7554/eLife.10769

Rizzoli, S. O. (2014). Synaptic vesicle recycling: steps and principles. *European Molecular Biology Organization Journal*, *33*(8), 788-822. https://doi.org/10.1002/embj.201386357

Rossignol, R., Faustin, B., Rocher, C., Malgat, M., Mazat, J. P., & Letellier, T. (2003). Mitochondrial threshold effects. *Biochemical Journal*, *370*(Pt 3), 751-762. https://doi.org/10.1042/bj20021594

References

Russell, O., & Turnbull, D. (2014). Mitochondrial DNA disease-molecular insights and potential routes to a cure. *Exp Cell Res*, *325*(1), 38-43. https://doi.org/10.1016/j.yexcr.2014.03.012

Rust, M. J., Bates, M., & Zhuang, X. (2006). Sub-diffraction-limit imaging by stochastic optical reconstruction microscopy (STORM). *Nat Methods*, *3*(10), 793-795. https://doi.org/10.1038/nmeth929

Sanderson, M. J., Smith, I., Parker, I., & Bootman, M. D. (2014). Fluorescence microscopy. *Cold Spring Harbor Protocols*, *2014*(10). https://doi.org/10.1101/pdb.top071795

Santo-Domingo, J., & Demaurex, N. (2012). The renaissance of mitochondrial pH. *Journal of General Physiology*, *139*(6), 415-423. https://doi.org/10.1085/jgp.201110767

Sara, Y., Virmani, T., Deák, F., Liu, X., & Kavalali, E. T. (2005). An Isolated Pool of Vesicles Recycles at Rest and Drives Spontaneous Neurotransmission. *Neuron*, *45*(4), 563-573. https://doi.org/10.1016/j.neuron.2004.12.056

Schikorski, T., & Stevens, C. F. (1997). Quantitative ultrastructural analysis of hippocampal excitatory synapses. *Journal of Neuroscience*, *17*(15), 5858-5867. https://doi.org/10.1523/jneurosci.17-15-05858.1997

Seeman, P., Cheng, D., & Iles, G. H. (1973). Structure of membrane holes in osmotic and saponin hemolysis. *Journal of Cell Biology*, *56*(2), 519-527. https://doi.org/10.1083/jcb.56.2.519

Shaner, N. C., Steinbach, P. A., & Tsien, R. Y. (2005). A guide to choosing fluorescent proteins. *Nature Methods*, *2*(12), 905-909. https://doi.org/10.1038/nmeth819

Sheng, Z.-H. (2017). The Interplay of Axonal Energy Homeostasis and Mitochondrial Trafficking and Anchoring. *Trends in Cell Biology*, *27*(6), 403-416. https://doi.org/10.1016/j.tcb.2017.01.005

Sheng, Z.-H., & Cai, Q. (2012). Mitochondrial transport in neurons: impact on synaptic homeostasis and neurodegeneration. *Nature Reviews Neuroscience*, *13*(2), 77-93. https://doi.org/10.1038/nrn3156

Shepherd, G. M. G., & Harris, K. M. (1998). Three-Dimensional Structure and Composition of CA33CA1 Axons in Rat Hippocampal Slices: Implications for Presynaptic Connectivity and Compartmentalization. *The Journal of Neuroscience*. https://doi.org/10.1523/JNEUROSCI.18-20-08300.1998

Skipper, S., & Perktold, J. (2010). Statsmodels: Econometric and statistical modeling with python. Proceedings of the 9th Python in Science Conference,

Snapp, E. L. (2009). Fluorescent proteins: a cell biologist's user guide. *Trends in Cell Biology*, *19*(11), 649-655. https://doi.org/10.1016/j.tcb.2009.08.002

Spillane, M., Ketschek, A., Merianda, T. T., Twiss, J. L., & Gallo, G. (2013). Mitochondria coordinate sites of axon branching through localized intra-axonal protein synthesis. *Cell Reports* , *5*(6), 1564-1575. https://doi.org/10.1016/j.celrep.2013.11.022

Stauch, K. L., Purnell, P. R., & Fox, H. S. (2014). Quantitative Proteomics of Synaptic and Nonsynaptic Mitochondria: Insights for Synaptic Mitochondrial Vulnerability. *Journal of Proteome Research*, *13*(5), 2620-2636. https://doi.org/10.1021/pr500295n

References

Stephan, T., Roesch, A., Riedel, D., & Jakobs, S. (2019). Live-cell STED nanoscopy of mitochondrial cristae. *Scientific Reports*, *9*(1), 12419. https://doi.org/10.1038/s41598-019-48838-2

Stewart, J. B., & Chinnery, P. F. (2015). The dynamics of mitochondrial DNA heteroplasmy: implications for human health and disease. *Nature Reviews Genetics*, *16*(9), 530-542. https://doi.org/10.1038/nrg3966

Suju, D. A., & Jose, H. (2017, 16-18 March 2017). FLANN: Fast approximate nearest neighbour search algorithm for elucidating human-wildlife conflicts in forest areas. *2017 Fourth International Conference on Signal Processing, Communication and Networking (ICSCN)*, https://doi.org/10.1109/ICSCN.2017.8085676

Tam, J., Cordier, G. A., Balint, S., Sandoval Alvarez, A., Borbely, J. S., & Lakadamyali, M. (2014). A microfluidic platform for correlative live-cell and super-resolution microscopy. *Public Library of Science One*, *9*(12), e115512. https://doi.org/10.1371/journal.pone.0115512

Tanaka, K. A. K., Suzuki, K. G. N., Shirai, Y. M., Shibutani, S. T., Miyahara, M. S. H., Tsuboi, H., Yahara, M., Yoshimura, A., Mayor, S., Fujiwara, T. K., & Kusumi, A. (2010). Membrane molecules mobile even after chemical fixation. *Nature Methods*, *7*(11), 865-866. https://doi.org/10.1038/nmeth.f.314

Terai, T., & Nagano, T. (2013). Small-molecule fluorophores and fluorescent probes for bioimaging. *Pflügers Archiv - European Journal of Physiology*, *465*(3), 347-359. https://doi.org/10.1007/s00424-013-1234-z

Torroni, A., Petrozzi, M., D'Urbano, L., Sellitto, D., Zeviani, M., Carrara, F., Carducci, C., Leuzzi, V., Carelli, V., Barboni, P., De Negri, A., & Scozzari, R. (1997). Haplotype and phylogenetic analyses suggest that one European-specific mtDNA background plays a role in the expression of Leber hereditary optic neuropathy by increasing the penetrance of the primary mutations 11778 and 14484. The *American Journal of Human Genetics*, *60*(5), 1107-1121.

Trifunovic, A., Hansson, A., Wredenberg, A., Rovio, A. T., Dufour, E., Khvorostov, I., Spelbrink, J. N., Wibom, R., Jacobs, H. T., & Larsson, N.-G. (2005). Somatic mtDNA mutations cause aging phenotypes without affecting reactive oxygen species production. *Proceedings of the National Academy of Sciences*, *102*(50), 17993-17998. https://doi.org/10.1073/pnas.0508886102

Uno, K., Sugimoto, N., & Sato, Y. (2021). N-aryl pyrido cyanine derivatives are nuclear and organelle DNA markers for two-photon and super-resolution imaging. *Nature Communications*, *12*(1), 2650. https://doi.org/10.1038/s41467-021-23019-w

Vaccaro, V., Devine, M. J., Higgs, N. F., & Kittler, J. T. (2017). Miro1-dependent mitochondrial positioning drives the rescaling of presynaptic Ca2+ signals during homeostatic plasticity. *EMBO Reports*, *18*(2), 231-240. https://doi.org/10.15252/embr.201642710

Van Bruggen, E., Borst, P., Ruttenberg, G., Gruber, M., & Kroon, A. (1966). Circular mitochondrial DNA. *Biochimica et Biophysica Acta (BBA)-Nucleic Acids and Protein Synthesis*, *119*(2), 437-439. https://doi.org/10.1016/0005-2787(66)90210-3

Van Haute, L., Pearce, S. F., Powell, C. A., D'Souza, A. R., Nicholls, T. J., & Minczuk, M. (2015). Mitochondrial transcript maturation and its disorders. *Journal of Inherited Metabolic Disease*, *38*(4), 655-680. https://doi.org/10.1007/s10545-015-9859-z

References

Van Laar, V. S., Arnold, B., Cassady, S. J., Chu, C. T., Burton, E. A., & Berman, S. B. (2011). Bioenergetics of neurons inhibit the translocation response of Parkin following rapid mitochondrial depolarization. *Human Molecular Genetics*, *20*(5), 927-940. https://doi.org/10.1093/hmg/ddq531

Virtanen, P., Gommers, R., Oliphant, T. E., Haberland, M., Reddy, T., Cournapeau, D., Burovski, E., Peterson, P., Weckesser, W., Bright, J., van der Walt, S. J., Brett, M., Wilson, J., Millman, K. J., Mayorov, N., Nelson, A. R. J., Jones, E., Kern, R., Larson, E., Carey, C. J., Polat, I., Feng, Y., Moore, E. W., VanderPlas, J., Laxalde, D., Perktold, J., Cimrman, R., Henriksen, I., Quintero, E. A., Harris, C. R., Archibald, A. M., Ribeiro, A. H., Pedregosa, F., van Mulbregt, P., & SciPy, C. (2020). SciPy 1.0: fundamental algorithms for scientific computing in Python. *Nature Methods*, *17*(3), 261-272. https://doi.org/10.1038/s41592-019-0686-2

Völgyi, K., Gulyássy, P., Háden, K., Kis, V., Badics, K., Kékesi, K. A., Simor, A., Györffy, B., Tóth, E. A., Lubec, G., Juhász, G., & Dobolyi, A. (2015). Synaptic mitochondria: A brain mitochondria cluster with a specific proteome. *Journal of Proteomics*, *120*, 142-157. https://doi.org/10.1016/j.jprot.2015.03.005

Wachsmuth, M., Huebner, A., Li, M., Madea, B., & Stoneking, M. (2016). Age-related and heteroplasmy-related variation in human mtDNA copy number. *Public Library of Science Genetics*, *12*(3), e1005939. https://doi.org/10.1371/journal.pgen.1005939

Waites, C. L., Craig, A. M., & Garner, C. C. (2005). Mechanisms of vertebrate synaptogenesis. *Annual Review of Neuroscience*, *28*(1), 251-274. https://doi.org/10.1146/annurev.neuro.27.070203.144336

Wallace, D. C. (1994). Mitochondrial DNA sequence variation in human evolution and disease. *Proceedings of the National Academy of Sciences*, *91*(19), 8739-8746. https://doi.org/10.1073/pnas.91.19.8739

Walt., S. v. d., Schonberger, J. L., Nunez-Iglesias, J., Boulogne, F., Warner, J. D., Yager, N., Gouillart, E., Yu, T., & scikit-image, c. (2014). scikit-image: image processing in Python. *PeerJ*, *2*, e453. https://doi.org/10.7717/peerj.453

Wang, L., Tran, M., D'Este, E., Roberti, J., Koch, B., Xue, L., & Johnsson, K. (2020). A general strategy to develop cell permeable and fluorogenic probes for multicolour nanoscopy. *Nature Chemistry*, *12*(2), 165-172. https://doi.org/10.1038/s41557-019-0371-1

Waskom, M. (2021). seaborn: statistical data visualization. *Journal of Open Source Software*, *6*(60). https://doi.org/10.21105/joss.03021

Weber, M., Leutenegger, M., Stoldt, S., Jakobs, S., Mihaila, T. S., Butkevich, A. N., & Hell, S. W. (2021). MINSTED fluorescence localization and nanoscopy. *Nature Photonics*, *15*(5), 361-366. https://doi.org/10.1038/s41566-021-00774-2

Weissman, T. A., Sanes, J. R., Lichtman, J. W., & Livet, J. (2011). Generating and imaging multicolor Brainbow mice. *Cold Spring Harbor Protocols*, *2011*(7), 763-769. https://doi.org/10.1101/pdb.top114

Wolf, S., Sohmen, B., Hellenkamp, B., Thurn, J., Stock, G., & Hugel, T. (2021). Hierarchical dynamics in allostery following ATP hydrolysis monitored by single molecule FRET measurements and MD simulations. *Chemical Science*, *12*(9), 3350-3359. https://doi.org/10.1039/D0SC06134D

References

Wollman, A. J. M., Nudd, R., Hedlund, E. G., & Leake, M. C. (2015). From Animaculum to single molecules: 300 years of the light microscope. *Open Biology.* , *5*(4), 150019. https://doi.org/https://doi.org/10.1098/rsob.150019

Wurm, C. A., Neumann, D., Schmidt, R., Egner, A., & Jakobs, S. (2010). Sample preparation for STED microscopy. *Methods in Molecular Biology*, *591*, 185-199. https://doi.org/10.1007/978-1-60761-404-3_11

Xiang, W., Roberti, M. J., Heriche, J. K., Huet, S., Alexander, S., & Ellenberg, J. (2018). Correlative live and super-resolution imaging reveals the dynamic structure of replication domains. *Journal of Cell Biology*, *217*(6), 1973-1984. https://doi.org/10.1083/jcb.201709074

Yoneda, M., ANNE CHOMYN, ANDREA MARTINUZZI, HuRKot, O., & ATTARDI, G. (1992). Marked replicative advantage of human mtDNA carrying a point mutation that causes the MELAS encephalomyopathy. *Proceedings of the National Academy of Sciences*, *89(23), 11164-8*. https://doi.org/10.1073/pnas.89.23.11164

Zhou, L., Cai, M., Tong, T., & Wang, H. (2017). Progress in the Correlative Atomic Force Microscopy and Optical Microscopy. *Sensors*, *17*(4), 938. https://doi.org/10.3390/s17040938

Zhou, Y., & Danbolt, N. C. (2014). Glutamate as a neurotransmitter in the healthy brain. *Journal of Neural Transmission*, *121*(8), 799-817. https://doi.org/10.1007/s00702-014-1180-8

Zimmermann, T., Rietdorf, J., & Pepperkok, R. (2003). Spectral imaging and its applications in live cell microscopy. *Federation of the European Biochemical Societies Letters*, *546*(1), 87-92. https://doi.org/10.1016/S0014-5793(03)00521-0
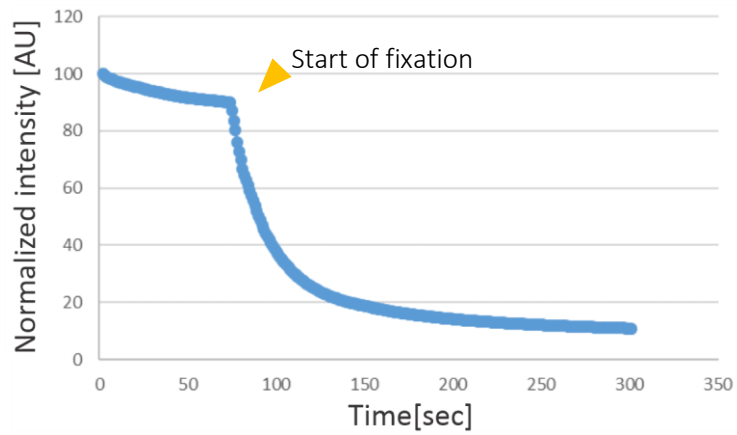
8 Supplements

8.1 Figures

8.1.1 DNA staining in primary neurons
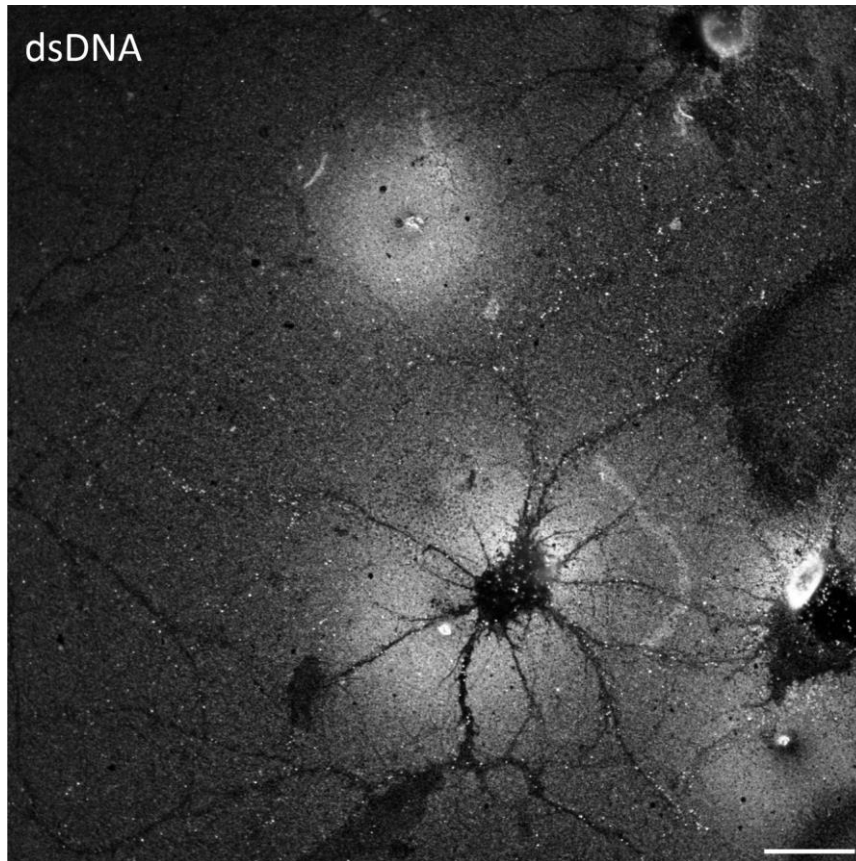
***Supplementary Figure 1: DIV14 neurons seeded on a poly-L-Lysine coated coverslip and stained with antibodies against double stranded DNA**. The staining shows cross-reaction to **poly-L-Lysine** resulting in bright background with dark spots on areas were cells grow. Scale bar 20 μm*

## 8.1.2 SiR bleaching due to fixation

Supplementary Figure 2: bleaching curve upon chemical fixation. *Cox8a-Snap HeLa cells were stained with Snap-SiR and imaged live at 3-second intervals. Fixation was initiated after 80 seconds. The graph shows fluorescence intensity over time. After fixation by adding 4% PFA to the medium, the intensity decreases to less than 20% of the initial fluorescence.*

8.1.3 Permeabilization using Saponin
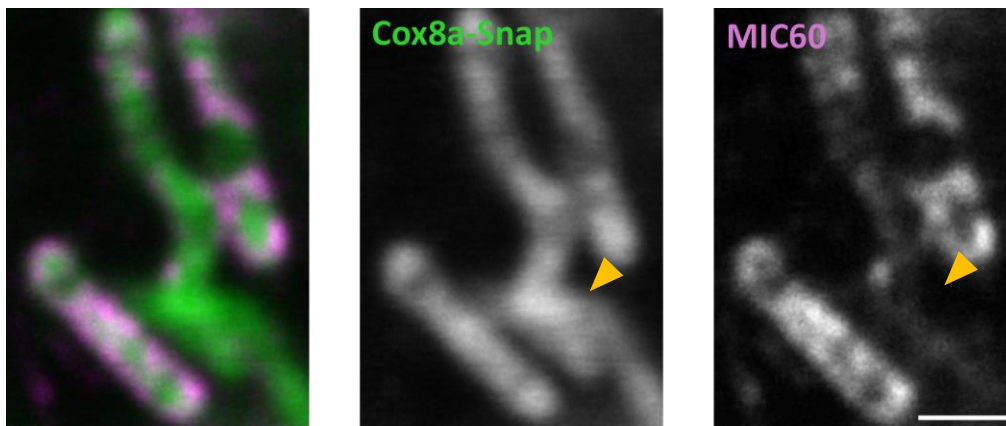
Supplementary Figure 3: Permeabilization with saponin is dependent on the lipid composition.*Confocal images of Hela cells stably expressing Cox8a-Snap. Live cells were stained with Snap-SiR, fixed as previously described, permeabilized with saponin, and stained against MIC60. The yellow arrow indicates an area showing Cox8a-Snap fluorescence but no MIC60 signal presumably due to insufficient permeabilization of all mitochondrial membranes. Scale bar: 1 µm.*

8.1.4 Nucleoid in growth cone
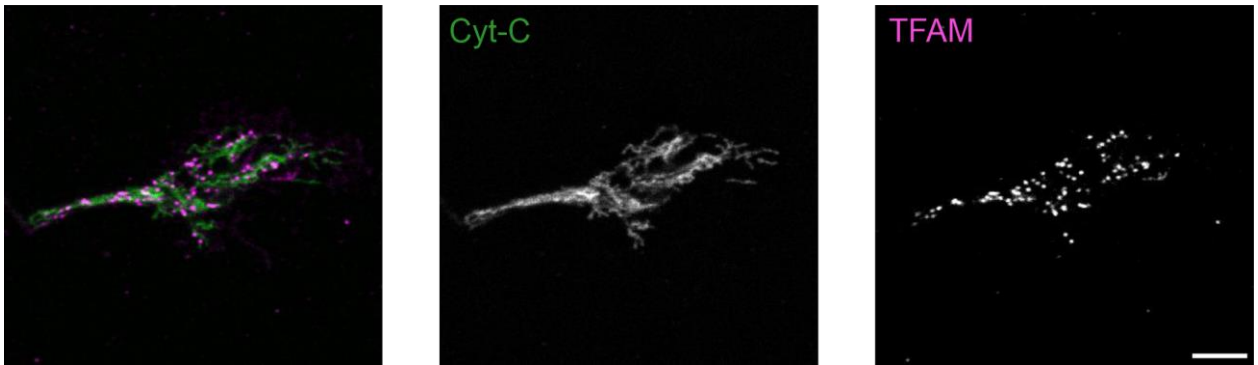
Supplementary Figure 4: TFAM distribution in growth cone. *Mitochondria are labeled with an anti Cyt-C antibody (green) and nucleoids with an antibody against TFAM (magenta). Scale bar: 5 µm.*

8.1.5   Field stimulation
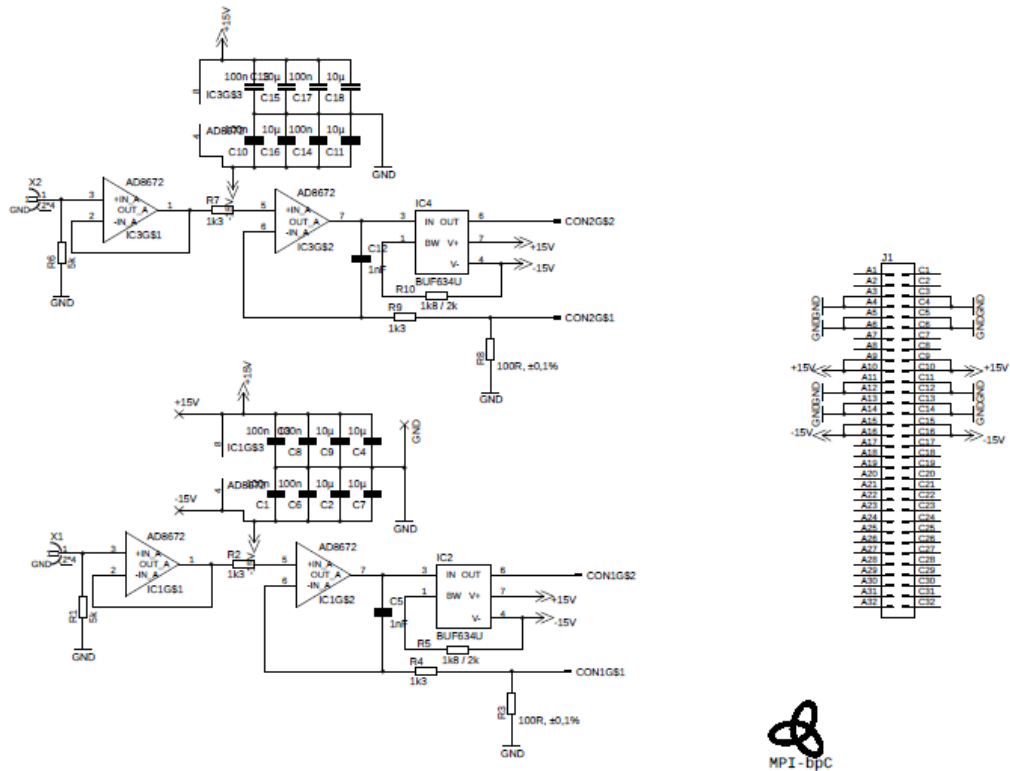
Supplementary Figure 5: Circuit diagram of a custom build device for electrical field stimulation of neuronal cell culture. *Current can be applied to the device and pulses are triggered by an external trigger source. Output is biphasic to avoid corrosion on the electrodes.*

8.2 Python code

8.2.1 Retrieval of the ROI

```python
################################################################
##################image registration###########################
################################################################
import numpy as np

import matplotlib.pyplot as plt

import tkinter as tk

from tkinter import filedialog

import scipy.ndimage as ndi

import cv2

from math import sqrt, atan2, cos, sin ,asin

from ipyfilechooser import FileChooser


###########################read ref image#######################


# Create and display a FileChooser widget

fc1 = FileChooser('/home/jovyan/Mirror Correlation')

display(fc1)

###########################read mov image#######################


# Create and display a FileChooser widget

fc2 = FileChooser('/home/jovyan/Mirror Correlation')

display(fc2)


######################### get file path#########################
# Print the selected path, filename, or both

print(fc1.selected_path)

print(fc1.selected_filename)

print(fc1.selected)
```

```
file_path1=fc1.selected

ref_im = (cv2.imread((file_path1),0))

folder_path=(fc1.selected_path)

########################## get file path############################
# Print the selected path, filename, or both
print(fc2.selected_path)
print(fc2.selected_filename)
print(fc2.selected)

file_path2 =fc2.selected

mov_im = np.flipud((cv2.imread(file_path2,0)))
mov_im = np.rot90(mov_im,1,(0,1))

############################center moving image###########################

A_center=np.float32([[0.940306, 0, -510],
          [0, 0.940306, -344]])

mov_im_center=cv2.warpAffine(mov_im, A_center, ref_im.shape, flags=cv2.WARP_INVERSE_MAP)

###############################cv2 SIFT#####################################

# Initiate SIFT detector
sift = cv2.SIFT_create()

# find the keypoints and descriptors with SIFT
kpS1, desS1 = sift.detectAndCompute(ref_im,None)
```

```
kpS2, desS2 = sift.detectAndCompute(mov_im_center,None)


# draw only keypoints location,not size and orientation

img3 = cv2.drawKeypoints(ref_im,kpS1,outImage = None, color=(255,0,0))

img4 = cv2.drawKeypoints(mov_im_center,kpS2,outImage = None, color=(255,0,0))


####################Matching FLANN#########################################

MIN_MATCH_COUNT = 10

FLANN_INDEX_KDTREE = 0


index_params = dict(algorithm = FLANN_INDEX_KDTREE, trees = 5)

search_params = dict(checks = 50)


flann = cv2.FlannBasedMatcher(index_params, search_params)


matchesF = flann.knnMatch(desS1,desS2,k=2)


#-- Filter matches using the Lowe's ratio test

ratio_thresh = 0.75

good_matches = []

for m,n in matchesF:

    if m.distance < ratio_thresh * n.distance:

        good_matches.append(m)



# Draw first 10 matches.

img6 = cv2.drawMatches(ref_im,kpS1,mov_im_center,kpS2,good_matches,None)


cv2.imwrite(folder_path+'/draw matches.png',img6)

plt.imshow(img6),plt.show()
```

```python
#-- Localize the object

obj = np.empty((len(good_matches),2), dtype=np.float32)

scene = np.empty((len(good_matches),2), dtype=np.float32)

for i in range(len(good_matches)):

    #-- Get the keypoints from the good matches

    obj[i,0] = kpS1[good_matches[i].queryIdx].pt[0]

    obj[i,1] = kpS1[good_matches[i].queryIdx].pt[1]

    scene[i,0] = kpS2[good_matches[i].trainIdx].pt[0]

    scene[i,1] = kpS2[good_matches[i].trainIdx].pt[1]


A_T_S, inliers= cv2.estimateAffinePartial2D(obj,scene)


###################decompose Matrix#####################################


theta0=np.degrees(np.arctan(-A_T_S[0,1]/A_T_S[0,0]))

theta1=np.degrees(np.arctan(A_T_S[1,0]/A_T_S[1,1]))

print(np.degrees(asin(-A_T_S[1,0])))

tx=(A_T_S[0,2])

ty=(A_T_S[1,2])


Sx = np.sqrt(np.power(A_T_S[0, 0], 2)+np.power(A_T_S[0,1], 2))

Sy = np.sqrt(np.power(A_T_S[1, 0], 2)+np.power(A_T_S[1,1], 2))

print('\n' ,'Winkel Theta0:',theta0,'\n' ,'Winkel Theta1:',theta1, '\n' ,

    'Scaling X:',Sx,'%','\n' ,'Scaling Y:',Sy,'%','\n','Translation X:',tx,

    'px','\n','Translation Y:',ty,'px')


im7=cv2.warpAffine(mov_im_center, A_T_S, ref_im.shape, flags=cv2.WARP_INVERSE_MAP)


################################################################################

##############################find position#####################################

################################################################################
```

Supplements

```
##############################WF Positions##############################
'''[X , Y] of the reference image and of the fluorescent image'''
ref_pos=np.array([ 3006.10009765625,197.39999389648438])


im_1_pos=np.array([2030.300048828125,1560.0999755859375])



##############################STED Positions##############################
'''[X , Y] of the moving image'''
mov_pos=np.array([-2390.6,-2324.9])


im_1_pos_Sted=np.array([2017.1,-5833.6])
##############################Distance##############################


disX=((ref_pos[0])-(im_1_pos[0]))
disY=((ref_pos[1])-(im_1_pos[1]))


dis= sqrt((disX**2)+(disY**2))
alpha=atan2(disY,disX)




print('Diastance Ref Im1',dis,'\n','angle between Ref Im1',np.degrees(alpha),'\n','\n')
cor_factor= np.radians(theta0+5+180)
FindX=mov_pos[0] +(dis*-cos((alpha+cor_factor)*-1))
FindY=mov_pos[1] +(dis*-sin((alpha+cor_factor)*-1))
```

9 Acknowledgements

I would like to dedicate the last chapter to all those who have supported me on my way.

First, I would like to thank Prof. Dr. Stefan Jakobs, who guided me and gave me the opportunity to work in such a unique environment. Not only in terms of science, but also in terms of the many nice people he has gathered around him. At this point, I would also like to thank Prof. Dr. Stefan Hell for his hospitality in the Department of Nanobiophotonics.

Furthermore, I would like to thank my TAC members Prof. Dr. Michael Müller and Prof. Dr. Michael Meinecke. For time, help and guidance during this work.

I would also like to thank the animal station, especially Sascha Kraus and Ulrike Teichmann for their help in setting up the neuronal cell culture. As well as the mechanical and electrical workshops of the MPI NAT for help in building the many prototypes.

For proofreading and helpful comments on this work I would like to thank Dr. Peter Ilgen, Dr. Nickels Jensen, Dr. Felix Lange, Dr. Christian Brüser and Christiaan Stuut. I would also like to thank the entire NanoBiophotonics department for a wonderful 4 years.

Last but not least, I would like to thank my family and friends for their support and the nice time outside the lab, which helped me to get a clear head.

10 Curriculum Vitae

Axel Rösch

Bürgerstraße 23
37073 Göttingen, Germany
axel.roesch@mpibpc.mpg.de

WORK EXPERIENCE

04.2018 - 09.2022:　**PhD Candidate**

Clinic for Neurology, University Medical Center Göttingen, & Max Planck Institute for Multidisciplinary Sciences Göttingen, Prof. Stefan Jakobs

- Developing a correlative fluorescent microscopy cross-platform workflow. Applied on correlation of live cell and different super resolution microscopes.
- Exploring mitochondrial DNA distribution and its implication on mitochondrial function in neurons.

04.2017 - 12.2018:　**Master Thesis**

Center for Biological Signalling Studies (BIOSS), Römer Lab, University of Freiburg

- Investigation of protein trafficking to the primary cilium using quantitative microscopy and fluorescence correlation spectroscopy.

10.2016 - 04.2017:　**Internship**

Molecular Imaging Center University of Bergen, Norway, Prof. Jaakko Saraste

- Investigation microtubule nucleation on the ER-Golgi intermediate compartment using live and super-resolution microscopy.

2015 - 2018:　**Research Assistant**

Institute of Physical Chemistry, University of Freiburg, Prof. Thorsten Hugel

- Designing hardware controls for custom made TIRF-FRET and magnetic tweezer setups using LabVIEW.

EDUCATION

04.2018 - 09.2022:   **PhD candidate in graduate school Molecular Medicine**

Clinic for Neurology, University Medical Center Göttingen, & Max Planck Institute for Multidisciplinary Sciences Göttingen, Prof. Stefan Jakobs

10.2015 - 04.2018:   **Master of Biochemistry and Biophysics**

University of Freiburg, Germany

SCIENTIFIC MEETINGS

11.2021:   **SFB 1286 Symposium**

Göttingen, Germany

09.2019:   **Symposium: Quantitative Synaptology SFB 1286,**

Göttingen, Germany

11.2018:   **Labeling and Nanoscopy 2018,**

Heidelberg, Germany

PUBLICATIONS

Stephan, T., Roesch, A., Riedel, D., & Jakobs, S. (2019). Live-cell STED nanoscopy of mitochondrial cristae. *Scientific reports*, *9*(1), 1-6.

Stroukov, W.*, Rösch, A.*, Schwan, C., Jeney, A., Römer, W., & Thuenauer, R. (2019). Synchronizing protein traffic to the primary cilium. *Frontiers in genetics*, *10*, 163. (*shared first)